Czech Technical University in Prague
Faculty of Nuclear Sciences and Physical Engineering
Department of Physical Electronics

&

Université Bordeaux 1
École Doctorale des Sciences Physiques et de l'Ingénieur
Centre Lasers Intenses et Applications

Ion Acceleration in Small-size Targets by Ultra-intense Short Laser Pulses (Simulation and Theory)

A dissertation thesis submitted to the CTU in Prague and Université Bordeaux 1 in partial fulfillment of the requirements for the degree of Doctor of Philosophy (PhD)

Author: **Jan Pšikal**
Supervisors: **Jiří Limpouch, Vladimir Tikhonchuk**
Date of submission: **16.10.2009**

Declaration

This dissertation is the result of my own work, except where explicit reference is made to the work of others, and has not been submitted for another qualification to this or any other university.

Prague, 16th October 2009 Jan Pšikal

Acknowledgements

Due to the fact that my doctoral studies were spent between the Department of Physical Electronics at the Faculty of Nuclear Sciences and Physical Engineering of the Czech Technical University in Prague and Centre Lasers Intenses et Applications in the campus of University of Bordeaux 1, many people deserve my thanks.

First and foremost, I must thank my two excellent supervisors - Prof. Jiri Limpouch from Prague and Prof. Vladimir Tikhonchuk from Bordeaux. I strongly appreciate their guidance, encouragement, patience with me, and their humanity. They have given me enough freedom to make my own mistakes and learn from them but at the same place they have gently pushed me forward in the right direction.

Among first people, I also have to express my profound gratitude to my family - my beloved parents and my brother. During the course of my PhD study, we lived in a very difficult time for us. My father became seriously ill and he left us after 16 months of our fight against his disease. I am grateful to Vladimir who kindly tolerate my frequent holidays in the Czech Republic with my family at this difficult time and to many others for their help. I have written this thesis mainly to my beloved dad who strongly supported my study and education. Unfortunately, he cannot be present at the end of my study which have taken really enough time (in fact, I started at school 21 years ago), but he is still with me in my heart.

During my PhD study, I have met many excellent physicists and kind people. I would like to thank Dr. Sargis Ter-Avetisyan from the Queen's University of Belfast, Prof. Alexander Andreev from Research Institute for Laser Physics in St. Petersburg, Prof. Shigeo Kawata from Utsunomiya University in Japan, and Dr. Julien Fuchs from Laboratoire pour l'Utilisation des Lasers Intenses (LULI) in Palaiseau close to Paris for interesting and fruitful cooperation.

I appreciate my young colleagues from Prague and Bordeaux, who have given me important advice and who have kindly helped me. I express my thanks to Ondřej Klimo, Martin Mašek, Daniel Klír, Arnaud Debayle, Afeintou Sangam, Roland Duclous, Cyril Regan, Candice Mezel, Marion Lafon, and others.

Finally, support by the following projects is also gratefully acknowledged:

- Ministry of Education, Youth and Sports of the Czech Republic, projects No. LC528 and No. MSM6840770022
- Czech Science Foundation, projects No. 202/08/H057 and No. 202/06/0801
- Czech Technical University in Prague, projects No. CTU0708014, No. CTU0813214, and No. CTU0916514
- Grant of french government - "Bourse de Doctorat en co-tutelle"

I forgot to name plenty of kind people, but I must cut the list somewhere. Excuse me and thank you all.

Contents

Chapter 1

Introduction

1.1 Motivation

Advent of chirped-pulse amplification (CPA) enabled generation of very short laser pulses (10's - 100's fs) of a high intensity ($I\lambda^2 > 10^{18}\ \mathrm{W cm^{-2} \mu m^2}$) [1]. Beyond intensities of a few times $10^{18}\mathrm{W/cm^2}$, the motion of electrons in the electromagnetic field of the laser becomes relativistic, as the electron velocity approaches the speed of light within only one oscillation period, and a large variety of new phenomena opens up [2] - wakefield generation, relativistic focusing, relativistic transparency, nonlinear modulation, multiple harmonic generation, etc.

When these laser pulses interact with any kind of target material, the rising edge of the pulse is already sufficiently intense to transform matter into the plasma state. The main part of the pulse then interacts with a highly ionized and heated plasma. Due to collective effects of the freed electrons, such a plasma can support electric fields in excess of $10^{12}\ \mathrm{V/m}$. These fields are higher by several orders of magnitude compared to conventional particle accelerators that usually operate at $10^8\ \mathrm{V/m}$. Due to the higher field strengths, the acceleration length for ions in the energy range of several hundreds of MeV is of the order of $1\ \mathrm{mm}$ at most. Therefore, femtosecond table-top lasers are a promising alternative to conventional radiofrequency accelerators.

There are two main acceleration scenarios able to explain the observation of fast ions in a typical experiment on femtosecond laser pulse interaction with solid foil targets. In the first scenario, the electrons are pushed into the target by the radiation pressure of the incident laser beam (i.e., by the ponderomotive force) and the ions are accelerated by generated electrostatic field at the target front side [3]. This mechanism is called radiation pressure acceleration (RPA) and could be more efficiently realized with circularly polarized laser pulses [4]-[6]. In the second scenario, a population of hot electrons, generated by a laser pulse on the front side of the target, crosses the target and propagates beyond its rear side, where a sheath layer is formed, and, again, a strong electrostatic field accelerates ions [7], [8]. This is the so-called target normal sheath acceleration (TNSA) and is commonly used and cited in numerous experiments.

Most of experimental groups are using thin metal or insulator foil targets as they can be easily characterized and positioned. Ions accelerated in such targets are mainly protons originated from low-Z hydrocarbon or water deposits. The deposits can be removed by

heating the target to a high temperature before laser-target interaction [9]. Experiments have demonstrated acceleration of protons to almost 60 MeV [10], fluorine ions to above 100 MeV [11] and high-Z palladium ions up to 225 MeV [12].

It was demonstrated [13] that the acceleration based on high intensity lasers produces high quality particle beams that compare favourably with conventional acceleration techniques in terms of emittance, brightness and pulse duration. One of the drawbacks is a very broad, exponential energy spectrum of the emitted particles, although quasimonoenergetic proton [14] and carbon ion spectra [15] were also demonstrated by using of microstructured or advanced targets. Scaling laws of maximum proton energy and laser-to-proton conversion efficiency [16] - [18] are still under debate as they depend on many laser and target parameters - laser pulse energy, intensity, duration, contrast, target composition, thickness, etc. However, it is obvious that the maximum energy, conversion efficiency, or the location of ion emission zone depend on hot electrons characteristics and dynamics in the target.

The interaction of femtosecond pulses with massive targets is not too efficient because the energy delivered to charged particles spreads out quickly over distances much larger than the laser focal spot size and it is redistributed between many secondary particles. One possibility to limit this undesirable energy spread and to achieve a high energy density deposition is to use small-size targets, such as microdroplets, big clusters, and small foil sections. For example, a deposition of 100 mJ in a water droplet of a diameter of $5\ \mu\mathrm{m}$ would correspond to the mean kinetic energy of about $5\ \mathrm{keV}$ for each particle. Since the expansion time of such a droplet is greater than $1\ \mathrm{ps}$, during this time period one can study a matter in quite unusual state of a very high density and temperature in same time.

Experiments with ordinary or heavy water microdroplets of diameter about $10 - 20\ \mu\mathrm{m}$, which is comparable to the laser spot size, have been reported in the last decade [19]-[24]. The main interest has been concentrated on proton or deuteron acceleration up to several MeVs and on monoenergetic feature in deuteron spectra [21], [22] explained by a spatial separation of two ion species, deuterons and oxygen, in the acceleration domain of a finite-volume target [25].

Recently published experiments in Ref. [26] with a cloud of water droplets of a diameter $150\ \mathrm{nm}$, the so-called waterspray target, have shown a surprisingly high fast proton emission efficiency, only two times lower than for a single $20\ \mu\mathrm{m}$ droplet, even if the total mass in the spray is three orders of magnitude smaller than that of a single droplet. Due to a larger ratio of the surface to volume for the cloud of droplets of sub-wavelegth diameter than for a single droplet of the same mass and a large number of droplets in a focal volume, efficient laser pulse absorption is enabled, which provides high electron temperatures and ion acceleration to high energies.

The main disadvantage of the using of spherical targets is almost an isotropic distribution of generated hot electrons and resulting angular divergence of accelerated ions. To limit the divergence of accelerated particles, flat foil or curved foil sections seem to be a promising alternative [27] as will be presented in one of the following chapters.

Other possibility to limit the undesirable energy spread is hot electron guiding in the case of large incidence angle of the laser pulse on a foil [28]-[33]. Hot electrons can be confined in a potential well formed by strong quasi-static magnetic and electric fields along the target surface. Moreover, the electrons can be resonantly accelerated by laser field inside the

potential well [34]. This could result in hot electron temperatures exceeding ponderomotive potential and transport of those electrons along the foil front surface far beyond interaction region. Small-size targets have advantages in the case of large incidence angles also, they prevent undesired spread of electrons outside the interaction zone.

1.2 Aims and new contributions of the work

The major direction for this work is to investigate the parameters that provide the most efficient utilization of laser energy and the control of ion parameters with presently available intensities for table-top laser systems (that means usually femtosecond Ti:Sapphire lasers able to produce moderate relativistic intensities from 10^{18} up to 10^{21} Wcm^{-2}) and comprehension of recent experimental data on ion acceleration in water spray target [26] and in thin foils of reduced surface [35]. Unlike numerous theoretical groups, we are not interested in novel acceleration schemes for rather ultrarelativistic regimes which have been recently theoretically described, such as laser piston acceleration [36], laser break-out afterburner [37], or stable radiation pressure acceleration by circularly polarized laser pulses [38]. These novel schemes could lead to even GeV ion energies as has been demonstrated by numerical PIC simulations.

In our case of moderate relativistic intensities, the improvements in terms of increased maximum ion energy and laser-to-ion conversion efficiency, could be achieved by enhanced density or energy of hot electrons mediating the ion acceleration. One possibility to achieve a higher ion acceleration efficiency is to reduce the target thickness, which has been described theoretically and demonstrated experimentally in the last decade [17], [39]-[41]. Here, we propose to increase further the efficiency by reducing transverse target sizes. Moreover, if the transverse target sizes are comparable or less than the laser beam width, multispecies ion composition can lead to quasimonoenergetic feature in ion energy spectra as the accelerating electric field is nearly uniform [42]-[44]. We have shown that this feature can be more pronounced in medium clusters near the maximum ion energy, where ions are accelerated by thermal expansion together with Coulomb-like explosion.

Therefore, this thesis is dedicated to numerical and theoretical study of femtosecond laser pulses interaction with small-size targets. Such targets are attractive for their capacity to limit the energy spread of absorbed laser pulse energy (by electrons). We consider fully ionized targets of given shapes, sizes, composition and plasma density profiles (usually steep or step-like) interacting with a short intense laser pulse of certain duration, intensity, temporal and spatial pulse profile. The interaction is modeled by two-dimensional particle-in-cell (PIC) code, obtained numerical results are analyzed, discussed and compared with published theory and experiments.

During the course of this thesis, the following goals have been achieved and the following new and important aspects have been discovered and described:

- **Simulations and theory of laser pulse interaction with mass-limited targets.** Mass-limited targets (MLTs) are solid targets of sizes comparable to the laser spot size. We demonstrated that they can enhance the efficiency of laser energy transformation into fast ions by reducing the spread of hot electrons in the transverse plane

and have contributed to the comprehension of recent experiment [35]. MLTs present a specific intermediate interaction regime between the targets much larger than the laser focal spot (bulk solids and foils) and interactions with sub-wavelength nanometer-size atomic clusters. We performed several studies on MLTs dealing with ion acceleration and we discuss the physical processes that are responsible for an enhancement of maximum ion energy and improved laser-to-proton conversion efficiency. The effects of multispecies target composition and the resulting modulations in light ion (usually proton or deuteron) energy spectra, various target shapes are also studied.

- **Laser proton acceleration in a water spray target.**
  We contributed to theoretical explanation of experimental results on laser proton acceleration in a water spray target [26] mainly by numerical simulation of the laser pulse interaction with a water droplet of a sub-wavelength diameter. The interaction of this type of target (cloud of big clusters) with femtosecond laser pulses substantially differs from the interaction with MLT, but also from the interaction with nanometer-size atomic clusters. Big clusters with diameters in the 100 nm range (which is the case) are expanding under the pressure of hot electrons, which cannot leave the target because of its very high electric charge. The hot electron pressure dominate in clusters in contrast to the MLT, where the hot electrons are in minority compared with the background cold electrons.

- **Lateral hot electron transport and ion acceleration in femtosecond laser pulse interaction with thin foils.**
  We investigated hot electron transport in small foil sections and the resulting ion acceleration from different foil faces when the laser pulse is obliquely incident on the foil front. In the case of large incidence angle, a part of hot electrons can be confined on the foil front by generated quasi-static electric and magnetic fields, accelerated to very high energies and transported towards an edge (lateral side) of the foil in the direction of laser wave vector projection onto the foil front surface. There, ions can be accelerated to higher maximum energy than beyond interaction region. However, their total number is rather low. It was also shown that hot electron recirculation forth and back still plays an important role which is useful to know for the cone target design in fast ignition concept.

- **Development of 2D3V PIC code and its broad applicability.**
  Recently developed particle-in-cell code with two spatial and three velocity components during author's Master thesis [47], [48] has been further improved and its parallel version was newly developed (for shared memory systems). The code have shown quite broad range of its applicability in various laser-plasma interaction studies and is presently employed by other users from Czech Technical University in Prague. A knowledge of all parts of the PIC code is a great advantage that enables modification of its content relatively easily according to various requirements related to a given problem in laser plasma physics.

1.3 Thesis Structure

This thesis is structured in the following manner:

- Chapter 2 covers basic theory of laser-plasma interaction mainly related to the acceleration of particles (electrons, ions) and to the following presented results. The theory of interaction of ultrashort and intense laser pulses with overdense plasma is reviewed in the point of view of the author. After necessary basic theoretical background including a brief review of basic plasma parameters and the models of plasma description, this chapter is devoted to the explanation of laser-plasma interaction conditions, propagation of intense laser beam in plasma, electron acceleration mechanisms at the critical surface of overdense plasma with step-like or very steep density gradient and related issues (angular distribution and propagation of accelerated electrons), and ion acceleration mechanisms in solid targets and clusters.

- Chapter 3 describes numerical methods used for our theoretical studies - a relativistic collisionless 2D3V (with two spatial and three velocity components) particle-in-cell code that author developed during the end of his Master and at the beginning of his PhD study at the Czech Technical University. After more detailed discussion about the difference of direct numerical solution of kinetic Vlasov equation and particle-in-cell method, numerical algorithms employed in the code are described. Some novel efficient algorithms have been implemented here - zigzag scheme for the computation of current densities in order to guarantee automatic compliance with the continuity equation and damping regions for the absorption of outgoing electromagnetic waves.

- Chapter 4 contains our theoretical and numerical results obtained during the course of this thesis on mass-limited targets. This chapter starts with our preliminary results that documented more efficient ion acceleration in the case of mass-limited targets compared to the usual foil target. Then, we consider various shapes and density profiles of targets of uniform chemical composition of two ion species. Finally, we present recent experimental results from LULI laser facility in Palaiseau (France) on enhanced proton acceleration in foils of reduced surface and our explanation of the enhanced acceleration based on the transverse refluxing of hot electrons in such small foil sections.

- Chapter 5 includes experimental results obtained at Max Born Institute in Berlin (Germany) on laser proton acceleration in water spray targets and the corresponding theoretical findings. We contributed to the theoretical interpretation of these results by the simulations of laser interaction with a sub-wavelength water droplet. The latter gives the basic idea of the physics of laser interaction with the cloud of such droplets.

- Chapter 6 is devoted to our theoretical study of lateral hot electrons transport and ion acceleration in femtosecond laser pulse interaction with thin foils. We discuss two mechanisms of the transport: the first one is due to hot electron recirculation across the foil and the second is electron guiding along the foil surface by quasi-static magnetic and electric fields. Then, the efficiency of ion acceleration (proton maximum energy and energy fluence) is compared from different target regions.

Chapter 2

Laser-plasma Acceleration

2.1 Basic theoretical background

Plasma is basically a many-body system composed of electrons and ions that are coupled to one another by their electric and magnetic fields. Because of the vast number of electrons and ions taking part in the interaction, an adequate theoretical description has to consider an average over all particles. Macroscopic parameters (T_e, T_i, n_e, n_i, and $\bar{Z}$) are introduced describing most phenomena quite well in plasmas close to thermodynamic equilibrium. The parameters n_e and n_i denote the electron and ion density in units of number of particles per cm^3. Created out of neutral matter, plasmas are generally quasi-neutral. In other words, the product of the number of ions and the average charge state (mean ion charge) $\bar{Z}$ of the ions equals the number of free electrons.

$$n_e = \bar{Z} n_i \tag{2.1}$$

T_e and T_i denote the electron and the ion temperature, respectively. The temperature can be defined for a thermodynamic equilibrium via the Maxwellian distribution function $f(\varepsilon_{kin})$ in kinetic energy

$$f(\varepsilon_{kin}) = \frac{2}{\sqrt{\pi}(k_B T)^{3/2}} \sqrt{\varepsilon_{kin}} \exp\left(-\frac{\varepsilon_{kin}}{k_B T}\right) \tag{2.2}$$

Concentrating on the electrons, the mean thermal velocity v_{te} for electrons moving in one direction is linked to the electron temperature by

$$\varepsilon_{kin} = \frac{1}{2} m_e v_{te}^2 = \frac{1}{2} k_B T_e \quad \text{thus} \quad v_{te} = \sqrt{\frac{k_B T_e}{m_e}}, \tag{2.3}$$

where m_e is the electron mass and k_B is the Boltzmann constant. For practical reasons, the temperature is given in energy units of eV, according to the relation $1\ eV \approx 1.2 \times 10^4$ K. Since $\sqrt{m_i/m_e} << 1$, the thermal velocity of ions v_{ti} is much smaller for $T \approx T_e \approx T_i$.

The thermal equilibrium is ensured by collisions. The rate of the momentum transfer between particles is expressed by collision frequencies. Electrons in the intense laser field are accelerated to very high velocities, whereas the ions stay almost at rest and do not respond onto a high frequency laser field due to their much higher inertia. The electron-ion collision frequency for an electron with velocity $v_e >> v_{te}$ is given by [45]

$$\nu_{ei} = \frac{3 Z^2 e^4 n_i \ln \Lambda}{8\pi \epsilon_0^2 m_e^2 v_e^3}. \tag{2.4}$$

where $\ln \Lambda$ is the Coulomb logarithm which can be usually regarded as constant with the value of order of unity. Nevertheless, these collisions do not mediate considerable energy transfer, since the mass of an ion is much larger than the mass of electron and only the part of $2m_e/m_i$ of electron energy can be transferred between the particles in each collision. The energy is transferred mainly due to the collisions of the same particle species, where the corresponding electron-electron collisional frequency is $\nu_{ee} = \nu_{ei}/Z$ and the relaxation time of electron energy distribution function is $\tau_e \approx Z\nu_{ei}^{-1}$. The characteristic time of energy transfer from electrons to ions is $\tau_T = m_i/(2m_e)\nu_{ei}^{-1}$, which is about 10^4 times higher than the relaxation time of electrons. Thus, in some cases, such as for the plasma interaction with less intense ($\approx 10^{15}\, Wcm^{-2}$) ns laser pulses, one can consider plasma composed of electrons and ions with a Maxwellian distribution, but different temperatures $T_e >> T_i$. However, in the case of femtosecond laser pulses, since the electrons in the relativistic laser field are accelerated to very high velocities close to c and $\nu_{ee} \sim v_e^{-3}$, the plasma irradiated by femtosecond laser pulses is certainly out of the thermal equilibrium with a single electron temperature as the electrons with high relativistic velocity do not heat the plasma by collisional effects. There, one can usually consider background plasma with the cold electron temperature and the population of hot electrons accelerated by the laser field. As the time scale of phenomena studied in this thesis (related to hot electrons) is less than τ_e the collisions are omitted here.

Electrons and ions in plasma are influenced by the electric field $\vec{E}$ produced by the nearby charges. The electric field can be decomposed into two separate fields $\vec{E}_{micro} =< \vec{E} > +\delta\vec{E}$ with different spatial scales [49]. $\delta\vec{E}$ has fluctuations on a scale below the so-called Debye length λ_D, which is the length over which the field contribution of a single charge is shielded by the surrounding electrons. This rapidly fluctuating microfield is due to random collisions between individual charged particles. Therefore, collisional processes are linked to $\delta\vec{E}$. On the other hand, $< \vec{E} >$ is related to deviations from charge neutrality on a scale that is large compared to λ_D, averaging out small scale fluctuations. Thus, $< \vec{E} >$ gives rise to collective or collisionless electron motion, like plasma waves. This classification provides a natural separation into collisional an collective behavior.

The Debye length can be given in terms of n_e and T_e as

$$\lambda_D = \sqrt{\frac{\epsilon_0 k_B T_e}{e^2 n_e}} \tag{2.5}$$

with the electron charge e and the permittivity of free space ϵ_0. A closely related parameter is N_D, the number of particles within the so-called Debye sphere that denotes a sphere with radius λ_D.

$$N_D = \frac{4\pi}{3}\lambda_D^3 n_e \tag{2.6}$$

If there are many particles in the Debye sphere, the microscopic fluctuations related to $\delta\vec{E}$ are effectively screened and the macroscopic description of the plasma is more appropriate. More particles in the Debye sphere means a smaller contribution of collisions and, thus, the collective behavior becomes dominant.

Another important parameter related to the electron density, is the electron plasma frequency ω_p. Subsequently to a distortion of the charge neutrality, the electrons within the

plasma tend to oscillate with the frequency

$$\omega_p = \sqrt{\frac{e^2 n_e}{\epsilon_0 m_e}} \tag{2.7}$$

Similarly, we can define ion plasma frequency

$$\omega_{pi} = \sqrt{\frac{n_i Z^2 e^2}{m_i \epsilon_0}} = \sqrt{\frac{Z m_e}{m_i}} \omega_p \tag{2.8}$$

The theory usually assumes two classes of electric fields [50]: high-frequency field and low-frequency (quasi-static one). The first one is of the order of $1/\omega_p \approx 10^{15} s$ for electron density $n_e \approx 10^{21}\ \mathrm{cm}^{-3}$ which is of the order of critical density n_{crit} for the wavelength $\lambda = 1\ \mu\mathrm{m}$, the second on the time scale of the order of $1/\omega_{pi}$. Due to much larger mass of ions, usually only the motion of electrons is considered in the high-frequency electric field. Thus, the electrons tend to be quickly in equilibrium with external electric potential φ. If we assume one-dimensional problem, the density of electrons $n_e(x)$ in equilibrium with quasi-static electric field is given by the Boltzmann law

$$n_e(x) = n_{e0} \exp\left(\frac{-e\varphi(x)}{k_B T_e}\right) \tag{2.9}$$

2.1.1 Three approaches to plasma physics

There are three basic approaches to plasma physics: the hydrodynamic theory, the kinetic theory, and the particle theory. Each approach has some advantages and limitations which stems from simplified assumptions appropriate only for certain phenomena and time scales.

- **Hydrodynamic description**
  In the hydrodynamic model, the conservation laws of mass, momentum and energy are coupled to Maxwell equations. In addition, for a fluid model, a local thermodynamic equilibrium is assumed and the knowledge of the equations of state (relations between pressure, temperature, energy, entropy, etc.) is mandatory for solving the problem. The fluid theory is a good approximation for many phenomena in the interaction of plasma with relatively low laser intensities ($\approx 10^{15}\ \mathrm{W/cm}^2$) and relatively long laser pulses (ns). However, the model is not always adequate, because there is an assumption of local thermodynamic equilibrium (LTE). All the variables in the fluid equations are functions of time and position, and each species in an LTE plasma has a Maxwellian distribution of the velocities everywhere. Physical quantities such as temperature and pressure can be defined only in LTE. Systems that are not in LTE (such as plasma interacting with relativistically intense femtosecond laser pulse) cannot be described by fluid equations. Hydrodynamic model can describe a target globally including nonionized solid part of the target.

- **Kinetic description**
  The kinetic theory is based on a set of equations for the distribution functions $f_s(\vec{q}, \vec{p})$

of each plasma particle species (where s is the index of particle species), together with Maxwell equations. The distribution function is a statistical description of a very large number of interacting particles. Each particle has its own position in the phase space $(\vec{q}, \vec{p})$, where $\vec{q}$ are the coordinates for all the degrees of freedom and $\vec{p}$ are the corresponding momentum. In this approach, $f_s(\vec{q}, \vec{p})\mathrm{d}^3\vec{q}\mathrm{d}^3\vec{p}$ is equal to the number of particles of species s (for example, electrons and protons) in the domain $[(\vec{q}, \vec{q} + \mathrm{d}\vec{q}), (\vec{p}, \vec{p} + \mathrm{d}\vec{p})]$.

Vlasov equation describing the evolution of single-particle distribution function $f_s(\vec{r}, t)$ for each species of particle is given as follows:

$$\frac{\partial f_s}{\partial t} + \frac{\vec{p}}{m_s\gamma}\frac{\partial f_s}{\partial \vec{r}} + q_s\left(\vec{E} + \left(\frac{\vec{p}}{m_s\gamma}\right) \times \vec{B}\right)\frac{\partial f_s}{\partial \vec{p}} = 0, \tag{2.10}$$

where m_s is the rest mass of particle species s, q_s its charge, $\vec{E}$ and $\vec{B}$ electric and magnetic fields in position $\vec{r}$ and time t. The statistical content of the Vlasov equation is expressed by assuming that f_s is a smooth function (i.e., differentiable) describing an average quantity over a phase space volume $\mathrm{d}^3\vec{q}\mathrm{d}^3\vec{p}$ containing a large number of particles. The electromagnetic fields, $\vec{E}$ and $\vec{B}$ are also smooth averaged quantities. The force acting on any plasma particle, describing the effect of all the other particles, is assumed to be a continuous and slowly varying function of space. This is a good approximation only if the collective effect is larger than direct collisions with nearby particles; therefore, the Vlasov equation is considered to be collisionless. If the short-range collisions are important, the collision term is added on the right hand side of Eq. (2.10) [51].

- **Particle description**
  The particle theory approach uses the equations of motion for the individual plasma particles. The plasma is described by electrons and ions moving under the influence of the electric and magnetic fields due to their own charge, and of the laser fields. For practical reasons, computer simulation of plasma using particle codes is limited to $N \approx 10^8$ particles, whereas one has $N \approx 10^{15}$ in typical laboratory laser-plasma systems [50]. Therefore, each simulation particle represents a large number of real electrons and ions. However, the decreasing number of particles means increasing noise, which indicates that this approach has limitations and some specific phenomena have to be studied by kinetic approach. Different aspects and similarities of kinetic (Vlasov code) and particle (PIC code) approach will be discussed in the next chapter.

2.2 Motion of a single particle in relativistic laser field

The motion of electron in electromagnetic wave is described by the Lorentz force

$$\frac{d\vec{p_e}}{dt} = \frac{d(\gamma m_e \vec{v_e})}{dt} = q(\vec{E} + \vec{v_e} \times \vec{B}) \tag{2.11}$$

where γ is the relativistic factor.

$$\gamma = \frac{1}{\sqrt{1 - v_e^2/c^2}} = \sqrt{1 + \frac{p^2}{m_e^2 c^2}} \tag{2.12}$$

Electric and magnetic fields are defined by Maxwell equations. Here, we use the vector potential $\vec{A}(\vec{r},t)$ in the Coulomb gauge $\nabla \cdot \vec{A} = 0$,

$$\vec{E} = -\frac{\partial \vec{A}}{\partial t}, \qquad \vec{B} = \nabla \times \vec{A}. \tag{2.13}$$

After using the vector identity $\vec{v} \times \nabla \times \vec{A} = \nabla(\vec{v} \cdot \vec{A}) - (\vec{v} \cdot \nabla)\vec{A}$, we obtain the first basic equation for electron momentum

$$\frac{d\vec{p_e}}{dt} = e\frac{\partial \vec{A}}{\partial t} + e(\vec{v_e} \cdot \nabla)\vec{A} - e\nabla(\vec{v_e} \cdot \vec{A}). \tag{2.14}$$

The second basic equation for electron energy is obtained by multiplying (2.14) with $\vec{v_e}$

$$\frac{d(\gamma - 1)m_e c^2}{dt} = e\vec{v_e} \cdot \frac{\partial \vec{A}}{\partial t}. \tag{2.15}$$

Considering plane electromagnetic wave of an infinite laser pulse propagating along the z-axis and the electron initially at rest, we have $\vec{A} = \vec{A}_\perp(z,t)$ and solve the set of equations (2.14), (2.15) to find electron momentum $\vec{p_e} = (p_\parallel, \vec{p}_\perp)$. Important conservation laws are obtained

$$\vec{p}_\perp - e\vec{A}_\perp = const \tag{2.16}$$

$$(\gamma - 1)m_e c^2 - p_\parallel c = const \tag{2.17}$$

where the first constant is usually called the canonical momentum. For the electron initially at rest, one has $const = 0$ on the right-hand side of Eqs. (2.16), (2.17). Finally, the following relations are found [45], [52].

$$p_\parallel = m_e c(\gamma - 1), \qquad p_\parallel = \vec{p}_\perp^{\,2}/(2m_e c). \tag{2.18}$$

Then, the angle θ of the electron motion owing to the direction of electromagnetic wave propagation is given by

$$\tan\theta = \frac{p_\parallel}{p_\perp} = \sqrt{\frac{2}{\gamma - 1}}. \tag{2.19}$$

In the nonrelativistic case, free electron simply oscillates in the electric field of the laser wave perpendicularly to its propagation vector $\vec{k}$. In the relativistic case, the $\vec{v_e} \times \vec{B}$ term of the Lorentz force (2.11) becomes significant as the electric field term, and for $\gamma >> 1$ the electron moves in the direction of laser wave.

The nonlinearity parameter of the laser plasma interaction is the dimensionless amplitude A_0 of the vector potential $\vec{A}$ of the electromagnetic laser wave. This dimensionless amplitude can be expressed as

$$a_0 = \frac{eA_0}{m_e c} = \frac{eE_0}{m_e \omega c}. \tag{2.20}$$

The trajectory of the electron initially at rest in the plane electromagnetic field of an infinite laser pulse depends on the polarization of the wave:

- **Circularly polarized electromagnetic wave**

This wave is expressed by the relation

$$\vec{A}_\perp(z,t) = (m_e c/e)a_0[\vec{e_x}\cos(\omega\tau) + \vec{e_y}\sin(\omega\tau)], \tag{2.21}$$

where $\tau = t - z/c$ is the retarded time. In this case, electron is moving along circular trajectory in the $x-y$ plane

$$\vec{r_e}_\perp(t) = (c/\omega)a_0[\vec{e_x}\sin(\omega\tau) - \vec{e_y}\cos(\omega\tau)]. \tag{2.22}$$

with drift velocity along z-axis

$$v_d = \frac{a_0^2}{a_0^2+2}c. \tag{2.23}$$

The explicit solution can be found for $\tau = t(1 - v_d/c)$. The electron trajectory in the circularly polarized laser wave is the spiral of radius $r_\perp = a_0 c/\omega$ and with the step along the wave propagation direction during one orbit $2\pi v_d/\omega$.

- **Linearly polarized laser wave**

In this case, the planar electromagnetic wave is described by

$$\vec{A}_\perp(z,t) = (m_e c/e)a_0\vec{e_x}\cos(\omega\tau) \tag{2.24}$$

The electron trajectory reads

$$kx_e(t) = a_0\sin(\omega\tau), \qquad kz_e(t) = \frac{a_0^2}{8}(2\omega\tau + \sin(2\omega\tau)) \tag{2.25}$$

with drift velocity along z-axis

$$v_d = \frac{a_0^2}{a_0^2+4}c. \tag{2.26}$$

Here, it is difficult to describe simply the electron trajectory. Therefore, the travel of electron is illustrated in the laboratory frame and in the moving frame in Fig. 2.1.

When we evaluate analytically the electron trajectory in the moving frame, the relativistic effects has to be taken into account. The oscillation frequency of electrons in the moving frame is reduced due to Doppler effect.

$$\omega' = \omega\sqrt{\frac{c-v_d}{c+v_d}} = \frac{\omega}{\sqrt{1+a_0^2/2}} \tag{2.27}$$

The phase $\omega\tau$ is invariant, thus $t' = t\sqrt{1+a^2/2}$. In the moving frame, we have

$$k'x'_e = \frac{a_0}{\sqrt{1+a_0^2/2}}sin(\omega' t'), \qquad k'z'_e = \frac{a_0^2/8}{\sqrt{1+a_0^2/2}}sin(2\omega' t') \tag{2.28}$$

We can generalize the electron motion for the case of finite laser pulse duration and amplitude a_0 which slowly varies in time. According to (2.22), (2.25), the electron returns to its initial position in the perpendicular plane, but it is moved in the direction of laser pulse propagation about the distance $\Delta z = \int v_d(t)\mathrm{dt}$. Thus, the electron is accelerated in the front of the pulse with increasing intensity and is decelerated when it feels decreasing laser pulse intensity. This acceleration in the direction of the intensity gradient is due to the ponderomotive force.

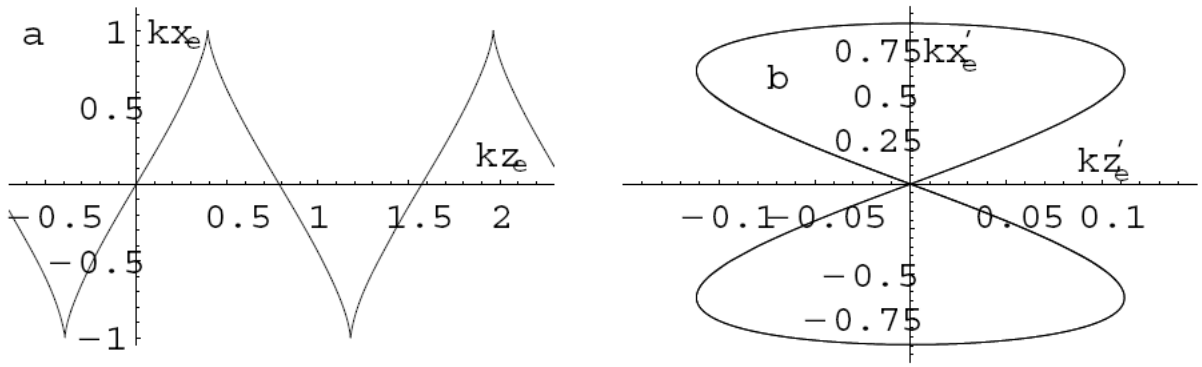

Figure 2.1: Demonstration of a free electron trajectory in the field of relativistic plane laser wave of infinite linearly polarized pulse: a) in the laboratory frame, b) in the moving frame along z-axis with drift velocity v_d

2.2.1 Ponderomotive force

As discussed above, the inhomogeneity of the field leads to a nonlinear force that a charged particle experiences [53]. By solving the equations (2.14), (2.15), the nonlinear force can be obtained

$$\frac{dp_{\parallel}}{dt} = -\frac{e^2}{2m_e\gamma}\frac{\partial \vec{A}_{\perp}^2}{\partial z} \tag{2.29}$$

This nonlinear force is proportional to the squared amplitude of the laser pulse, thus, it is, in general, composed of an averaged part and oscillating part with period π/ω, which is a half of the laser period. The equation (2.29) is rewritten into the following more general form with time-averaged momentum through a laser period $\langle\vec{p}\rangle$

$$\frac{d\langle\vec{p}\rangle}{dt} = \vec{F}_p = -\frac{e^2}{2m_e\langle\gamma\rangle}\nabla\langle\vec{A}^2\rangle, \tag{2.30}$$

where $\langle\gamma\rangle$ the relativistic average factor

$$\langle\gamma\rangle = \sqrt{1 + \langle\vec{p}\rangle^2/(m_e c)^2 + e^2\langle\vec{A}^2\rangle/(m_e c)^2} \tag{2.31}$$

taking into account average momentum $\langle\vec{p}\rangle$ and oscillation momentum $\vec{p}_{osc} = e\vec{A}/(m_e c)$. Eq. (2.30) can be simplified as only the part related to the oscillation momentum is the function of coordinates and $\langle\vec{p}\rangle$ is only the function of time

$$\vec{F}_p = -\frac{m_e c}{2\langle\gamma\rangle}\nabla\langle\gamma\rangle^2 = -m_e c^2\nabla\langle\gamma\rangle. \tag{2.32}$$

This is the force which can be defined by the gradient of potential $U_p = m_e c^2(\langle\gamma\rangle - 1)$. In the case of plane wave with a slowly varying amplitude, this force cannot accelerate electrons, thus any free charge cannot gain the kinetic energy from this laser pulse, which is is called Lawson-Woodward theorem. However, in reality, especially by assuming femtosecond laser pulses, which are usually tightly focused and their amplitude changes on a very short time scale, this theorem is not certainly valid.

2.3 Interaction of ultrashort intense laser pulse with plasma

2.3.1 Basic laser beam parameters

Circularly polarized laser wave propagating in vacuum along z-axis can be expressed by Eq. (2.21). This relation previously described infinite plane electromagnetic wave, but one can generalize that for short laser pulse by assuming $a_0 = a_0(\vec{r}, t)$ in the slowly varying envelope approximation [54], where $\vec{r} \perp z$. Similarly to the latter, one can generalize the relation (2.24) for linearly polarized laser pulse. However, there are two linear polarization cases. If the laser electric field oscillates in the plane of incidence (in the plane that contains the incident ray and the normal to the plasma-vacuum interface), the laser pulse is *p-polarized*. On the contrary, the laser pulse is *s-polarized* when the laser electric field oscillates perpendicularly to this plane. The corresponding relations for electric and magnetic components can be found by using Eq. (2.13) for all polarization cases.

The laser intensity is defined as the energy flux density averaged over the fast oscillations

$$I(\vec{r}, t) = \left\langle \left| \vec{E} \times \frac{\vec{B}}{\mu_0} \right| \right\rangle = \frac{\epsilon_0 c}{2} |E_0(\vec{r}, t)|^2, \tag{2.33}$$

where the relation between amplitudes of magnetic and electric field of the laser wave is $B_0 = E_0/c$. In the theory of femtosecond laser pulse interaction with plasma, the field amplitude a_0 given in dimensionless units is usually used and defined according to (2.20) Intensity is expressed in these units as

$$I\lambda^2 = a_0^2 \times 1.37 \cdot 10^{18} \ [\mathrm{W}\mu\mathrm{m}^2/\mathrm{cm}^2]. \tag{2.34}$$

Then, $a_0 = 1$ corresponds to the equality of the rest and averaged kinetic energy of electron oscillating in the laser wave. When $a_0 > 1$, electrons oscillating in the laser field has the quiver velocity v_{osc} close to the velocity of light c in free space and their motion is relativistic.

$$v_{osc} \approx \frac{eE_0}{\gamma_L m_e \omega}, \tag{2.35}$$

where the relativistic factor of laser field is

$$\gamma_L = \begin{cases} \sqrt{1 + \frac{a_0^2}{2}} & \text{for linear polarization} \\ \sqrt{1 + a_0^2} & \text{for circular polarization} \end{cases} \tag{2.36}$$

The relativistic average factor γ of electron is defined by (2.31). If the average electron momentum is much lower than the oscillation momentum ($\langle \vec{p} \rangle << e\vec{A}$), then $\gamma \approx \gamma_L$, where γ is the relativistic factor of electron.

To obtain a high intensity, the laser pulse is usually tightly focused onto the target. In the confocal area, a typical transverse laser pulse shape is usually assumed as [55]

$$I(r, z) = I_0 \left(\frac{w_0}{w} \right)^2 \exp - \left(\frac{|r|}{w(z)} \right)^2 \tag{2.37}$$

That is the most usual gaussian shape ($\exp(|r|/w_0)^n$, n=2), but super-gaussian shapes are also assumed (up to n=5). The laser beam current radius for a gaussian beam reads

$$w(z) = w_0\sqrt{1+(z/z_R)^2}, \tag{2.38}$$

where z_R is the Rayleigh length and w_0 is the waist of the laser beam (radius at the focal spot at $z = 0$)

$$z_R = \frac{1}{2}\frac{\omega w_0^2}{c} = \frac{\pi}{\lambda}w_0^2. \tag{2.39}$$

The laser beam divergence is

$$\tan\theta_0 = \lim_{z\to\infty}\frac{w(z)}{z} = \frac{w_0}{z_R} = \frac{2}{\pi}\frac{\lambda}{2w_0} \tag{2.40}$$

In the experiments, femtosecond laser pulses are usually focused to the beam width of several laser wavelengths at the focal spot, which means that the target positioning has to be quite precise to irradiate the target at the focal spot.

2.3.2 Propagation of a high-intensity laser beam in plasma

The plasma frequency ω_p (2.7) marks a fundamental boundary between conducting and dielectric behavior in the interaction of electromagnetic waves with plasmas. For light with frequency larger than ω_p, the inertia of electrons retards their response and the underdense plasma behaves like a dielectric. As a result, the underdense plasma is rather transparent to the radiation. When the incident laser frequency is lower than ω_p, the electrons can respond and exclude the incident field, resulting in a reflection of the wave from the so-called overdense plasma. The electron density at which the plasma frequency equals the laser frequency ω is called the critical electron density n_{crit}. This density denotes the boundary between underdense and overdense plasma.

$$n_{crit} = \frac{\epsilon_0 m_e \omega^2}{e^2} \tag{2.41}$$

The relativistic effect is equivalent to a reduction of the effective electron density $n_{eff} = n_e/\gamma_L$. As a result the plasma can be theoretically transparent in a so-called relativistic induced transparency regime [56] where

$$n_{crit} < n_e < \gamma_L n_{crit}. \tag{2.42}$$

We can also determine the dispersion relation of electromagnetic wave in plasma for relativistic case [52]

$$\omega^2 = \frac{\omega_p^2}{\gamma_L} + k^2c^2 \tag{2.43}$$

Numerical simulations [57] demonstrated that electromagnetic wave propagating in this regime is a subject of strong instabilities and heating of electrons that absorbs the energy of the propagating laser wave.

The instability of particular interest is the relativistic self-focusing of the laser beam. A typical laser pulse has a radial dependent shape of $I(r)$ with $dI/dr < 0$ and the corresponding radial dependent index of refraction is [56]

$$N_r(r) = \sqrt{1 - \frac{\omega_p^2(r)}{\gamma_L(r)\omega^2}}. \tag{2.44}$$

In this expression, ω_p is also supposed to depend on r, due to the ponderomotive force which tends to expel the electrons from regions of higher laser field amplitude, with $d\omega_p/dr > 0$. As a result of the γ_L and ω_p dependence on r, one has $dN_r/dr < 0$, and, thus, the plasma acts as a lens on the laser light. There exists a critical power [58]

$$P_{crit} \approx 17 \times 10^9 \frac{\omega^2}{\omega_p^2} \quad [W] \tag{2.45}$$

for which this lens effect dominates the natural diffraction given by the Rayleigh length in vacuum. Above the power P_{crit}, the laser light self focusses (the so-called relativistic self-focusing) into a filament [59] and can be self guided on long distances, much longer than the Rayleigh length.

2.3.3 Laser prepulse, preplasma formation, and rarefaction wave

In laser-matter interactions, plasma formation already starts at very moderate intensities of 10^{10} W/cm^2. When a high-intensity laser pulse hits any target, already the onset of the pulse many orders of magnitude below peak intensity is strong enough to ionize the target atoms and start plasma formation [59]. The main pulse is commonly preceded by picosecond prepulses and Amplified Spontaneous Emission (ASE) in the nanosecond time scale [60]. The picosecond prepulses originate from the imperfect isolation of the main pulse from its neighboring pulses in the master-oscillator or from the pulses leak from the early main pulse passes [61]. The picosecond prepulses can be almost completely cleaned away by using additional Pockles cells [62]. The ASE on the other hand is coming from the amplifier chain and it is a general feature found in all amplification systems operating based on population inversion process. ASE typically lasts for several ns and its intensity contrast ratio to the main pulse is a function exponentially growing with time up to about 10^{-6}. There exist special techniques to improve this intensity contrast ratio up to 10^{-10} using plasma mirror [63] or double plasma mirror [64]. These techniques inhibit preplasma formation which enables to employ ultrathin foils in experiments as will be discussed later.

The temporal scale on which preplasma is created (the duration of ASE or the separation of higher intensity femtosecond prepulse from the main laser pulse) is usually longer than the thermalization time for electrons and ions. It is thus reasonable to assume that both electrons and ions are in some kind of equilibrium, namely that they acquire Maxwell-Boltzmann energy distributions [65]. The temperature of preplasma generally ranges from several up to hundreds of eV. It is clear that the preplasma is not confined to the target surface but it starts to expand towards vacuum and form a density profile. This situation is described by the isothermal model of a freely expanding plasma [66], [67].

This one-dimensional model assumes ions at rest with the density $n_i = n_{i0}$ for $x < 0$ and $n_i = 0$ for $x > 0$. The electron density n_e is continuous and follows the Boltzmann distribution (2.9), $n_e = n_{e0} \exp(e\varphi/T_e)$, where n_{e0} is the electron density in the unperturbed plasma and T_e is a constant electron temperature. The potential satisfies the Poisson equation,

$$\frac{\partial^2 \varphi}{\partial x^2} = \frac{e}{\epsilon_0}(n_e - Z n_i), \tag{2.46}$$

while the ion expansion into a vacuum is described by the hydrodynamic equations of continuity and motion

$$\left(\frac{\partial}{\partial t} + v_i \frac{\partial}{\partial x}\right) n_i = -n_i \frac{\partial v_i}{\partial x}, \qquad \left(\frac{\partial}{\partial t} + v_i \frac{\partial}{\partial x}\right) v_i = -\frac{Ze}{m_i} \frac{\partial \varphi}{\partial x}, \tag{2.47}$$

where v_i is the ion velocity. A self-similar solution of this set of equations depending on the self-similar variable $\xi = x/t$ can be found, if one assumes the quasi-neutrality condition $n_e = Z n_i$. This solution describes the rarefaction wave:

$$Z n_i = n_{e0} \exp(-\xi/c_s - 1), \qquad v_i = c_s + \xi, \qquad e\varphi = -T_e(\xi/c_s + 1). \tag{2.48}$$

Here, $x = 0$ is the sonic point and also the original position of the plasma surface. The solution is valid for $x > x_u = -c_s t$, where x_u is the upstream front of the rarefaction wave, which propagates with the ion-acoustic velocity, $c_s = \sqrt{ZT_e/m_i}$, and terminates with the shockfront. However, these aspects of the rarefaction wave will be discussed later in the section describing ion acceleration from the rear foil surface. At this moment, it is sufficient to say that the isothermal expansion model results in an exponential density profile on the target surface.

The exponential density profile is widely used as a starting point for numerical simulations and analytical models for its simplicity. In the case of small-size targets, a sufficiently high laser pulse contrast which avoids the formation of a larger preplasma is strongly desirable as the target heating by the prepulse could lead to the expansion of a small target before the main pulse arrives. Thus, we usually assume initially a step-like density profile or the exponential one with a very small characteristic scale length.

2.4 Electron acceleration mechanisms at the critical surface

For very low laser intensities, the plasma is gradually heated due to electron-ion collisions. Related absorption mechanisms, such as normal skin effect, anomalous skin effect, collision absorption (inverse bremstahlung), etc. [61] lead to the heating of all electrons. For efficient collisional heating, many collisions must take place in the interaction region on the temporal scale of the laser pulse duration. This is usually fulfilled for low laser intensities (below 10^{15} W/cm^2) and relatively long laser pulses (ns). In such case collisional absorption can be very efficient and results in the transfer more than 80% of the laser pulse energy into plasma [50].

At laser intensities higher than 10^{16} $\mathrm{W/cm^2}$, collisionless absorption mechanisms dominate. Resonance absorption takes place when a p-polarized laser pulse is obliquely incident on a gradually rising plasma density. The laser wave penetrates through the underdense plasma up to the surface of electron density $n_e = n_{crit}\cos^2(\alpha)$, where the reflection occurs (here, α is the incidence angle of the laser on plasma-vacuum boundary; $\alpha = 0$ for normal incidence). Laser field skins from the reflection surface to the critical density surface where it resonantly excites an electron plasma wave. This wave propagates into the underdense plasma and it is damped either by collisions and Landau damping at lower intensities of by particle trapping and wave breaking at higher intensities. The latter gives rise to population of very fast electrons. This is an essential difference between collisional and collisionless heating mechanisms. A minority of plasma electrons acquires most of the absorbed energy in contrast to the collisional heating, which heats all of the electrons. Up to about 50% absorption may occur by resonance absorption. However, this mechanism efficiently works only for a large scale plasma density profile, which is not our case where the plasma density profile is step-like or, at least, very steep. Here, the absorption of laser energy is due to the Brunel vacuum heating or $j \times B$ heating, which will be discussed in this section in more detail.

2.4.1 Hot electron population

In the theory of the interaction of a femtosecond laser pulse with overdense plasma, the electrons heated by collisionless mechanisms are called "hot" as their kinetic energy is much higher then the energy of thermal electrons named "cold". Because of a high relaxation time of hot electrons compared to the plasma expansion time, two-temperature electron distribution is usually assumed in the plasma initially after the interaction. The electron density n_e can be considered as a sum of two Boltzmann distributions with cold (T_c) and hot (T_h) electron temperatures [67]

$$n_e = n_c + n_h = n_{c0}\mathrm{e}^{e\varphi/T_c} + n_{h0}\mathrm{e}^{e\varphi/T_h}, \tag{2.49}$$

where φ is the electrostatic potential. The hot electron temperature is estimated from the ponderomotive potential

$$T_h \approx U_p = m_e c^2(\langle\gamma\rangle - 1) \approx m_e c^2\left(\sqrt{1+\frac{a_0^2}{2}} - 1\right)[MeV], \tag{2.50}$$

although this scaling is still under debate. For example, in Ref. [68], T_h is found experimentally to increase as $(I\lambda^2)^{0.34\pm0.04}$ for laser intensities ($I\lambda^2$) from 10^{18} to 10^{21} $\mathrm{W/cm^2}\mu\mathrm{m}^2$ and laser pulse duration 400 fs (FWHM), which suggests that the ponderomotive scaling $(I\lambda^2)^{0.5}$ overestimates hot electron temperature growth with laser intensity.

2.4.2 Brunel vacuum heating

In this scenario, a p-polarized laser pulse is obliquely incident on the surface of plasma with a step-like density profile. This mechanism works for high laser intensities when the amplitude of oscillating electrons in the laser field, $r_e = a_0 c/\omega$ is larger than the density

scale length. Assuming that the plasma is overdense in the region $z < 0$, the electric field of obliquely incident laser wave is composed of the part oscillating perpendicularly to the plasma surface $E_z(t) = E_p \sin(\omega t + \phi)$, where $E_p = E_0 \sin\alpha$, and the part oscillating parallel to the surface, where α is the incidence angle of the wave. We can define dimensionless amplitude of the field oscillating perpendicularly to the surface $a_p = a_0 \sin\alpha$, where a_0 is given by (2.20).

In the fist half laser cycle ($0 < \omega t + \phi < \pi$), $E_z > 0$, electrons are pushed inside the plasma and they can gain only very low energy because the electric field is strongly attenuated in plasma. On the contrary, in the second half laser period ($\pi < \omega t + \phi < 2\pi$), $E_z < 0$ and electrons are ejected into vacuum. They can gain very high energy of the order of ponderomotive potential $U_p = m_e c^2(\sqrt{1 + a_p^2} - 1)$. The trajectory of an electron ejected by the laser electric field depends on the time of ejection. Many electrons are ejected at the same time and they create self-consistent electric field. Due to the action of this self-consistent field and oscillating laser field, most accelerated electrons turn back into the plasma, where they feel no restoring forces after the passing of a thin skin layer.

One can estimate that the self-consistent electric field should be of the order of E_p and the energy of the electrons of the order of U_p. Then the number of ejected electrons δN_e and the thickness of the ejected layer d can be estimated from the following relations

$$E_p \simeq e\delta N_e d/\epsilon_0, \qquad eE_p d \simeq U_p. \tag{2.51}$$

This relations give the estimates of the number of ejected electrons per unit surface $\delta N_e d$. Multiplying the latter with the energy U_p and taking into account that the ejection of electrons run over approximately a quarter of the laser period $\sim \pi/2\omega^{-1}$, the absorbed power per time unity can be obtained in dimensionless units

$$W_{abs} \sim \frac{0.05 m_e^2 c^3 \epsilon_0 \omega^2}{e^2} a_p(\sqrt{1 + a_p^2} - 1). \tag{2.52}$$

In the non-relativistic case, $a_p << 1$, and the absorbed energy is proportional to a_p^3, whereas the absorbed energy is proportional to a_p^2 in the relativistic regime. W_{abs} divided by the laser intensity $\frac{1}{2}\epsilon_0 c E_0^2 \cos\alpha$ gives the absorption coefficient

$$A_B \sim 0.05 a_0^{-1} \tan(\alpha)(\sqrt{1 + a_0^2 \sin^2(\alpha)} - 1). \tag{2.53}$$

Eq. (2.53) predicts more efficient absorption by larger incidence angles of p-polarized laser pulse. The analysis above is only qualitative as the reflected pulse and the finite focal spot of the incident laser beam are not included. However, the validity of this relation has been verified by numerical simulations for very short laser pulses when the ions can be assumed as immobile [45]. The absorption coefficient A_B rarely exceeds 10% and another mechanism, $j \times B$ heating, is usually more efficient in the relativistic case, because the Brunel heating is efficient only during a small part of laser period and requires large incidence angles.

The energy deposed by Brunel heating is transported by hot electrons in the bunches ejected once per laser period. The average energy of electrons is $\varepsilon_e \sim U_p$ and their energy distribution can be considered as maxwellian because the electrons are accelerated in different phases of the laser electric field.

2.4.3 $j \times B$ heating

For the normal incidence of laser pulse onto the target, the oscillating electric field perpendicular to the plasma surface E_p is zero. If the laser pulse intensity is sufficiently large (relativistic), the $v \times B$ component of the Lorentz force (2.11) becomes important and can heat electrons similarly to the Brunel effect.

Considering a laser wave incident normally with the potential vector $A_0 = m_e c a_0/e$ and the laser frequency ω, the momentum in the perpendicular plane $p_\perp = eA_0$ can be obtained from Eq. (2.16), and the magnetic field $B_0 = \omega A_0/c$. Then, one can estimate the force in the normal direction

$$F_p \sim m_e \omega c a_0^2/\sqrt{1+a_0^2} \tag{2.54}$$

which ejects electrons into vacuum two times per laser period. Due to the action of the self-consistent field created by ejected electrons and the oscillating force of the order of F_p, the electrons return back into the plasma, where they feel no restoring forces after the passing of a thin skin layer. Similarly to (2.51), one can estimate the number of ejected electrons δN_e and the thickness of ejected layer d on the basis of the following relations

$$F_p \simeq e^2 \delta N_e d/\epsilon_0, \qquad F_p d \simeq U_p. \tag{2.55}$$

Here, the characteristic energy of the electrons is $U_p = m_e c^2(\sqrt{1+a_0^2}-1)$.

The absorption coefficient is obtained by dividing the energy transferred to electrons during a laser period $U_p \delta N_e d\omega/4\pi$ (assuming that the ejection takes half laser period) over laser pulse intensity $\frac{1}{2} c\epsilon_0(\omega A)^2$

$$A_a \sim \frac{1}{2\pi}\left[1 - \frac{1}{\sqrt{1+a_0^2}}\right]. \tag{2.56}$$

For relativistic laser intensity ($a_0 > 1$), this model predicts a constant value of absorption about 15%. In the case of oblique incidence of s-polarized laser pulse, the Eq. (2.56) can be simply multiplied by factor $1/\cos\alpha$ taking into account the decrease of Poynting vector (energy flux) in the perpendicular direction to the plasma surface. The estimated average energy of electrons is $\varepsilon_e \simeq U_p$, similarly to Brunel heating. On the contrary, the bunches of hot electrons are ejected twice per laser period. Due to this feature, one can distinguish between Brunel and $j \times B$ heating in numerical simulations.

2.4.4 Angular distribution of fast electrons

The main direction of fast electron ejection into vacuum and injection in plasma (as the electron momentum is reversed) depends on kinetic energy of particles and laser pulse incidence angle. Theoretical estimate [69] assuming that the momentum is conserved along the target surface between the absorbed photons and accelerated electrons gives the relation between the electron angular direction θ and the laser pulse incidence angle α (see Fig. 2.2)

$$\sin\theta = \sqrt{\frac{\gamma_L - 1}{\gamma_L + 1}}\sin(\alpha). \tag{2.57}$$

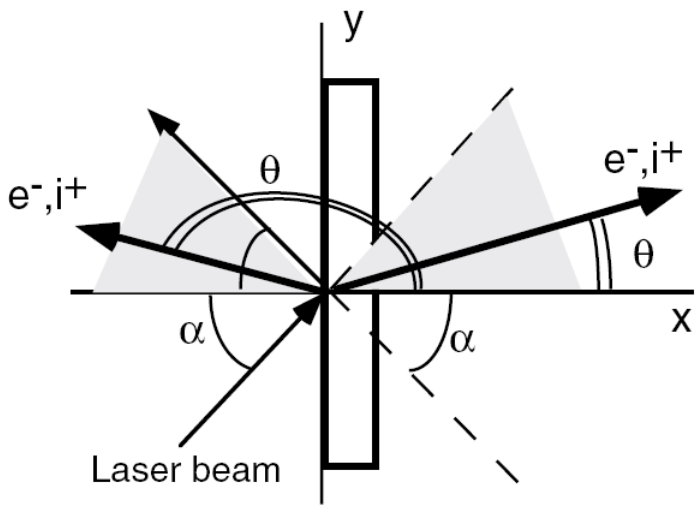

Figure 2.2: Schematic drawing of the laser-target interaction and predicted electron emission angle according to the theory in Ref. [69].

Thus, the increasing laser intensity is translated into a higher electron momentum, i.e. a higher relativistic factor γ, according to Eq. (2.31), leads to the angular direction closer to the incident laser beam direction.

Since electrons are relatively easy to escape from the target during and after the interaction with laser pulses, the target is usually positively charged. Taking into account the potential jump $\delta\Phi = e\delta\varphi_s/(m_e c^2)$ at the target surface, the following relation is obtained [69]

$$\tan(\theta) = \pm\sqrt{\frac{2(\gamma_L - 1)(1 + \delta\Phi) - \delta\Phi^2}{(\gamma_L - 1 - \delta\Phi)^2}\sin^{-2}(\alpha) + \tan^{-2}(\alpha)}. \tag{2.58}$$

For positively charged targets, $\delta\Phi > 0$ for all particles. In this case, electrons are expected to appear in grey-colored regions in Fig. 2.2.

The experimental measurements indicate a hot electron emission predominantly in the target normal direction for moderate laser intensities ($a_0 < 1$) and in the incident laser direction for relativistic intensities ($a_0 > 1$) [70]-[72], thus they are in agreement with theoretical analysis. However, experiments also show their considerable angular spread. The measurements of the electron beam divergence from metallic foils [73]-[76] show that it depends strongly on particular experimental conditions and the results spread from $\theta \sim 25^\circ$ to $\theta \sim 50^\circ$. In this case, no correlation has been found with the focused laser intensity.

2.4.5 Propagation of hot electrons inside the target

The laser-produced relativistic electron beams are characterized by a very high charge and current density. They carry around $\sim 30\%$ of the laser energy with current densities of $\sim 10\,\mathrm{kA}/\mu\mathrm{m}^2$ [77]. At such high current densities, the self-consistent electromagnetic fields reach values $E \sim 1\ \mathrm{TV/m}$, $B \sim 10\ \mathrm{kT}$ and the beam propagation is only possible if the beam is neutralized by free background electrons. The neutralizing current of free electrons is called the return current.

In initially ionized target layers (thus, in plasma) and inside metals, these free background electrons are easily accessible. They are naturally present since the beginning of electron beam propagation. In the insulators, all electrons are in a bound state at room temperature, the return current must be generated by processes breaking the local thermodynamic equilibrium, such as the electric field ionization, or collisions between atoms and the beam electrons. In our particular conditions, we consider a high conductivity thin target, and the appropriate model of collective transport of plasma electrons. That means that the fast electrons of the beam are assumed collisionless and evolve in the self-consistent electromagnetic field.

Let us consider a monoenergetic electron beam with a finite radius r_b, homogeneous density n_b, and with the velocity v_b. Such a beam creates, in the laboratory frame, the transverse electric field $\vec{E}_\perp = -\frac{e}{2\epsilon_0} n_b r$ in the radial direction which leads to a repulsion between the electrons and the transverse magnetic field $\vec{B}_\perp = -\frac{1}{2} e \mu_0 n_b v_b r$ in the azimuthal direction which attracts them. If the beam velocity approaches the velocity of light, the Lorentz force (2.11) tends towards zero - the beam does not spread radially.

It has been found [78] that there is a maximum uncompensated current that can be transported in vacuum. The reason for this limiting current is that the magnetic field near the edges of the electron beam would otherwise be so strong that it deflects electrons near the beam edges inhibiting their further propagation with the beam. Alfven current depends only on the energy of beam electrons and it reads

$$I_A = \frac{4\pi\epsilon_0 m_e c^2 \gamma v_b}{e} \approx 17 \frac{\gamma v_b}{c} \ [\mathrm{kA}]. \tag{2.59}$$

In the laser-plasma interaction, the laser-induced beam currents are around ~ 10 MA for electrons with energies of several hundred keV, which certainly exceeds the Alfven current. Nevertheless, their propagation occurs over distances of several hundred of μm [77], which is explained by an almost complete neutralization of the charge density and current density of the incident beam by free plasma electrons, i.e., by the return current.

Qualitatively, the beam charge accumulation in the plasma rises the longitudinal electric field $E_\parallel$ which accelerates backwards the plasma electrons. One can estimate the time of response of the electron plasma density by using Poisson equation coupled with the total charge continuity equation, and the Ohm's law

$$j_r = \sigma E_\parallel \tag{2.60}$$

where σ is the conductivity of the target material. The characteristic relaxation time is $\tau_E = \epsilon_0/\sigma$, which provides very fast charge density response, for example, for cold metals around $\tau_E \sim 1$ as [77].

The system consisting of an electron beam and a return current formed by free electrons is in general unstable. A current beam perturbation affects the electromagnetic field distribution and modifies the return current shape. This effect further amplifies the perturbation of electromagnetic field, the incident hot electron beam deformation is enhanced, and it grows exponentially.

In our case, the most important is the Weibel instability [79]. This instability occurs due to the beam density perturbations in the direction perpendicular to the beam propagation,

which create the transverse components of the electromagnetic field. Then, the focusing effect of the magnetic field is amplified and it enhances the beam current perturbation. The Weibel instability has the growth rate proportional to n_{b0}/n_{e0}, where n_{b0} is the unperturbed electron beam density and n_{e0} the plasma density, respectively. Therefore, the instability can be excited near the beam source, where the hot electron beam density is high and the electron plasma density can be small. In this case, the beam splits into filaments with the characteristic size of $\sim 0.1 - 1\ \mu\mathrm{m}$. On the contrary, this transverse instability is stabilized by the low ratio of n_{b0}/n_{e0} and the wide initial angular spread of hot electron distribution [80].

2.4.6 Guiding of hot electrons along the surface and their acceleration

Surface electron current

When an intense laser pulse is incident obliquely on a solid surface with a steep density gradient, quasi-static surface magnetic fields can be induced. In such case ($\gamma_L > 1$), the angle of fast electron injection into the target θ should be close to the incidence angle of the laser beam α according to (2.57). However, the angle of electron injection is modified by the surface magnetic field in the opposite direction than by the electrostatic potential jump included in Eq. (2.58). Since the quasistatic magnetic field is along the z direction, the associated vector potential is $\vec{A_{s0}} = A_{s0y}\vec{e_y}$. Ref. [29] includes this field into the normalized potential variation $\delta\Phi = e(\delta\varphi_s - \delta A_{s0y}/\sin\alpha)/(m_e c^2)$, where $\delta\varphi_s(x)$ and $\delta A_{s0y}(x)$ denote the scalar and vector potential changes experienced by the particles. Now, $\delta\Phi$ can be also negative and the electron emission angle may lay outside the grey-colored region in Fig. 2.2.

The mechanism of the surface magnetic field generation is explained as follows [28]. When an intense laser pulse is incident obliquely on a solid surface with a steep density gradient, fast electrons are injected into the plasma due to the vacuum or $j \times B$ heating. The accelerated electrons form a jet along the laser beam direction to induce magnetic fields. When a sufficiently intense magnetic field is generated along the surface, a significant fraction of fast electrons is reflected back to the vacuum by the magnetic field. They are reflected back from the vacuum region because of a negative space charge in the vacuum. Therefore, these electrons are confined on the surface in a potential well, see Fig. 2.3B, and provide a surface current that enhances the surface-magnetic field. In this way, the positive feedback is established and it sustains the surface current and magnetic field. The lateral flow direction is in the direction of the projection of laser wave vector onto the target surface. There is also an induced return current, which flows inside the critical surface, whereas the surface current flows in front of it, see Fig. 2.3B.

The maximum magnitude of the surface-magnetic field is evaluated as [28]

$$B_{s0} \simeq 2\pi\eta(1-\xi)\frac{R}{\lambda}\frac{a_0^2}{\gamma_L^2(\gamma_L - 1)}B_0, \tag{2.61}$$

where η is the energy absorption coefficient, ξ is the transmittance of electrons through the surface magnetic field, R is the laser beam spot size, and B_0 is the laser field amplitude. The transmittance $\xi = \xi(\theta)$ depends on the injection angle of electrons (here, the relativistic case is usually assumed, where $\theta \approx \alpha$ according to (2.57)). Thus, the transmittance decreases with

the increasing incidence angle α. This is clear from the following relation by considering the orbit of an electron in a uniform magnetic field B_s with extent L_B. One finds that the electron is reflected back (thus, the electron is not transmitted through the surface layer), if its initial momentum

$$p_{in} < \frac{eB_s L_B}{1 - \sin\theta} \tag{2.62}$$

The problem of surface electron guiding has been well illustrated, for example, in 2D PIC simulations in Ref. [34]. There, 2 μm thick targets of density 50 n_{crit} are irradiated by p-polarized laser pulses with wavelengths of 1 μm, intensity of 1.0×10^{19} W/cm^2 which is uniform in y direction. There is also considered preplasma at the target front where the density profile is assumed to be exponential as $n_e \sim \exp(-x/l_{sc})$ with the scale length $l_{sc} = 0.1$ μm. Boundary conditions are the absorbing in the x direction, and periodic in the y direction. The initial electron temperature is 500 eV, and ions are assumed to be immobile.

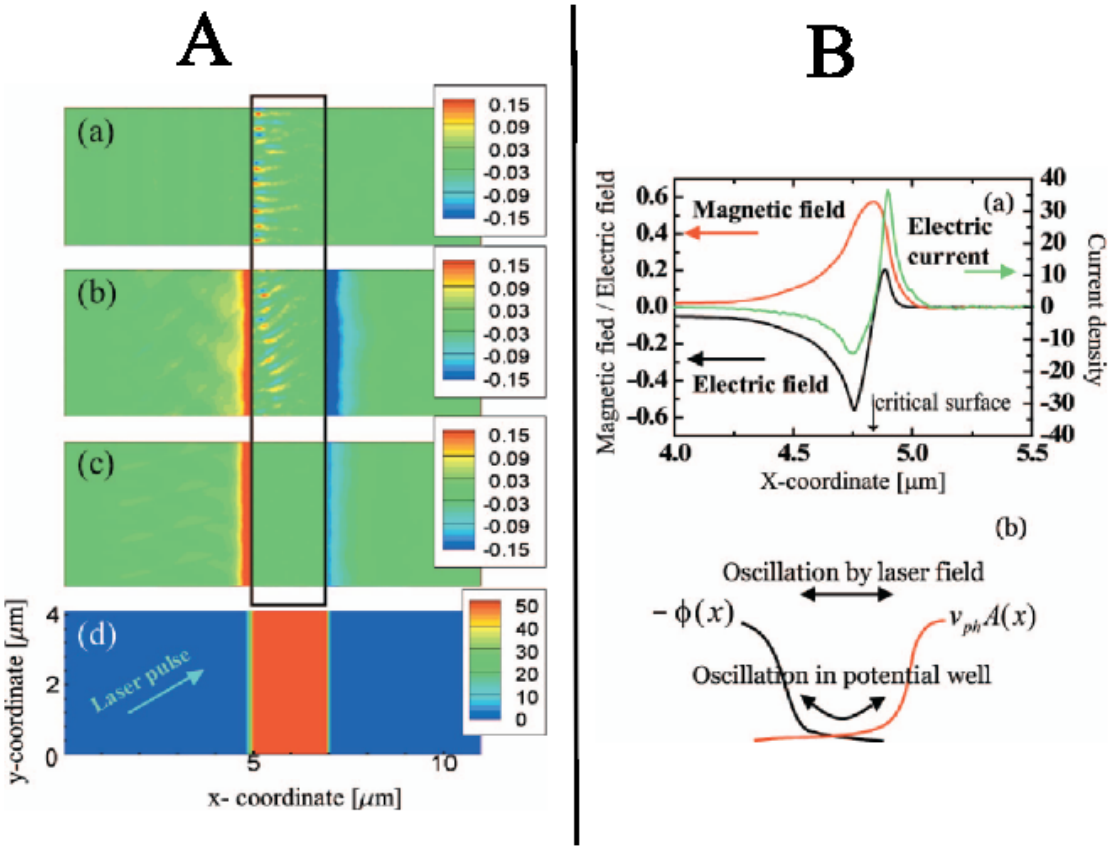

Figure 2.3: A (left panel) - Spatial profile of the quasistatic magnetic field for (a) normal incidence, (b) 45° incidence, (c) 75° incidence, where magnitude is normalized by that of the laser magnetic field. (d) The initial density profile which is normalized by the critical density. B (right panel) - (a) Spatial profile of the surface fields for the 75 ° incidence case which is a transverse cut at y=2.59 μm. The electric and magnetic fields are normalized by the laser electric and magnetic fields. The electric current density is normalized by $en_{crit}c$. (b) Schematic figure showing the surface acceleration mechanism in the moving frame along y-axis (target surface) with accelerated electron. The figure is taken from [34].

Spatial profiles of the quasistatic magnetic fields are shown in Fig. 2.3A. In the case of normal incidence, electron jets are formed by the oscillating part of the nonlinear force (2.29) in the parallel direction and the quasistatic magnetic field is generated inside the target due to the Weibel instability - the jets break-up and are merged into current filaments. In the 45° incident case, the magnetic field is observed both inside and on the surface of the target. Namely, some fraction of the electrons penetrate into the target and others flow along the surface. With increasing incidence laser angle to 75°, the magnetic field is observed only along the surface. Thus, the majority of electrons is guided along the surface in this case. The simulation demonstrates that the surface quasi-static magnetic field can reach up to $\sim 50\%$ of the laser field for large incidence angles.

Experiments with foils demonstrated dependencies of the guiding effect on the prepulse level [30], [31] and on the laser intensity [32], [33]. The hot electron guiding was observed only at relativistic laser intensities and for a very steep plasma density profile, although these both conditions are related. No evidence of fast electron transport was reported in Ref. [81]. There, a high intensity s-polarized laser pulse $I = 10^{20}$ W/cm^2 at the wavelength $\lambda = 1.054$ μm was interacting with the foil surface at oblique incidence and fast electrons were detected by x-ray fluorescence. This fact can be explained by a too strong laser prepulse that created a preplasma with the scale length of about 100 μm at the front side of the target. It destroyed the electron guiding, because desired strong electric and magnetic fields can be formed only at a sharp plasma-vacuum interface. Moreover, the laser energy absorption by plasma electrons is due to either vacuum or $j \times B$ heating mechanisms. Their efficiency depends on the ratio of the characteristic preplasma scale length L to the quiver length of electrons in the laser wave l_{osc}. In the case of steep plasma profile, $l_{osc} >> L$, the dominant absorption mechanisms are the vacuum heating and $j \times B$ heating, necessary for forming of the electron surface current. On the contrary, in the limit $l_{osc} << L$ (which is the case of Ref. [81]), the laser energy is dissipated due to the resonance absorption [50], which produces electron currents in the direction normal to the target surface.

Acceleration of confined electrons along the surface

Due to the presence of the surface fields, which tend to keep electrons around the critical surface, the electrons confined inside the potential well can be further accelerated by wiggling inside the static and laser fields [34], which is illustrated schematically in Fig. 2.3B. A similar situation was studied in electron acceleration inside a laser channel created in gas plasmas, which is called betatron acceleration [82], [83]. The major difference is in the fact that the phase velocity of the laser field propagating along the target surface $v_{ph} = c/\sin\alpha$ depends on the angle of incidence.

The equation of transverse motion for an electron confined inside the potential well created by static magnetic $B_z^s = -\kappa_B x/c$ and electric $E_x^s = \kappa_E x$ fields, and in the laser field $E_x^L = E_0 \sin(\alpha) \cos[\omega(t - y/v_{ph})]$, $B_z^L = E_x^L/v_{ph}$ can be written as [82]

$$\frac{d^2x}{dt^2} + \omega_\beta^2 x = \frac{e}{m_e\gamma}\left[\frac{1}{c^2}\left(\frac{dx}{dt}\right)^2 - \left(1 - \frac{v_y}{v_{ph}}\right)\right] E_x^L + \frac{e}{m_e\gamma c^2}\left(\frac{dx}{dt}\right)^2 \kappa_E x. \qquad (2.63)$$

This is an equation of a driven oscillator with the eigenfrequency

$$\omega_\beta^2 = e(\kappa_E + v_y c\kappa_B)/(m_e\gamma) \qquad (2.64)$$

corresponding to betatron oscillations in the static electric and magnetic fields. The driving force on the right hand side of Eq. (2.63) hits the resonance when

$$\omega_\beta/\omega = 1 - v_y/v_{ph}. \tag{2.65}$$

This resonance condition states that when an electron makes one oscillation, the laser wave propagating along the target surface with $v_{ph} > c$, overtakes it exactly by one period. When the resonance condition is satisfied, the energy and the longitudinal momentum (along the target surface) of electron increase.

The resonance can only be achieved for sufficiently strong surface quasi-static fields. The necessary condition for the electron trapping in the acceleration phase reads [46]

$$\kappa_E,\, \kappa_B > \frac{m_e}{e}\omega^2\gamma_{e0}\frac{5\beta_{ph}^2 + 4 - 3\beta_{ph}\sqrt{\beta_{ph}^2+8}}{2\beta_{ph}^2} \approx \frac{4m_e}{9e}\omega^2\gamma_{e0}\cos^4\alpha, \tag{2.66}$$

where $\beta_{ph} = v_{ph}/c = 1/\sin\alpha$ is the wave phase velocity and γ_{e0} is the particle initial energy. Moreover, the initial electron energy has to satisfy the condition

$$\gamma_{e0} \gtrsim \sqrt{3}/\cos\alpha \tag{2.67}$$

Once the electron is trapped, its average energy increases with the acceleration length and the laser field amplitude $T_{ef} \propto a_0 l_{acc}$ as it was reported in Refs. [34], [82].

The acceleration of electrons along the target surface has been demonstrated by numerical PIC simulations in Ref. [34]. Here, in order to increase the interaction length without substantial losing laser intensity due to larger laser spot size, a capillary type target is proposed. This scheme considers two laser pulses irradiating the capillary inner surface at large incidence angles. In such a case, the simulation demonstrates the acceleration of electrons up to $50\ \mathrm{MeV}$ for the laser pulse intensity $4 \times 10^{19}\ \mathrm{W/cm^2}$ and the capillary length $60\ \mu\mathrm{m}$. According to the author's knowledge, convincing experimental results confirming the theory of this electron acceleration have not been obtained yet since most experiments have been interested in the electron emission directions, but not in the dependence of electron energy on the emission direction. Somewhat enhanced temperature of electrons emitted along the foil surface is reported only in Ref. [33] for a relatively low laser intensity reached in this experiment about $3 \times 10^{18}\ \mathrm{W/cm^2}$. For more convincing experimental results, higher laser pulse intensities and larger spot sizes are required.

2.4.7 Conclusion

When an intense femtosecond laser pulse ($I\lambda^2 \gtrsim 10^{18}\ \mathrm{W}\mu\mathrm{m}^2/\mathrm{cm}^2$) is interacting with plasma, its amplitude is high enough to accelerate electrons within half of the oscillation period to energies comparable or even higher than their rest energy. In this case, collisional absorption mechanisms, which take place for lower intensities, are not further efficient as the collisional frequency is proportional to $\sim v_e^{-3}$, thus, it is strongly reduced for relativistic electrons with velocity $v_e \approx c$. The absorption of laser pulse energy is due to collisionless mechanisms. These mechanisms give rise to population of very fast (hot) electrons characterized by very high temperatures of the order of ponderomotive potential. The accelerating

mechanisms of electrons at the surface of plasma with a step-like density profile are the Brunel vacuum heating due to oscillating electric field perpendicular to the plasma surface or $j \times B$ heating due to the oscillating Ampere's force ($v \times B$ component of the Lorentz force).

Accelerated electrons propagate in the directions ranging from the normal of the surface in non-relativistic case towards the incident laser pulse direction with increasing laser intensity. Experiments have shown a large angular spread of electrons up to $\sim 50°$. The hot electron current is neutralized by the return current of background plasma electrons, their difference cannot exceed the Alfven limit, of several tens of kA. The direction of electron propagation can be modified by quasi-static magnetic and electric fields on the target surface. For large incidence angles, hot electrons can be guided along the front foil surface due to the static fields. Then, these electrons can be further accelerated in the potential well formed by the static fields due to the action of laser fields.

In summary, this section contains mostly a review of theories describing the interaction of relativistically intense laser pulse with a sharp plasma-vacuum boundary and propagation of hot electrons. Some experimental results are also presented. Our new contribution is in the last part which reviewed recent works on the guiding of hot electrons along the foil surface and their possible acceleration to energies exceeding the ponderomotive potential. We applied the theory of betatron acceleration in laser channels on the acceleration of hot electrons trapped along the foil front surface by the static magnetic and electric fields and completed the theory in Ref. [34]. The lateral electron transport of hot electrons in this foils and their influence on ion acceleration has not been fully described yet, thus we devoted one chapter of the thesis to this problem (see Chapter 6) which summarizes our effort in this domain.

2.5 Ion acceleration in solid targets

The direct interaction of protons and heavier ions with laser light at presently achievable intensities is by far not strong enough to accelerate these particles to MeV energies. Similarly to (2.34), with the relativistic threshold for electrons $I_e\lambda^2 = 1.37 \times 10^{18}$ [Wμm^2/cm^2], one can derive the intensity when the kinetic energy of an oscillating proton in the laser field is equal to its rest energy [59]

$$I_p\lambda^2 = \left(\frac{m_p}{m_e}\right)^2 I_e\lambda^2 \approx 5 \times 10^{24} \quad [\mathrm{W}\mu\mathrm{m}^2/\mathrm{cm}^2] \tag{2.68}$$

This intensity is far beyond the present laser technology.

However, the plasma electrons can mediate the forces of laser fields on ions by generation of strong and quasistatic electric fields arising from local charge separations. These fields can be of the same magnitude as the fast oscillating laser fields, but they vary on a time scale comparable to the laser pulse duration giving the ions a significantly longer time to be accelerated.

In this section, the two main ion acceleration scenarios will be described, that can both provide sufficiently strong electric fields over a sufficiently long time. According to these two scenarios, ions can either be accelerated in the vicinity of the laser focus at the target front

side, where the ponderomotively expelled electrons leave behind a positive space charge of ions, or at the target rear side, where the electrons, that have been accelerated by the laser on the front side and have propagated through the target, form a thin Debye sheath, that also provides strong and long lasting electric fields.

2.5.1 Ion acceleration at the target front side

This mechanism accelerates ions at the front side of the target in the vicinity of the laser focus due to electrostatic fields arising from the ponderomotive expulsion of plasma electrons from regions of high laser intensities inside the target, where they form a compressed electron cloud. The front-side ion acceleration is also called radiation pressure acceleration as the ponderomotive force (2.32) drives it. When the main pulse arrives at the relativistic critical surface, electrons are pushed inward, until the electrostatic potential arising from the charge separation balances the ponderomotive potential (2.50). This can be expressed by the balance between the total radiation and electrostatic pressure

$$\frac{1}{2}\epsilon_0 E_{es}^2 = \frac{1+R}{c} I_L \simeq \frac{2}{c} I_L, \tag{2.69}$$

where E_{es} is the electrostatic field due to the charge separation, I_L laser pulse intensity, and R is the target reflectivity (we further assume $R \simeq 1$). Electron depletion layer is established at the target front followed by the compressed electron cloud in the target interior. Ions in the depletion layer which experience the charge separation field E_{es} can be accelerated to maximum energy [84], [85]

$$\varepsilon_{imax} \simeq \frac{Z m_e c^2 a_0^2}{m_i \gamma_L}. \tag{2.70}$$

The front-side acceleration is expected to produce a large-divergence ion beam because the critical density interface where the charge separation occurs is curved by the transverse laser beam shape (2.37). If the laser pulse is linearly polarized, it has been found experimentally and numerically that rear-surface acceleration (TNSA) produces higher energy particles with smaller divergence and a higher efficiency than the acceleration at the target front [3], [85], [86]. On the contrary, circularly polarized laser beams at normal incidence on a foil may inhibit most electron heating mechanisms (resonance absorption, vacuum heating, $j \times B$ heating) and radiation pressure acceleration mechanism becomes dominant.

The essential difference between circularly and linearly polarized laser wave is the absence of the oscillating part of the nonlinear force (2.29), which means that electrons can rest in the field of circularly polarized laser wave in the interaction zone, that is, they are not heated. Then, the ion acceleration may continue further as the target expansion is inhibited. Once all ions from the electron depletion layer at the target front are accelerated and enter the non-perturbed target, the electron cloud is pushed deeper into the target as well. This process lasts until the moment when the compressed electron cloud reaches the position of the former rear target surface. Indeed, one-dimensional numerical simulations demonstrated that the radiation pressure of laser beam (intensity more then 10^{20} $\mathrm{W/cm^2}$) may accelerate whole ionized ultrathin foil (initial thickness of several tens of nm) and monoenergetic heavy ion beams could be obtained [4], [5], [6]. There, ions can theoretically gain very high energy (much more than discussed in Ref. [84] and given by Eq. (2.70)) due to the ballistic

evolution - the foil is gradually accelerated as a compact block. Nevertheless, this approach has constraints due to multidimensional effects leading to undesirable electron heating and target explosion. Two-dimensional PIC simulations have demonstrated that it is still possible to accelerate the central part of the foil by using specially tailored laser beam (super-gaussian shape with a plateau in the central part) with a limited pulse duration [6]. More detailed discussion about this acceleration mechanism is out of the scope of this thesis, since the main acceleration mechanism in the range of current experiments is the TNSA.

2.5.2 Target normal sheath acceleration mechanism

Introduction

MeV-electrons that have been generated in the laser focus propagate through the target as discussed above. After the fastest electrons have left the target at the rear side, a strong electrostatic potential is built up due to the charge separation in the vicinity of the rear-side target-vacuum boundary. As soon as the subsequently arriving electrons pass this boundary, they are held back and forced to return into the target. Due to this mechanism, an electron sheath is formed at the rear surface of the target. The initial electrostatic field strength, comparable with the electric field of laser wave, is by far strong enough to ionize atoms at the target rear surface. These ions can be subsequently accelerated by the same fields. Due to hydrocarbon or water contaminants on the surfaces of non-treated targets, the favorably accelerated ion species are protons, as they have the highest charge-to-mass ratio. The heavy ions can be also efficiently accelerated from cleaned targets. In last years, such cleaning techniques like target heating and laser ablation have developed, permitting to remove almost all protons and other contaminants from the target [87].

The accelerated ions leave the target together with comoving electrons forming a quasi-neutral plasma cloud. As the plasma density in this cloud quickly drops after the detachment from the target and as the temperature remains high in this cloud, recombination effects are negligible for propagation lengths in the range of several meters [88]. The accelerating electrostatic field is parallel to the normal vector of the target rear surface, therefore the mechanism is called target normal sheath acceleration (TNSA). The scheme of the TNSA mechanism is sketched in Fig. 2.4.

The mechanism has been firstly described by Snavely and Wilks [8], [10] in short-pulse experiments using the NOVA-Petawatt laser at the Lawrence Livermore National Laboratory, where the emission of protons normal to both rear surfaces of a wedge-shaped target was observed. Since then it has been widely accepted as a possible mechanism to accelerate ions to high kinetic energies (in tens of MeVs per nucleon with presently achievable laser intensities).

Basic theoretical model

The basic broadly used theory for this mechanism has been developed in Ref. [66]. Here, the ion expansion is described by the model of free isothermal expansion into a vacuum of a plasma occupying initially a half space $x < 0$. We recall the basic set of equations (2.46), (2.47) which leads, together with the assumption of Boltzmann equilibrium (2.9), to the self-similar solution (2.48) describing the rarefaction wave. This solution is valid on the

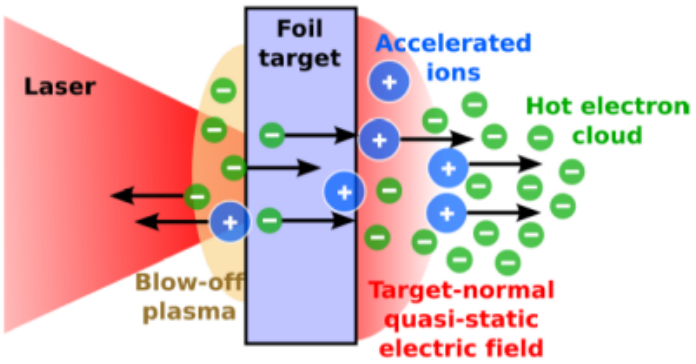

Figure 2.4: Scheme of the TNSA mechanism: Electrons heated at front side pass through a thin target, escape to vacuum and form an electrostatic field which accelerates ions.

scale length larger than the Debye radius. By integration of the Poisson equation (2.46) from $x = 0$ to $x = \infty$, the maximum accelerating electric field can be obtained

$$E_{ac} = \sqrt{\frac{2}{e_N}}\frac{T_e}{e\lambda_{D0}} \approx \frac{T_e}{e\lambda_{D0}} = \sqrt{\frac{n_{e0}T_e}{\epsilon_0}} \tag{2.71}$$

where T_e is the electron temperature, λ_{D0} is the Debye length in the unperturbed plasma of electron density n_{e0}, and and $e_N = 2.7182...$ is Euler number. The analysis of the system (2.46), (2.47) also shows that the self-similar solution terminates with the shock front where the ion velocity achieves its maximum. The maximum velocity can be translated into the maximum (cutoff) energy of accelerated ions

$$\varepsilon_{imax} \simeq 2ZT_e \ln^2(\tau + \sqrt{\tau^2 + 1}). \tag{2.72}$$

The self-similar model also predicts a number of ions per unit energy and unit surface (ion energy spectrum)

$$\frac{dN}{d\varepsilon_i} = \frac{n_{i0}c_s t_{acc}}{\sqrt{2\varepsilon_i ZT_e}} \exp\left(-\sqrt{\frac{2\varepsilon_i}{ZT_e}},\right) \tag{2.73}$$

where $c_s = \sqrt{ZT_e/m_i}$ is the ion acoustic velocity, $\tau = \omega_{pi}t_{acc}/\sqrt{2e_N}$, $\omega_{pi} = \sqrt{n_{i0}Z^2e^2/(m_i\epsilon_0)}$ is the ion plasma frequency, t_{acc} is the ion acceleration time, and Z is the ion charge number. By integration the product of (2.73) with ε_i, one can obtain the total energy of accelerated ions

$$W_{itot} = \int \varepsilon_i \frac{dN}{d\varepsilon_i} d\varepsilon_i = ZT_e n_{i0} c_s t_{acc} \tag{2.74}$$

The laser-to-ion conversion efficiency is defined as the ratio of W_{itot} and the laser pulse energy ε_{Ltot}

$$\eta_i = W_{itot}/\varepsilon_{Ltot}. \tag{2.75}$$

Previously described analytical isothermal model is usually applied to explain experimental and numerical results on ion acceleration, although there are several issues:

- *Ion acceleration time and constant electron temperature*
  Firstly, the maximum energy in Eq. (2.72) diverges logarithmically with time, while the total energy in the fast ions (2.74) diverges linearly, so that to be able to apply the model to the interpretation of experiments, one has to determine the relevant time t_{acc} at which the acceleration is stopped. A natural choice for t_{acc} is the laser pulse duration t_L, but one might argue that, in the experiment, the acceleration does not stop suddenly, and that it goes on even for $t > t_L$. On the other hand, the isothermal model assumes a constant electron temperature, which can be a reasonable assumption during the laser pulse, but is certainly violated for late times, as the electrons progressively give their energy to the ions and cool down in the expansion.

  An alternative adiabatic model [89] investigates the collisionless expansion into a vacuum of the thin foil instead of semi-infinite plasma slab and assumes that the electron temperature is a function of time determined by the energy conservation equation

  $$\frac{dU_e}{dt} = -\frac{dU_i}{dt} - \frac{dU_{field}}{dt} \tag{2.76}$$

  where U_i is the kinetic energy of ions, U_{field} is the electrostatic energy of the electric field, and U_e is the thermal energy of electrons. This approach provides a rather good approximation when the laser pulse turns off. It is clear that the total ion energy does not diverge in this case. However, this model does not give an exact analytical solution and has to be treated numerically.

  Another theoretical approach is presented in Ref. [90]. The basic idea is that only those electrons, which are bound in the overall positive potential created by the lattice ions and by themselves, participate to the formation of the quasi-stationary electron cloud, while the most energetic electrons overcome the potential barrier and are lost by the system. The correct inclusion of bound electrons only in the Poisson equation removes the above mentioned problems (energy divergence, determination of acceleration time) as the accelerating electrostatic field becomes zero at a finite distance from the initial plasma-vacuum boundary.

- *Two populations of electrons*
  The second issue of the model [66] is the assumption of a single electron temperature, which is not appropriate for laser plasma interactions. During the interaction, two populations of electrons should be considered - the background cold electrons and the minority of hot electrons. Then, the electron density is a sum of two Boltzmann distributions with cold (T_c) and hot (T_h) temperatures (2.49). In the relativistic case, T_h/T_c is certainly well above the critical value ≈ 10, for which the quasineutral fluid theory of the expansion of semi-infinite plasma predicts two corresponding ion populations - while the first expands slowly according to the cold electron temperature, the second expands according to the hot electron temperature [91]. There is at all times a point in space where the slower ions cannot follow the faster ones and the two populations separate. At the position where this separation occurs, a strong space-charge field is generated and the ion density, as well as the velocity, experience a jump which can be identified as rarefaction shock [67]. Thus, there is also formed a dip in the ion velocity spectrum. To make it more clear, the results of numerical simulations are presented

in Fig. 2.5. The numerical solution was found from the Boltzmann-Vlasov-Poisson model (BVP) [92], where the electrons follow the Boltzmann distribution and the ions are described by the Vlasov kinetic equation in one spatial dimension completed with the Poisson equation for the electrostatic potential.

Since the fast ion expansion is mainly determined by the hot electron component, the fast ion velocity (energy) spectrum is almost identical to what it was in the one-temperature case (2.73). In the equations from (2.71) to (2.74), one need to change the electron density $n_e = Zn_i$ to hot electron density n_h, the electron temperature T_e to hot electron temperature T_h, and the ion plasma frequency to a partial ion plasma frequency $\omega_{pih} = \sqrt{n_{h0}Ze^2/(m_i\epsilon_0)}$.

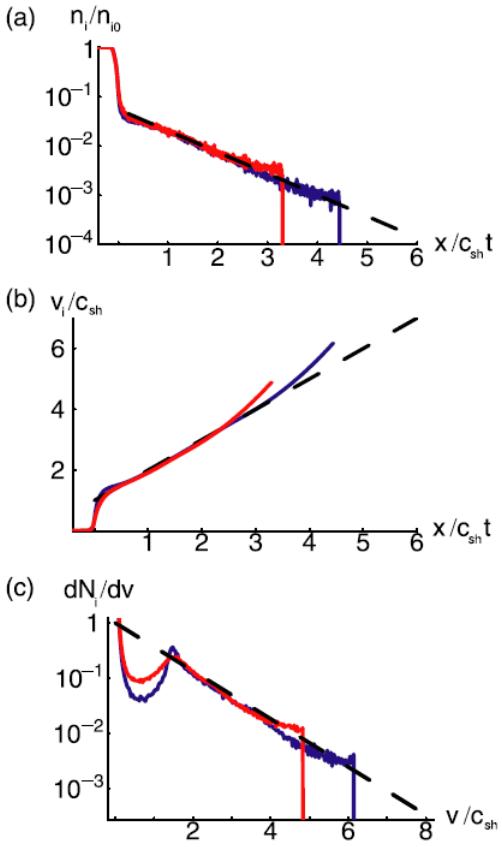

Figure 2.5: Rarefaction wave in the self-similar coordinates for two-temperature electron distribution with T_c=4 keV, $n_{c0} = 10^{23}$ cm^{-3} and T_h=4 MeV, $n_{h0} = 10^{21}$ cm^{-3}, and for one ion species (protons). (a) ion density, (b) average ion velocity, and (c) ion velocity distribution normalized by $n_{i0}t$. Solid lines represent the numerical solution from the BVP model [92] for the time $\omega_{pih}t = 10$ (red) and 20 (blue), dashed lines represent the self-similar solution [67].

- *2D and 3D effects*
  The third problem of the isothermal model [66] (as well as the problem of the adiabatic model [89]) is that they do not include multidimensional effects. The one-dimensional

model assumes, in fact, a planar intense laser wave interacting with plasma which creates a population of homogeneously distributed hot electrons inside the initial plasma. However, the laser pulse is tightly focused under realistic experimental conditions and the hot electron sheath spreads along the target surface, which certainly decreases the efficiency of the acceleration process. This problem is also one of the main subject of the thesis - the confinement of hot electrons reduces their spread and enhances the efficiency of the ion acceleration, which is subsequently closer to overestimated predictions of one-dimensional models.

One of important parameters of accelerated laser beams, which has not been mentioned yet and cannot be predicted by one-dimensional models, is the beam divergence. The ions are accelerated parallel to the normal vector of the target rear surface. If the multidimensional effects are taken into account, the initial planar rear surface is curved due to the gradual spread of the sheath layer [8], [93]. As the accelerating electric field decreases due to the expansion and the sheath spread, it is expected that the most energetic ions are accelerated from the planar rear surface and the ions with a lower energy could be also accelerated from subsequently curved surface. Thus, the divergence of the fastest ions should be lower than the divergence of ions with a lower velocity.

Experimental results

Experiments with thin foils (the thickness is of the order of 10 μm) have shown the proton energy scaling for ultrashort pulses ranging from 8.5×10^{17} Wcm^{-2} to 6×10^{20} Wcm^{-2} (intensity) and from 55 fs to 8 ps (duration) [16], [17], [18]. One-dimensional model of isothermal expansion [66] provides a good fit to the maximum proton energies for intensities up to several times 10^{19} Wcm^{-2}, but for higher intensities a more realistic temperature-varying model is required. Also, the multidimensional effects become more important [18] with increasing intensity because the longitudinal excursion of the fast ions at the back of the foil becomes of the order of the transverse plasma size in a shorter time.

The qualitative theoretical prediction on ion beam divergence (discussed above) has been confirmed by numerous experiments. They are, for example, summarized in Ref. [94], where the beam divergence of the fastest ions is about 15° and the divergence of the ions with the energy about 1/5 of the maximum energy is more than 30°.

The TNSA mechanism works as well at the target front surface, as the MeV-electrons that were initially accelerated in laser direction, are reflected at both target surfaces due to the space charge fields, which is called hot electron recirculation, see Ref. [3], [39]. Due to the longer scale length in the front side blow-off plasma, that has been generated by the laser prepulse, the electric fields are lower here. Although the potential difference is equal for both target surfaces, the electric fields, that are proportional to the potential gradient, are inversely proportional to the Debye length in the plasma sheaths at each target surface. As the potential difference and the electric fields are only kept up as long as the electron temperature remains high, ions accelerated at the target front side gain lower energies by the TNSA mechanism. On the other hand, recent techniques [63], [64] enable to avoid preplasma formation and lead to the same or even slightly higher maximum energies of ions emitted from the foil front side [41].

2.5.3 Multiple ion species

The one-dimensional model of two ion species acceleration in isothermal plasma [67] describes the spatial separation of ion species in expanding plasma which leads to the discontinuity formation. This model considers a mixture of heavy ions with charge Z_1, mass $m_1 = A_1 m_p$ (m_p is the proton mass) and density n_1, and light ions with charge Z_2, mass $m_2 = A_2 m_p$ and density n_2. The charge-to-mass ratio $\alpha = A_1 Z_2/(A_2 Z_1)$ is large and the heavy ions dominate, $N = Z_1 n_{10}/(Z_2 n_{20}) >> 1$. The electrons are isothermal and follow the Boltzmann distribution similar to (2.49) with $n_{e0} = Z_1 n_{10} + Z_2 n_{20}$.

In the dense plasma region, where the heavy ions dominate, the velocity of the rarefaction front depends on the ratio between the densities and the masses of ions. The effect of light ions can be neglected, if $N > \alpha$. Then, the movement of heavy ions is described by the self-similar equations (2.48) where c_s is substituted by the heavy ion acoustic velocity $c_{s1} = \sqrt{Z_1 T_e/(A_1 m_p)}$

$$Z n_1 = n_{e0} \exp\left(-x/(c_{s1}t) - 1\right), \qquad v_1 = c_{s1} + x/t, \qquad e\varphi = -T_e(x/(c_{s1}t) + 1). \quad (2.77)$$

The solution (2.77) defines the speed of the upstream front of the heavy ion rarefaction wave, $x_{01}/t = -c_{s1}$.

Behind the heavy ion upstream front, $x > x_{01}$, the light ions behave as test particles. They move in the given potential φ (2.77) created by the dominant, heavy ion population. The electric field associated with this potential is $\sqrt{\alpha}$ times stronger than the field that would be created by the light ions themselves. The light ions then get a boost. For light ions in the limit $\alpha >> 1$ one finds

$$v_2 \approx c_{s2}\sqrt{2(1 + x/(c_{s1}t))}, \qquad n_2 \approx n_{20}/\sqrt{1 + 2\alpha(1 + x/(c_{s1}t))} \quad (2.78)$$

where $c_{s2} = \sqrt{Z_2 T_e/(A_2 m_p)}$ is the light ion acoustic velocity.

The density of light ions decreases very slowly in space. Correspondingly, very shortly at the distance x_{k1} where the heavy ions achieve their maximum velocity $v_{1k} = x_{k1}/t$, the densities of both species equalize and then the light ions dominate the expansion.

$$x_{k1} \approx c_{s1} t[\ln(4N\sqrt{2\alpha}) - 2] \quad (2.79)$$

For $x >> x_{k1}$, there will be no heavy ions, and we return to the single ion specie expansion, discussed in the previous section.

The analysis shows that in the transient region $x \gtrapprox x_{k1}$, the light ion density and velocity are constants given by (2.78). The light ion energy spectrum comprises three parts: the slow particles with $\varepsilon_{i1} < \varepsilon_{kp}$, the delta-function-like peak with $\varepsilon_{i1} \approx \varepsilon_{kp}$, and the tail $\varepsilon_{kp} < \varepsilon_{i1} < \varepsilon_{imax}$. Here, the maximum light ion energy is determined by Eq. (2.72) and the position of discontinuity point in energy spectra of light ions

$$\varepsilon_{kp} \approx Z_2 T_e \ln(4N\sqrt{2\alpha} - 1) \quad (2.80)$$

does not depend on time (after the moment when the discontinuity is created), but only on the electron temperature and the partial concentration of light ions.

To demonstrate previously discussed analysis, Fig. 2.6 shows the results of numerical simulation of BVP model [92] (also described briefly in the previous section) with single

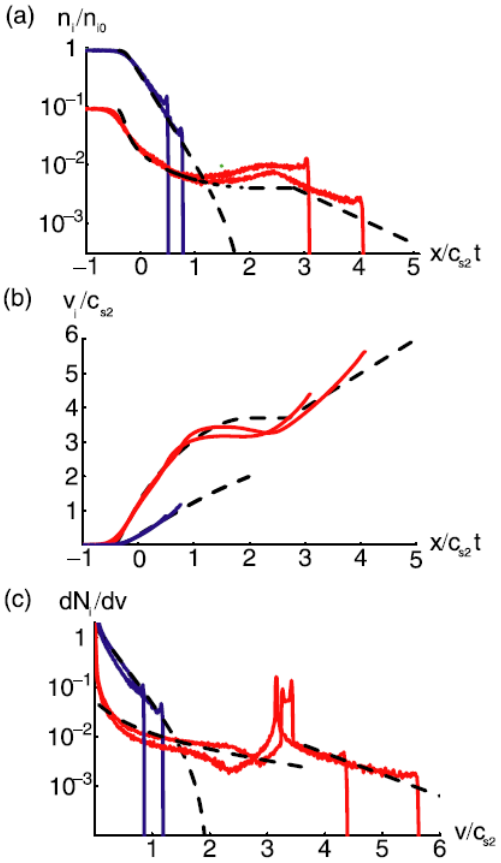

Figure 2.6: Rarefaction wave in the self-similar coordinates for two ion species (CH plasma) in isothermal plasma: (a) ion densities, (b) velocities, and (c) distribution functions. Full lines represent the numerical solution from the BVP model [92] for the time $\omega_{pi2}t = 20$ and 40 for the light (red) and heavy ions (blue). Dashed lines represent the self-similar solution of hydrodynamic equations in the quasi-neutral limit for $\alpha = 12$ and $N = 10$ [67].

electron population and two ion species. The simulation consider a CH plasma with $\alpha = A_1Z_2/(A_2Z_1) = 12$ (singly ionized carbon and protons) and $N = Z_1n_{10}/(Z_2n_{20}) = 10$.

The prediction of this model opens possibilities for control of the number and the energy spectrum of accelerated ions. We should note that there exists also another possibility of modulation in ion energy spectra due to acceleration of them by thermal (cold) and hot electrons with the ratio of temperatures above ≈ 10 as discussed in the previous section (see the discussion of the problem of a single electron temperature in the Mora's isothermal model). However, numerical simulations [67], [91] have shown that this separation of ions due to different electron temperatures fails under more realistic conditions of temperature variation even in one-dimensional case.

The effect of shaping in light ion energy spectra requires almost uniform dense hot electron sheath, which cannot be satisfied in the experiments with non-treated foils. Here, the energy spectrum of ions accelerated by widely used TNSA mechanism is usually broad, exponential (2.73) with the cutoff energy (2.72). A special treatment with foils, such as the foil coated with hydrogen rich dots [14] and carbon catalytic layer [15] can lead to quasimo-

noenergetic ion beams. It was shown by numerical simulations that a pure proton microdot target does not by itself result in a quasimonoenergetic ion beam and, thus, multispecies ion composition has to be taken into account [43]. Nevertheless, these experiments are difficult to realize as a sophisticated target engineering is required. Other possibility is to use mass-limited targets with sizes comparable with the laser spot size. Dips and peaks in the ion energy spectra were observed in the experiments with water (and heavy water) droplets of a diameter approximately two times larger than the laser spot size [21], [22].

The formation of dips and peaks in proton energy spectra was also mentioned as the result of the interaction of two subsequent short high intensity laser pulses with a target, however, this scheme proposed in Ref. [95] has no experimental evidence to date. For the following monochromatisation and collimation of a laser accelerated protons in a certain energy range, Ref. [96] demonstrates the employment of a permanent quadrupole magnet lens system.

2.5.4 Enhancement of ion energy due to reduced target thickness

A higher efficiency of TNSA mechanism is strongly desired for various applications using the accelerated ion beams. One possibility is to reduce target thickness. Here, we will discuss theoretical model together with experiments as it is more illustrative in this case.

Experiment with Al foils of variable thickness ranging from 3 μm to 100 μm [39] demonstrated an increase of maximum proton energy from 6.5 MeV to 24 MeV with the reduction of the thickness, see Fig. 2.7 (left panel). Moreover, the paper shows 2D PIC simulation results in agreement with experimental ones. The experiment was performed using a Ti:sapphire laser at a wavelength of 800 nm and duration of 100 fs. The p-polarized pulse was focused at incidence angle of 22° onto the target with a focal spot size of 4 μm. The peak laser intensity was in excess of 10^{20} Wcm^{-2}.

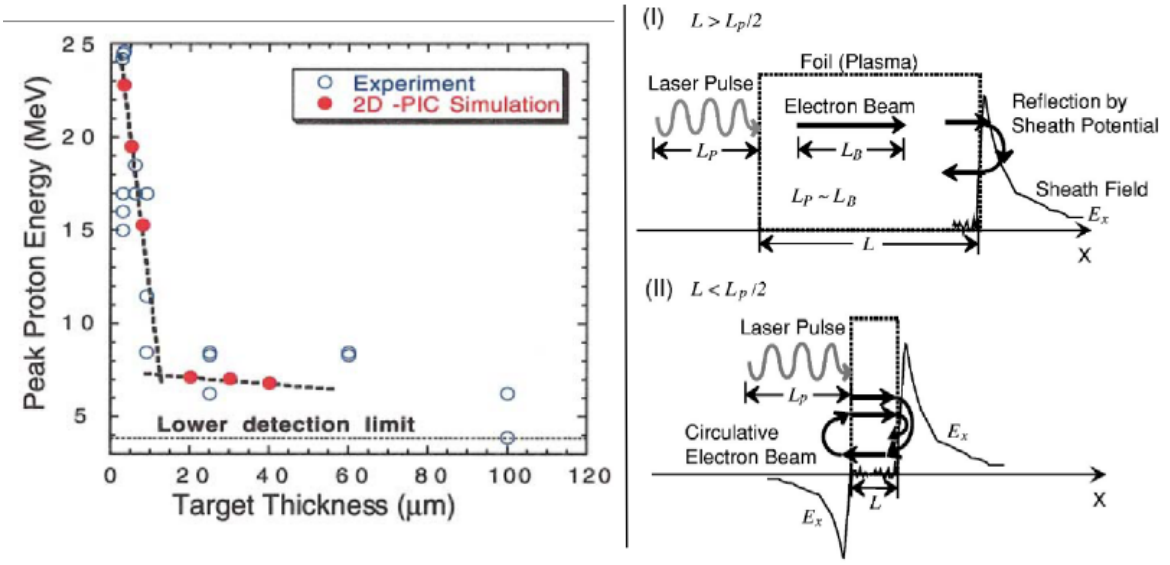

Figure 2.7: left panel - Maximum proton energy vs. target thickness for experiment and 2D PIC code simulations [39]; right panel - Images of the electron circulation inside the target for (I) a thick foil and (II) a thin foil [3].

In Fig. 2.7 (left panel), there are two distinct slopes present in both the simulation results and experimental data. For a thickness less than 15 μm the maximum proton energy falls in a steep quasilinear trend with increasing target thickness, while for a greater thickness the slope becomes much flatter. These two distinct regions can be explained by the temporal dynamics of high energy electrons as they propagate through the target. According to (2.72), the maximum proton energy is directly proportional to the product of hot electron temperature T_h with the natural logarithm of hot electron density $\ln(n_h)$. As the laser pulse intensity is the same in the experiment, T_h should not vary and the explanation is in different n_h.

The range of foil thickness from 15 μm to 100 μm corresponds to the situation sketched schematically at the top (I) of right panel in Fig. 2.7. In this case, the spatial length of laser pulse, ct_L, is smaller or comparable with the target thickness, d. A relatively small decrease of maximum proton energy with increasing foil thickness is explained by the divergence of hot electrons. According to the model [97] of TNSA mechanism, N_h electrons are accelerated over the laser pulse duration t_L and spread over the surface of the sheath S_{sh} at the rear target side, the density $n_{h0} = N_h/(ct_L S_{sh})$ with $S_{sh} = \pi(r_0 + d \times \tan\theta)^2$. The latter depends on the half-angle divergence of hot electrons inside the target ($\sim 20^\circ$), the target thickness d and the initial radius r_0 of the zone over which the electrons are accelerated at the target front surface, that is, the laser spot.

For the foil thickness less than 15 μm, $d < ct_L/2$, the hot electron density in the sheath layer is strongly enhanced due to the recirculation of hot electrons. That corresponds to the bottom (II) of right panel in Fig. 2.7. In this case, the accelerated electrons propagating through the target are reflected by the sheath field at the foil back, then at the foil front and so on. They are mixed with newly accelerated electrons, that means an increase of hot electron density at the sheath. Moreover, the density is further increased by the effect of lower hot electron spread (due to their divergence) with thinner target as discussed above for thicker targets.

In other experiment in Ref. [17], there is also shown the dependence of laser-to-proton conversion efficiency on the foil thickness. In the 1D isothermal model of ion acceleration, the conversion efficiency (the integral of (2.73)) is directly proportional to the product $T_h n_h$. Thus, the conversion efficiency should increase more rapidly with decreasing foil thickness. Indeed, it differs more than one order of magnitude comparing experimental data of 20μm and 80μm thick foils.

In recent experiments, the laser pulse contrast has been increased by several orders of magnitude by using a plasma mirror [63] or a double plasma mirror [64], which enables to decrease further the foil thickness. Ultra-high laser pulse contrast inhibits preplasma formation on the target front. The presence of preplasma may slightly increase laser pulse absorption and, thus, the maximum energy of ions (cutoff energy) [27], [98]. On the contrary, a prepulse-launched shock wave reduces the electrostatic fields due to an initial ion density scale length at the rear side of a thin target, which leads to the resulting reduction of ion cutoff energy or even destruction of the ion acceleration process [99], [100]. The employment of the plasma mirror enables to accelerate ions from ultrathin foils (their thickness is from 10's to 100's nm) and produce more energetic ions as the ion cutoff energy decreases with the target thickness [40], [41]. The optimal foil thickness found in those experiments is about 100 nm. The paper [41] also points out that 1D PIC simulations overestimate the maximum proton energy due to missing transverse divergence effects of electrons spreading

through the target.

2.5.5 Conclusion

Since the mass of ions (thus, their inertia) is much higher than the mass of electrons, presently achievable laser intensities are not sufficient enough to accelerate ions directly within one laser wave period. However, hot electrons can mediate the forces of the laser field and generate strong electrostatic fields of the same magnitude as the fast oscillating laser fields. These relatively long-lasting electric fields subsequently accelerate ions.

Two basic acceleration scenarios are described in this section. The first one is explained by the space-charge separation on the target front due to the action of ponderomotive force. The ponderomotive force pushes electrons into the target, creates the electron depletion layer on the target surface followed by the compressed electron cloud in the target interior. Then, the resulting electric field due to the charge separation sustained by the laser radiation pressure attracts ions and accelerates them.

The main attention is concentrated on the second scenario - the target normal sheath acceleration. In this case, hot electrons cross the target and propagate behind its rear side where a strong electrostatic potential is built and ions are accelerated in the direction normal to the target rear surface. This mechanism can also work on the target front, especially when the level of laser prepulse is strongly reduced, as the electrons can recirculate forth and back. The acceleration of ions is usually described by the model of free isothermal expansion of plasma into a vacuum which provides reasonable approximation in most cases. This model predicts that the maximum ion energy is proportional to the hot electron temperature whereas the laser-to-ion energy conversion efficiency is rather proportional to the hot electron temperature multiplied by the hot electron density. Multidimensional effects which are not taken into account in the discussed one-dimensional model certainly reduce the efficiency of acceleration process - experiments on maximum proton energy scaling have demonstrated that the 1D model works quite well for laser intensities up to several times $10^{19}\ \mathrm{W/cm^2}$, but for higher intensities a more realistic temperature-varying model is required.

Energy spectrum of accelerated ions is usually broad, exponentially decreasing with the cutoff (maximum) energy. However, this spectrum can be modified by the presence of other ion species (which is, in reality, satisfied in the surface contamination layers) and by considering an uniform dense hot electron sheath (that is not satisfied in a typical experiment with foils). It is expected to work for specially treated structured foils or for targets with all sizes less or comparable with the laser spot size).

The last part of this section is devoted to the experimental demonstration and theoretical explanation of ion energy enhancement due to a reduced target thickness. We are interested in this problem as it is one of possibilities to enhance the ion acceleration efficiency, previously described and demonstrated. The enhancement can be explained by the recirculation of hot electrons forth and back (in the longitudinal direction) and by reduced hot electron beam spread for thin foils, which both increase the hot electron density in the sheath. The second possibility, the enhancement of the acceleration efficiency in foil sections of reduced surface due to the refluxing of hot electrons in the transverse direction, is experimentally demonstrated and theoretically explained in detail in Chapter 4.

2.6 Ion acceleration in clusters

Sub-wavelength clusters provide another possibility for efficient ion acceleration. The qualitative picture of ion acceleration in such clusters depends on the strength of the laser field and the cluster radius. Theoretical analysis of this phenomenon can be made with the use of the relevant simplifying assumptions that clusters are much smaller than the laser wavelength and that the electron plasma frequency inside the cluster is considerably greater than the laser frequency (thus, overdense plasma).

2.6.1 Coulomb explosion in small clusters

We start by considering a uniform spherical cluster, with ion density n_{i0}, in a uniform static electric field E_0. The field extracts electrons from the cluster, making the cluster positively charged. If all the electrons are extracted, the cluster becomes a uniform ion sphere with the total charge $N_i Ze$, where $N_i = (4/3)\pi R_0^3 n_{i0}$ is the total number of ions in the cluster and R_0 is cluster radius. In this case, the electric field created by the cluster increases from zero at the center to

$$E_{max} = \frac{N_i Ze}{4\pi\epsilon_0}\frac{1}{R_0^2} = \frac{n_{i0}R_0 Ze}{3\epsilon_0} \tag{2.81}$$

at the cluster edge and then decreases radially outside the cluster.

The external field can extract all the electrons only if $E_0 > E_{max}$. In this regime, electrons do not affect the dynamics of the ion explosion. The ions are accelerated in the electrostatic field of their own charge, they are receiving the kinetic energy according to their initial position in the cluster, from 0 up to the maximum energy. One can obtain the following relations by considering the transfer of initial potential electrostatic field energy into the kinetic energy of particles.

The ion energy distribution function obtained from the simple cluster explosion is proportional to the square root of energy [101]

$$\frac{dN}{d\varepsilon_i} = \frac{3}{2}\frac{N_i}{\varepsilon_{imax}}\sqrt{\frac{\varepsilon_i}{\varepsilon_{imax}}}, \tag{2.82}$$

with the maximum (cutoff) energy equal to

$$\varepsilon_{imax} = \frac{5Z^2e^2}{8\pi\epsilon_0}\frac{1}{R_0}. \tag{2.83}$$

The explosion time of small cluster ($\tau_i \approx 1/\omega_{pi}$) [102] is typically much longer than the laser period $\tau_i\omega >> 1$.

This feature of increasing ion number with energy, i.e., of a relatively high average ion energy produced in clusters, attracts the attention due to the possibility of quite efficient neutron production. The latter was demonstrated by numerous experiments, for example with deuterium [103] or deuterated methane [104], [105] clusters. A typical diameter of those clusters produced in gas jets is several nm, the maximum energy of accelerated ions in the experiments is about 10 keV. The laser pulse intensity used in those experiments is around 10^{17} Wcm^{-2} and the pulse duration $\sim$ 40 fs.

2.6.2 Ion dynamics in larger clusters

In small clusters with diameters of a few tens of nanometers, which is of the order of the hot electron Debye length, the Coulomb ion repulsion is the dominant mechanism. In this case, energies of MeV per nucleon were never observed as their size is considerably limited by the laser field strength. In addition, small clusters are much more sensitive to the laser prepulse and can be easily destroyed before the peak of the laser pulse. Larger clusters with diameters in the 100 nm range are expanding under the pressure of hot electrons, which cannot leave the droplet because of its very high electric charge. Moreover, the ionization is very inhomogenous - atoms in the outer layer of a thickness about the skin depth (~ 10 nm) are ionized by the laser electric field to a high degree, while atoms in the inner part of the target can be ionized only by electron collisions, which are very rare for high intensity lases pulses. Therefore, it appears that the size of clusters and a high laser pulse contrast are the crucial parameters for efficient ion acceleration.

Authors of Ref. [106] solve the problem of self-similar expansion of finite-size non-quasi-neutral plasmas into vacuum, which is the case of homogeneous larger cluster. The problem is solved in the planar, cylindrical and spherical geometries ($\nu = 1, 2, 3$) by the set of one-dimensional hydrodynamic equations for electron, ion densities (continuity equations) and momentum, Poisson equation, and, instead of the energy equation, a polytropic law is used for the electron temperature evolution $T_e(t)/T_{e0} = [n_e(t,0)/n_e(0,0)]^{\gamma-1}$, where $\gamma = 4/3$ (the adiabatic case of ideal electron gas). Here, important parameters are the ratio of cluster radius R_0 and Debye length which is kept constant during the expansion

$$\Lambda_s = \frac{R_0}{\lambda_{D0}} = \frac{R(t)}{\lambda_D(t)} \tag{2.84}$$

We also need to take into account the small but crucial factor $\mu_e = Zm_e/m_i << 1$ (electron-to-ion mass-over-charge ratio) as the familiar Boltzmann relation (2.9) cannot be applied for spherical geometry ($\nu = 3$).

The most important output of the self-similar solution is the maximum ion energy ε_{imax} for ions at the vacuum boundary in the form

$$\varepsilon_{imax} = \varepsilon_0 \xi_f^2, \qquad \varepsilon_0 = 2ZT_{e0}/(\nu(\gamma - 1)) \tag{2.85}$$

where ε_0 is the characteristic energy for ion at infinite time given for the case of instantaneous heating $\gamma > 1$ ($t_L << R_0/c_{s0}$, where t_L is the laser pulse length and c_{s0} ion-acoustic velocity). In spherical geometry ($\nu = 3$), the asymptotic behavior of ξ_f with respect to Λ_s is analytically derived in the limits $\Lambda_s << \mu_e^{-1/2}$ and $\Lambda_s >> \mu_e^{-1/2}$ as follows

$$\xi_f^2 = \begin{cases} \xi_{fA}^2 = W[\pi^{1/3}\Lambda_s^{4/3}/(2\mu_e)]/2, & \Lambda_s << \mu_e^{-1}, \\ \xi_{fB}^2 = W[\Lambda_s^2/2], & \Lambda_s >> \mu_e^{-1}, \end{cases} \tag{2.86}$$

where $W(x)$ is called the Lambert function defined as the inverse of the function

$$x(W) = W \exp(W) \tag{2.87}$$

Asymptotically, $W(x) \approx x$ for $x << 1$ and $W(x) \approx \ln(x/\ln x)$ for $x >> 1$. An approximate value of ξ_f for arbitrary Λ_s is

$$\xi_f \approx (\xi_{fA}^6 + \xi_{fB}^6)^{1/6}, \quad 0 < \Lambda_s < \infty \tag{2.88}$$

The second important output of the self-similar solution is the energy spectrum of ions

$$\frac{dN}{d\varepsilon_i} = \frac{n_{i0}}{\varepsilon_0}\left(\frac{\varepsilon_i}{\varepsilon_0}\right)^{\nu/2-1}\left[\exp\left(-\frac{\varepsilon_i}{\varepsilon_0}\right)+\frac{2\nu}{\Lambda_s^2}\right], \quad \varepsilon_i \leq \varepsilon_{imax}. \tag{2.89}$$

In the limit of $\Lambda_s \to 0$, $dN/d\varepsilon_i \propto \sqrt{\varepsilon_i/\varepsilon_0}$ is the Coulomb explosion spectrum, whereas for $\Lambda_s \to \infty$, $dN/d\varepsilon_i \propto \sqrt{\varepsilon_i/\varepsilon_0}\exp\left(-\varepsilon_i/\varepsilon_0\right)$ is the ambipolar expansion type of spectra.

In reality, the larger clusters are usually composed of several ion species which makes the situation more complicate as the energy spectra of ions are the combination of Coulomb-like and ambipolar-like expansion of spectra. In this case, there is a solution for a particular case of homogeneously distributed impurity ions [107]. This solution accompanied by numerical simulations demonstrates that the formation of a monoenergetic light ion bunch at the maximum energy of the spectra (2.89) takes place when the factor expressing the Coulomb-like explosion is larger than the factor expressing ambipolar-like explosion, that is, for $\Lambda_s \lesssim 5$. Thus, in multispecies medium-sized clusters, the light ions are running ahead of heavier ions and, additionally, in the spectra described by (2.89), the high energy peak is formed.

2.6.3 Conclusion

Clusters are usually spherical targets with a diameter much lower than the the laser wavelength. In this case, a sufficiently intense laser wave can expel a relatively large fraction or even all electrons from the cluster. If all electrons are extracted, the cluster expands only under the action of Coulomb forces. This mechanism of ion acceleration results in the energy distribution function proportional to the square root of ion kinetic energy, in contrast to the TNSA mechanism in thin foils where the number of ions is exponentially decreasing with their velocity. Thus, the Coulomb explosion gives relatively high average ion energy compared to their maximum (cutoff) energy in the energy spectra.

In larger clusters, all electrons cannot leave the target because of very high restoring forces due to their high electric charge. In this case, the ion energy spectrum is composed of two parts which comprise Coulomb-like explosion and ambipolar-like expansion. In multispecies clusters, if the factor expressing Coulomb-like explosion is sufficiently large, i. e. the ratio of the cluster radius and the hot electron Debye length is below ~ 5, a substantial part of light ions forms a monoenergetic light ion bunch at the maximum energy in the spectrum.

It is clear that clusters provide alternative possibility for efficient ion acceleration. Although ion energies obtained experimentally using clusters are far below maximum energies of ions accelerated in solid targets, the advantage of clusters is in a relatively high average energy of accelerated ions. As it is possible now to improve laser pulse contrast by recently developed techniques mentioned above to prevent undesirable cluster heating before the interaction with the main laser pulse, larger clusters could be efficiently used in experiments with relativistically intense laser beams, and thus higher ion energies are expected to be measured. An experiment demonstrating quite efficient proton acceleration (quasimonoenergetic proton bunch about 0.6 MeV) in water spray target together with our theoretical explanation is presented in Chapter 5 of this thesis.

Chapter 3

Particle-in-Cell Simulations

Particle-in-cell codes are usual numerical tools for exploring the physics of interaction of femtosecond laser pulses with ionized targets. Plasma interacting with an ultrashort intense laser pulse is certainly out of the thermal equilibrium, thus the hydrodynamic theory cannot be applied in this case. Kinetic theory solving the Vlasov equation describing the evolution of single-particle distribution function could be used, but its numerical solution is very demanding on computational resources as will be discussed in the next section. Particle approach solving directly the equations of motion of numerical macro-particles is much more suitable in our case.

For our needs, we developed a two-dimensional particle-in-cell (PIC) code several years ago. The development of the new 2D3V PIC code started from older code [108], mainly in the sense that the older code had several unsolved problems at that time (spurious reflection of outgoing electromagnetic waves from simulation box boundaries, complicated setting of obliquely incident laser wave, ...) and we shared experience of its authors during the selection of employed algorithms and the implementation of the new code. Own PIC code gives us a great advantage that the modification of its content is relatively easy due to the knowledge of its all parts. Otherwise, it is usually difficult to read other codes, understand all used algorithms without corresponding references, modify its content or diagnostics, etc.

This chapter is thus devoted to the discussion of general aspects of the PIC method and the description of algorithms used in our code. Note that more detailed description of the code including its testing is presented in Ref. [109].

3.1 Vlasov equation and a PIC code

The kinetic Vlasov equation (2.10) on the single-particle distribution function has to be generally solved in the six-dimensional phase space (three spatial and three momentum coordinates), which is quite complicated. The most straightforward and usual approach is to solve the partial differential equation (2.10) using finite differences on the Eulerian grid in the phase space.

One of the potential advantage of these Vlasov codes is a possibility of producing smooth results. Indeed, the Vlasov codes handle the distribution function, which is a smoothly changing real number already giving a probability of finding the plasma particles at the

corresponding point of the phase space. However, these codes are very expensive from the computational point of view, and even one-dimensional problems may demand the use of parallel supercomputers. The reason, why the Vlasov codes need so much computational power, becomes clear from Fig. 3.1 (a). There is shown an example of two-dimensional phase space (with one spatial and one momentum coordinate). The dashed region represents the part of the phase space occupied by plasma particles, where the associated distribution function $f(x, p_x)$ is essentially non-zero. The unshaded region is empty of particles, and nothing interesting happens there. Nevertheless, one has to maintain these empty regions as parts of the numerical arrays, and process them when solving Eq. (2.10) on the Eulerian grid. This processing of empty regions leads to enormous wasting of computational power. This decisive drawback becomes even more severe with increase in the dimensionality of the problem - the efficiency of Vlasov codes drops exponentially with the number of dimensions and becomes very low in the real six-dimensional case, when one has to maintain in the memory and process a 6D mesh, most of it just empty.

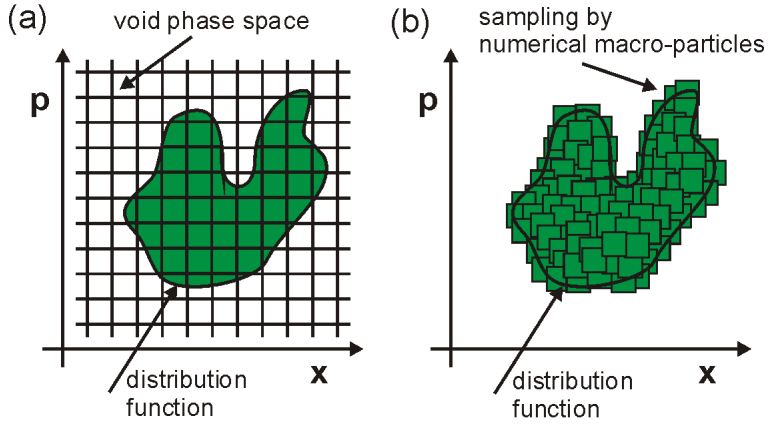

Figure 3.1: (a) Vlasov method: distribution function on Eulerian grid in two-dimensional phase space; (b) PIC method: numerical macro-particles sample the distribution function.

Fortunately, there is more computationally effective method to solve Eq. (2.10) - a special finite-element method. The distribution function can be approximated (sampled) in the phase space by a set of finite phase-fluid elements (FPFE):

$$f_s(\vec{r}, \vec{p}) = \sum_k W_k S(\vec{r} - \vec{r_k}, \vec{p} - \vec{p_k}), \tag{3.1}$$

where W_k is the weight of k-th particle of species s, and $S(\vec{r}, \vec{p})$ is the shape of particle in the phase space, or the support function in the phase space.

Now, let us take a simple example of the support function in two-dimensional phase space:

$$S(x, p_x) = 1 \qquad \text{for} \qquad |x - x_k| < \frac{\Delta x}{2}, \quad |p_x - (p_x)_k| < \frac{\Delta p_x}{2}, \tag{3.2}$$

where Δx is the "width" of a particle along x-axis and Δp_x is the "width" along p_x-axis in two-dimensional phase space. This sampling is also illustrated in Fig. 3.1 (b). Finite elements on the picture are macro-particles of the shape $S(\vec{r} - \vec{r_n}, \vec{p} - \vec{p_n})$ considered in particle-in-cell codes.

Vlasov equation can be substituted by the following set of relativistic equations of motion for macro-particles:

$$\frac{\partial \vec{r_k}}{\partial \vec{t}} = \frac{\vec{p_k}}{\gamma m_k}, \qquad \frac{\partial \vec{p_k}}{\partial \vec{t}} = q_k(\vec{E_k} + \frac{\vec{p_k}}{\gamma m_k} \times \vec{B_k}), \qquad \gamma = \sqrt{1 + \left(\frac{\vec{p_k}}{m_k c}\right)^2} \tag{3.3}$$

$\vec{E_k}$ and $\vec{B_k}$ are electric and magnetic fields at the position of k-th particle, m_k is the rest mass of k-th particle, q_k its charge, γ is the relativistic factor.

The significant advantage of the finite element method over the Vlasov codes is that one does not need to maintain a grid in the full phase space. Instead, finite phase-fluid elements (e.g., macro-particles) sample only the interesting regions, where particles are present, and something important is going on. A grid in the configuration space is still maintained to solve the field (Maxwell) equations, but this grid has only three (and not six as in the Vlasov code) dimensions in the most general case.

3.2 Basic scheme of particle-in-cell codes

There is no essential difference between basic schemes of 1D and 2D or 3D electromagnetic particle codes - the simulation box is divided into cells by a numerical grid where the fields are calculated and each particle has an arbitrary position. The equation of motion is defined by the second Newton law with the Lorentz force

$$\frac{d(\gamma \vec{v})}{dt} = \frac{q}{m}(\vec{E} + \vec{v} \times \vec{B}) \tag{3.4}$$

where $\vec{v} = d\vec{x}/dt$ is particle velocity, $\vec{x}$ its position. Usually, the position is computed in a different time than the velocity according to the leap-frog scheme [110], i.e. positions are calculated always at time moments $t = n\Delta t$ and velocities at time $t = (n + 1/2)\Delta t$ (where n=1,2,3,...). It has been proved that the leap-frog method has a better accuracy than computation of those physical quantities at the same time.

The second step of the PIC code computational cycle are charge and current densities which are computed only at certain places of the simulation box, namely on the grid. This is more complicated, especially in 2D and 3D cases, therefore it will be discussed later (in the section 3.3.2). The following continuity equation (3.5) has to be fulfilled in a finite discrete scheme:

$$\frac{d\rho}{dt} + \nabla \cdot \vec{J} = 0, \tag{3.5}$$

where ρ is charge density and $\vec{J}$ is current density.

In the next step, Maxwell equations are solved to compute values of $\vec{E}$ (electric field) and $\vec{B}$ (magnetic field) on the grid. The last step involves an interpolation method to specify values of $\vec{E}$ and $\vec{B}$ at the position of each particle in the simulation box. Computational cycle of a PIC code is schematically presented in Fig. 6.1.

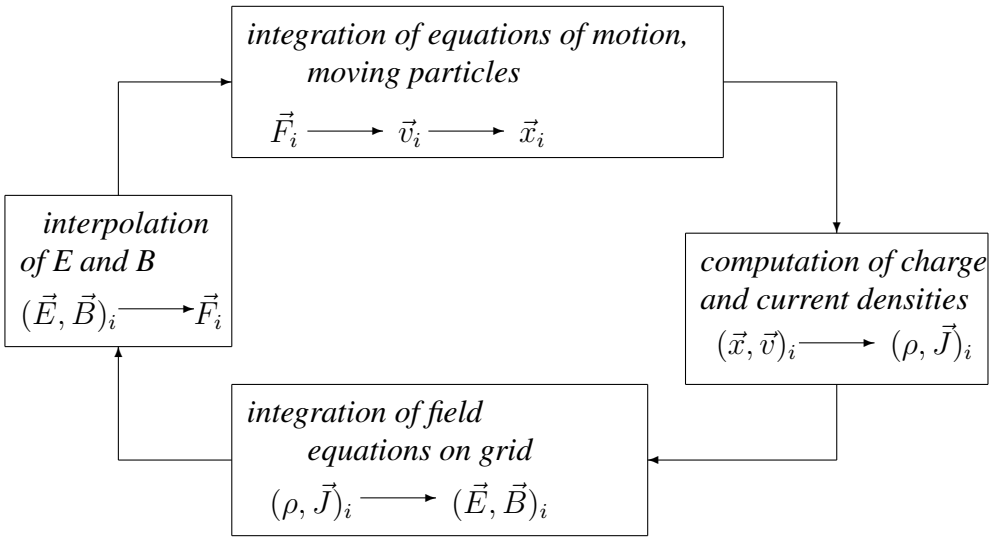

Figure 3.2: Schematics of PIC code computational cycle.

3.3 Algorithms of our two-dimensional PIC code

3.3.1 Maxwell equations

Electromagnetic problems are described by Maxwell equations:

$$\nabla \times \vec{E} = -\frac{\partial \vec{B}}{\partial t}, \tag{3.6}$$

$$\nabla \times \vec{B} = \mu_0 \vec{J} + \frac{1}{c^2}\frac{\partial \vec{E}}{\partial t}, \tag{3.7}$$

$$\nabla \cdot \vec{E} = \frac{\rho}{\epsilon_0}, \tag{3.8}$$

$$\nabla \cdot \vec{B} = 0. \tag{3.9}$$

There are eight first-order differential equations but with only six unknown vector components for three-dimensional cases and four equations with only three unknowns for two-dimensional TE and TM cases. The number of equations is larger than the number of unknowns, thus the system of four Maxwell equations seems to be overdetermined and it is commonly believed that divergence equations (3.8) and (3.9) are redundant. However, ignoring the divergence equations leads to spurious (incorrect) solutions in the computational electromagnetism, see Refs. [111], [112]. Not only curl equations (3.6) and (3.7) have to be solved, but divergence equations (3.8), (3.9) have to be fulfilled too. To ensure it in PIC codes, the first approach is a usage of Poisson equation for a correction of electric fields [110], the second approach uses current densities satisfying the continuity equation (charge conservation schemes) [113], [114], [115].

Solution of Maxwell equations in our 2D PIC code

We will prepare tools to satisfy the charge continuity equation (3.5) without solving of divergence equations (3.8), (3.9) and without any corrections of electric fields in the next section. Now, it is shown, how to solve curl equations (3.6), (3.7) and thus, how to compute electric and magnetic fields on the grid. The points, where x, y and z components of fields and currents are defined, are depicted on figure 3.3

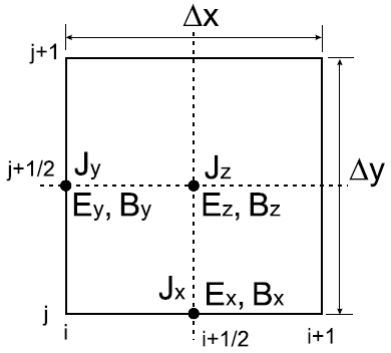

Figure 3.3: Positions of x, y and z components of $\vec{J}$, $\vec{E}$, $\vec{B}$ on the grid.

In **TM case**, there are two components of electric field (E_x and E_y) and one component of magnetic field (B_z). This case is the main subject of our interest, because of the most efficient collisionless absorption of electromagnetic waves in the plasma (p-polarization). The equations can be written as follows

$$\frac{(B_z)^{n+1/2}_{i+1/2,j+1/2} - (B_z)^{n-1/2}_{i+1/2,j+1/2}}{\Delta t} = -\frac{(E_y)^n_{i+1,j+1/2} - (E_y)^n_{i,j+1/2}}{\Delta x} + \\ + \frac{(E_x)^n_{i+1/2,j+1} - (E_x)^n_{i+1/2,j}}{\Delta y}, \tag{3.10}$$

$$\frac{(E_x)^{n+1}_{i+1/2,j} - (E_x)^n_{i+1/2,j}}{\Delta t} = \frac{(B_z)^{n+1/2}_{i+1/2,j+1/2} - (B_z)^{n+1/2}_{i+1/2,j-1/2}}{\Delta y} - 2\pi (J_x)^{n+1/2}_{i+1/2,j}, \tag{3.11}$$

$$\frac{(E_y)^{n+1}_{i,j+1/2} - (E_y)^n_{i,j+1/2}}{\Delta t} = -\frac{(B_z)^{n+1/2}_{i+1/2,j+1/2} - (B_z)^{n+1/2}_{i-1/2,j+1/2}}{\Delta x} - 2\pi (J_y)^{n+1/2}_{i,j+1/2}. \tag{3.12}$$

3.3.2 Charge conservation methods

A local Maxwell solver equivalent to Finite Difference Time Domain Method (FDTD) [116] is considered:

$$\frac{1}{c^2}\frac{\vec{E}^{n+1} - \vec{E}^n}{\Delta t} = \nabla^+ \times \vec{B}^{n+1/2} - \mu_0 \vec{J}^{n+1/2}, \tag{3.13}$$

$$\frac{\vec{B}^{n+1/2} - \vec{B}^{n-1/2}}{\Delta t} = -\nabla^- \times \vec{E}^n, \tag{3.14}$$

$$\nabla^+ \cdot \vec{E}^n = \frac{\rho^n}{\epsilon_0}, \tag{3.15}$$

$$\nabla^- \cdot \vec{B}^{n+1/2} = 0. \tag{3.16}$$

Index n denotes value of a quantity in time $n\Delta t$. Discrete operators ∇^+, ∇^- are vectors

$$\nabla^+ f_{i,j,k} = \left(\frac{f_{i+1,j,k} - f_{i,j,k}}{\Delta x}, \frac{f_{i,j+1,k} - f_{i,j,k}}{\Delta y}, \frac{f_{i,j,k+1} - f_{i,j,k}}{\Delta z} \right), \tag{3.17}$$

$$\nabla^- f_{i,j,k} = \left(\frac{f_{i,j,k} - f_{i-1,j,k}}{\Delta x}, \frac{f_{i,j,k} - f_{i,j-1,k}}{\Delta y}, \frac{f_{i,j,k} - f_{i,j,k-1}}{\Delta z} \right), \tag{3.18}$$

where i, j, k mean grid indices ($x = i\Delta x, y = j\Delta y, z = k\Delta z$).

When the operator $\nabla^+ \cdot$ acts on the equation (3.13) and the operator $\nabla^- \cdot$ acts on the equation (3.14), the following formulas are obtained:

$$\frac{\rho^{n+1} - \rho^n}{\Delta t} + \nabla^+ \cdot \vec{J}^{n+1/2} = 0, \tag{3.19}$$

$$\frac{\nabla^- \cdot \vec{B}^{n+1/2} - \nabla^- \cdot \vec{B}^{n-1/2}}{\Delta t} = 0. \tag{3.20}$$

These relations have been obtained by using the following identities:

$$\nabla^- \cdot \nabla^- \times \vec{f} = \nabla^+ \cdot \nabla^+ \times \vec{f} = \vec{0}. \tag{3.21}$$

The derivation of (3.19) and (3.20) proves that if the charge continuity equation (3.19) is fulfilled, then the divergence of $\vec{E}$ is always equal to the charge density, and, if the initial divergence of $\vec{B}$ is zero then it remains zero. It means that equations (3.8), (3.9) have to be fulfilled at the start of simulations and then, if a conservation algorithm in which current densities satisfy the charge continuity equation at each time step is used, these divergence equations are still valid.

Zigzag scheme

In several charge conservation schemes, particle trajectories over one time step are conventionally assumed to be a straight line, see Villasenor-Buneman method [113] and Esirkepov method [114]. In the zigzag scheme, the particle trajectory is a zigzag line. This scheme has an advantage in computation speed and there is no substantial distortion of physics according to test simulations presented in [115], therefore this method is employed in our PIC code.

The particle is shifted from the position (x_1, y_1) to (x_2, y_2) during a time step Δt.

$$x_1 = x^n, \qquad y_1 = y^n \tag{3.22}$$

$$x_2 = x^{n+1} = x^n + v_x^{n+1/2}\Delta t, \qquad y_2 = y^{n+1} = y^n + v_y^{n+1/2}\Delta t \tag{3.23}$$

Values i_1, i_2, j_1, j_2, which are the largest integer values not greater than $x/\Delta x$ and $y/\Delta y$, respectively, are given by *floor* function.

$$i_1 = \text{floor}\left(\frac{x_1}{\Delta x}\right), \quad i_2 = \text{floor}\left(\frac{x_2}{\Delta x}\right), \quad j_1 = \text{floor}\left(\frac{y_1}{\Delta y}\right), \quad j_2 = \text{floor}\left(\frac{y_2}{\Delta y}\right) \tag{3.24}$$

The particle has no right to move more than the grid spacings Δx and Δy during a time step, in other words $v_x \Delta t < \Delta x$, $v_y \Delta t < \Delta y$. These assumptions are met when a more general Courant condition is satisfied [110]

$$1 > (c\Delta t)^2 \left(\frac{1}{(\Delta x)^2} + \frac{1}{(\Delta y)^2} \right) \tag{3.25}$$

Four basic cases of particle motion during one time step are now considered. In the first case, the particle remains in the same cell during its movement, i.e. $i_1 = i_2$ and $j_1 = j_2$. In this case, particle trajectory stays straight, however, it is formally assumed that the movement of particle from (x_1, y_1) to (x_2, y_2) is described as a two-step movement, that is, at one step the particle moves from (x_1, y_1) to $(\frac{x_1+x_2}{2})$, and at the second step the particle moves from $(\frac{x_1+x_2}{2})$ to (x_2, y_2).

When the particle moves across cell meshes, the situation is not so clear, and, generally, the particle movement is decomposed according to Fig. 3.4. We have several options depending on positions of the particle at times t and $t + \Delta t$ (at the beginning and at the end of each time step).

When $i_1 \neq i_2$ and $j_1 \neq j_2$, the particle moves across two cell boundaries. The movement of the particle is decomposed in two consecutive movements during the time step - first, the particle moves from (x_1, y_1) to $(i_2 \Delta x, j_2 \Delta y)$ and then the particle moves from from $(i_2 \Delta x, j_2 \Delta y)$ to (x_2, y_2). In this case, the trajectory becomes a zigzag line, see Fig. 3.4a.

The cases, where the particle moves across one cell boundary, e.g. where $i_1 \neq i_2$ and simultaneously $j_1 = j_2$, or where $i_1 = i_2$ and simultaneously $j_1 \neq j_2$, are similar. If $i_1 \neq i_2$, $j_1 = j_2$, the movement is decomposed into two parts, the first part from (x_1, y_1) to $(i_2 \Delta x, \frac{y_1+y_2}{2})$ and the second part from $(i_2 \Delta x, \frac{y_1+y_2}{2})$ to (x_2, y_2), see Fig. 3.4b. If $i_1 = i_2$, $j_1 \neq j_2$, the movement of the particle is decomposed in the first interval from (x_1, y_1) to $(\frac{x_1+x_2}{2}, j_2 \Delta x)$ and in the second one from $(\frac{x_1+x_2}{2}, j_2 \Delta x)$ to (x_2, y_2).

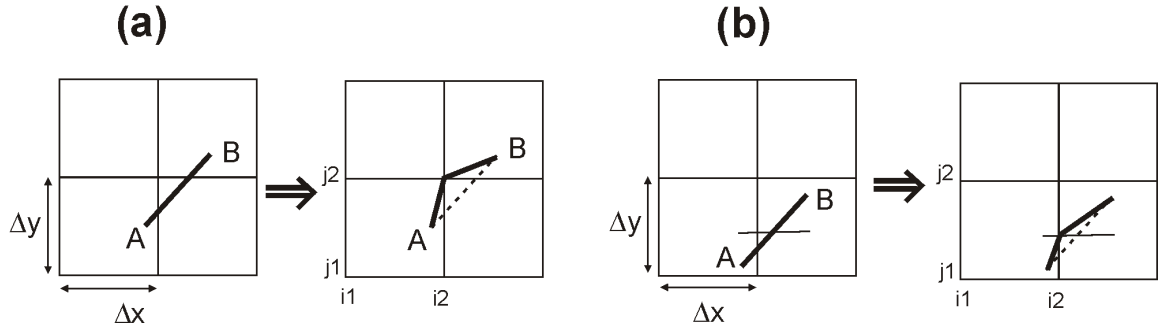

Figure 3.4: (a) When $i_1 \neq i_2$ and simultaneously $j_1 \neq j_2$, the movement of particle from A to B is decomposed in two movements. (b) The decomposition of particle trajectory from A to B in the case when $i_1 \neq i_2$ and $j_1 = j_2$.

When the particle remains in the same cell during its movement, it is the simplest case. Movement decomposition is only formal

$$J_x(i_1 + 1/2, j_1) = \frac{1}{ppc} F_x (1 - W_y) \qquad J_x(i_1 + 1/2, j_1 + 1) = \frac{1}{ppc} F_x W_y \tag{3.26}$$

$$J_y(i_1, j_1 + 1/2) = \frac{1}{ppc} F_y(1 - W_x) \qquad J_y(i_1 + 1, j_1 + 1/2) = \frac{1}{ppc} F_y W_x, \tag{3.27}$$

where F_x and F_y represent charge flux given by (3.28). W is the first-order shape factor (see [110]), which corresponds to the linear weighting function defined at the midpoint between points (x_1, y_1) and (x_2, y_2), see relations (3.29). ppc means the number of electrons per cell at critical density in the code. Current densities J_x, J_y are in dimensionless units (normalized by $en_{crit}c$) such as in Refs. [117], [118].

$$F_x = q\frac{x_2 - x_1}{\Delta t}, \qquad F_y = q\frac{y_2 - y_1}{\Delta t} \tag{3.28}$$

$$W_x = \frac{x_1 + x_2}{2\Delta x} - i_1, \qquad W_y = \frac{y_1 + y_2}{2\Delta y} - j_1 \tag{3.29}$$

Now it is convenient to put previous ideas together. New variables x_r (3.30) and y_r (3.31) are introduced by using min (minimum) and max (maximum) function

$$x_r = \text{min}(\text{min}(i_1\Delta x, i_2\Delta x) + \Delta x), \text{max}(\text{max}(i_1\Delta x, i_2\Delta x), \frac{x_1 + x_2}{2})) \tag{3.30}$$

$$y_r = \text{min}(\text{min}(j_1\Delta y, j_2\Delta y) + \Delta y), \text{max}(\text{max}(j_1\Delta y, j_2\Delta y), \frac{y_1 + y_2}{2})). \tag{3.31}$$

By using (x_r, y_r), the charge flux $(F_x, F_y) = q(v_x, v_y)$ is decomposed into (F_{x1}, F_{y1}) and (F_{x2}, F_{y2})

$$F_{x1} = q\frac{x_r - x_1}{\Delta t}, \qquad F_{y1} = q\frac{y_r - y_1}{\Delta t}, \tag{3.32}$$

$$F_{x2} = q\frac{x_2 - x_r}{\Delta t}, \qquad F_{y2} = q\frac{y_2 - y_r}{\Delta t}. \tag{3.33}$$

We define first-order shape factors from W_x, W_y to W_{x1}, W_{y1}, W_{x2}, W_{y2} in a similar way like F_x, F_y:

$$W_{x1} = \frac{x_1 + x_r}{2\Delta x} - i_1, \qquad W_{y1} = \frac{y_1 + y_r}{2\Delta y} - j_1, \tag{3.34}$$

$$W_{x2} = \frac{x_r + x_2}{2\Delta x} - i_2, \qquad W_{y2} = \frac{y_r + y_2}{2\Delta y} - j_2. \tag{3.35}$$

Finally, charge fluxes assigned to 8 grid points are determined.

$$J_x(i_1 + 1/2, j_1) = \frac{1}{ppc} F_{x1}(1 - W_{y1}) \qquad J_x(i_1 + 1/2, j_1 + 1) = \frac{1}{ppc} F_{x1} W_{y1} \tag{3.36}$$

$$J_y(i_1, j_1 + 1/2) = \frac{1}{ppc} F_{y1}(1 - W_{x1}) \qquad J_y(i_1 + 1, j_1 + 1/2) = \frac{1}{ppc} F_{y1} W_{x1} \tag{3.37}$$

$$J_x(i_2 + 1/2, j_2) = \frac{1}{ppc} F_{x2}(1 - W_{y2}) \qquad J_x(i_2 + 1/2, j_2 + 1) = \frac{1}{ppc} F_{x2} W_{y2} \tag{3.38}$$

$$J_y(i_2, j_2 + 1/2) = \frac{1}{ppc} F_{y2}(1 - W_{x2}) \qquad J_y(i_2 + 1, j_2 + 1/2) = \frac{1}{ppc} F_{y2} W_{x2} \tag{3.39}$$

In order to obtain total current densities, the charge fluxes contributed by each particle are superposed. The zigzag scheme determines current densities J_x and J_y from positions of particles at time instances t and $t + \Delta t$. J_z component is free from the charge continuity equation in two dimensions, thus J_z is simply calculated from velocities of particles in z direction and from the first-order weighting factor.

3.3.3 Particle solvers

Several numerical schemes can be used for calculation of positions and velocities of each particle, see Ref. [119]. Our PIC code employs a time-centered leap-frog scheme, which is presented in [110].

Basic equations for the movement of particles in the relativistic plasma are written as:

$$\frac{\vec{u}^{n+1/2} - \vec{u}^{n-1/2}}{\Delta t} = \frac{q}{m}\left(\frac{\vec{E}^n}{c} + \frac{\vec{u}^n}{\gamma^n} \times \vec{B}^n\right), \tag{3.40}$$

$$\frac{\vec{x}^{n+1} - \vec{x}^n}{\Delta t} = \frac{\vec{u}^{n+1/2}}{\gamma^{n+1/2}}, \tag{3.41}$$

$$\gamma = \sqrt{(1 + (\vec{u})^2)}, \tag{3.42}$$

where $\vec{u} = \vec{p}/(mc)$ is the dimensionless momentum of the particle.

Momentum $\vec{u}^n$ and magnetic field $\vec{B}^n$ are not known yet. $\vec{u}^n$ and $\vec{B}^n$ are replaced by the following approximations

$$\vec{u}^n = \frac{\vec{u}^{n+1/2} - \vec{u}^{n-1/2}}{2}, \tag{3.43}$$

$$\vec{B}^n = \vec{B}^{n-1/2} + \frac{\Delta t}{2}\nabla \times \vec{E}^n. \tag{3.44}$$

$\vec{u}^{n-1/2}$ and $\vec{u}^{n+1/2}$ are substituted as follows:

$$\vec{u}^{n-1/2} = \vec{u^-} - \frac{q\vec{E}^n \Delta t}{2mc}, \qquad \vec{u}^{n+1/2} = \vec{u^+} + \frac{q\vec{E}^n \Delta t}{2mc} \tag{3.45}$$

From relation (3.40) by using approximations (3.43), (3.44) and the latter substitutions, the following equation is obtained.

$$\frac{\vec{u^+} - \vec{u^-}}{\Delta t} = \frac{q}{2\gamma^n m}(\vec{u^+} + \vec{u^-}) \times \vec{B}^n \tag{3.46}$$

$\vec{u^+}$ is obtained by an explicit method which is called two-step rotation.

$$\vec{u'} = \vec{u^-} + \vec{u^-} \times \vec{r}, \qquad \vec{u^+} = \vec{u^-} + \vec{u'} \times \vec{s} \tag{3.47}$$

$\vec{r}$ and $\vec{s}$ denote the following relations:

$$\vec{r} = \frac{q\vec{B}\Delta t}{2\gamma^n m}, \qquad \vec{s} = \frac{2\vec{r}}{1 + (\vec{r})^2}. \tag{3.48}$$

The value of γ^n is determined as follows.

$$(\gamma^n)^2 = 1 + \left(\vec{u^-}\right)^2 \tag{3.49}$$

Finally, the new position is calculated

$$\vec{x}^{n+1} = \vec{x}^n + \vec{v}^{n+1/2}\Delta t = \vec{x}^n + \frac{\vec{u}^{n+1/2} c \Delta t}{\gamma^{n+1/2}}. \tag{3.50}$$

3.3.4 Interpolation of fields

In order to simulate the force acting on each particle, it is necessary to determine electric and magnetic fields at exact positions of particles as $\vec{E}$ and $\vec{B}$ is known only on the grid according to Fig. 3.3. For the interpolation of fields, the first-order weighting is used, defined by the following formulas [110], [115]. The first-order shape factors can be evaluated as:

$$S_i(\xi) = \begin{cases} 1 - |\xi - i| & \text{for } |\xi - i| \leq 1 \\ 0 & \text{for } |\xi - i| > 1 \end{cases} \tag{3.51}$$

where $\xi = \frac{x_p}{\Delta x}$, p means index of particle;

$$S_j(\eta) = \begin{cases} 1 - |\eta - j| & \text{for } |\eta - j| \leq 1 \\ 0 & \text{for } |\eta - j| > 1 \end{cases} \tag{3.52}$$

where $\eta = \frac{y_p}{\Delta y}$, p means index of particle.

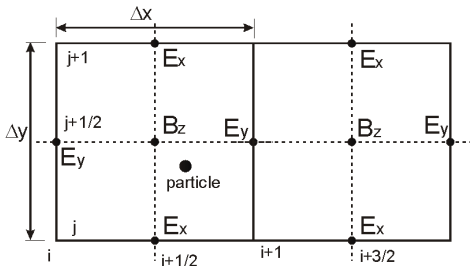

Figure 3.5: Positions of x and y components of $\vec{E}$ on the grid and the position of particle.

Finally, the components of fields are determined in the position of each particle $(E_x)_p$, $(E_y)_p$ and $(B_z)_p$:

$$\begin{aligned}(E_x)_p = {} & S_{i+1/2}(\xi)S_j(\eta)(E_x)_{i+1/2,j} + S_{i+1/2}(\xi)S_{j+1}(\eta)(E_x)_{i+1/2,j+1} \\ & + S_{i+3/2}(\xi)S_j(\eta)(E_x)_{i+3/2,j} + S_{i+3/2}(\xi)S_{j+1}(\eta)(E_x)_{i+3/2,j+1},\end{aligned} \tag{3.53}$$

$$\begin{aligned}(E_y)_p = {} & S_i(\xi)S_{j-1/2}(\eta)(E_y)_{i,j-1/2} + S_{i+1}(\xi)S_{j-1/2}(\eta)(E_y)_{i+1,j-1/2} \\ & + S_i(\xi)S_{j+1/2}(\eta)(E_y)_{i,j+1/2} + S_{i+1}(\xi)S_{j+1/2}(\eta)(E_y)_{i+1,j+1/2},\end{aligned} \tag{3.54}$$

$$\begin{aligned}(B_z)_p = {} & S_{i+1/2}(\xi)S_{j-1/2}(\eta)(B_z)_{i+1/2,j-1/2} + S_{i+1/2}(\xi)S_{j+1/2}(\eta)(B_z)_{i+1/2,j+1/2} \\ & + S_{i+3/2}(\xi)S_{j-1/2}(\eta)(B_z)_{i+3/2,j-1/2} + S_{i+3/2}(\xi)S_{j+1/2}(\eta)(B_z)_{i+3/2,j+1/2}.\end{aligned} \tag{3.55}$$

3.4 Boundary conditions

3.4.1 Boundary conditions for particles

Selection of a suitable boundary condition depends on the type and parameters of the simulated experiment. Our 2D3V PIC code enables to model interactions of laser beam with

thin foils, small-size targets or with thick solid targets. A small-size target is immediately ionized by the interaction and the whole target is situated in the simulation box. On the other hand, the thick solid target is ionized only near its surface layer and, thus, only this layer is modeled in the simulation box. Thus, different boundary conditions for particles are necessary for different types of targets.

Particles reaching the simulation box boundaries may be either reflected, frozen, or cooled down at the boundaries. Eventually, periodic boundary condition seems to be the best choice for sub-micrometer targets as all dimensions of the simulation box are limited to several microns and other interacting particles are in the vicinity to the simulation region, see Ref. [26]. When laser interaction with thick solid target is studied, the PIC code models only the target surface layer, and a special condition [120] is implemented at the boundary in the target interior where fast electrons leaving simulation region are replaced by thermal electrons carrying the return current.

3.4.2 Boundary conditions for fields

For the solution of Maxwell equations, we can add damping layers to any combination of boundaries in order to eliminate spurious reflection of outgoing electromagnetic waves from the simulation box boundaries. For two-dimensional (2D) case, we have successfully adopted the recipe described in 1D situation [121]. Special damp factor is added to the Maxwell equations via the masking function $f_M(x,y,r) = f_M(x,r) \times f_M(y,r)$, where

$$f_M(x,r) = \begin{cases} 1 & \text{pro } L_x + L_{Dx} > x > L_{Dx} \\ 1 - \left(r\frac{x-L_{Dx}}{L_{Dx}}\right)^2 & \text{for } x \le L_{Dx} \\ 1 - \left(r\frac{x-L_{Dx}-L_x}{L_{Dx}}\right)^2 & \text{for } x \ge L_{Dx} + L_x \end{cases} \tag{3.56}$$

L_x and L_{Dx} are widths of simulation box and of damping layers, respectively.

Electric and magnetic fields are calculated according to the following relations in each simulation time step:

$$\begin{aligned} \vec{E}^{n+1}(x,y) &= f_M(x,y,r_d) \times (\vec{E}^n(x,y) - f_M(x,y,r_r)\,\Delta t \times \\ &\quad (2\,\pi\,\vec{J}^n(x,y) - \nabla \times \vec{B}^{n+1/2}(x,y))), \\ \vec{B}^{n+1/2}(x,y) &= f_M(x,y,r_d)(\vec{B}^{n-1/2}(x,y) - f_M(x,y,r_r)\Delta t(\nabla \times \vec{E}^n(x,y))) \end{aligned} \tag{3.57}$$

The above equations are discretized Maxwell equations inside the simulation box and electromagnetic waves are damped and retarded inside damping regions. For higher efficiency of the damping regions, damping parameter r_r and retarding parameter r_d are set according to the relations proposed in Ref. [121]

$$r_r = \begin{cases} \sqrt{1-\Delta x}\frac{N_D}{N_D-1} & \text{pro } \Delta x \ge 1 - \left(\frac{N_D-1}{N_D}\right)^2 \\ 1.0 & \text{pro } \Delta x < 1 - \left(\frac{N_D-1}{N_D}\right)^2 \end{cases}, \tag{3.58}$$

$$r_d \approx \sqrt{\frac{3.5 r_r^2 \Delta t}{N_D \Delta x}\left(\frac{1}{2r_r}\ln\left|\frac{1+r_r\frac{N_D}{N_D-1}}{1-r_r\frac{N_D}{N_D-1}}\right| - \frac{N_D}{N_D-1}\right)^{-1}}, \tag{3.59}$$

where $N_D = L_{Dx}/\Delta x$ is the thickness of damping layer (in the number of cells).

3.5 Parallelization of the PIC code

During the course of this thesis, the PIC code was parallelized in order to improve its performance and to allow calculations with up to $\sim 10^8$ macroparticles and $\sim 3 \times 10^7$ cells. Our simulations were performed on JUMP cluster in Forschungszentrum Juelich in Germany and on computers at the Department of Physical Electronics in Prague. The JUMP cluster had several tens of nodes with 32 CPUs per node. High-performance computers at the Department of Physical Electronics have several CPUs with shared memory. Thus, the code was parallelized for shared-memory systems which is easier than for distributed memory systems, although the shared-memory systems have a limited number of CPUs.

The code, written in Fortran, uses OpenMP (Open Multi-Processing), which is an application programming interface that supports shared memory multiprocessing programming in C, C++ and Fortran on many architectures, including Unix and Windows platforms. OpenMP consists of a set of compiler directives, library routines, and environment variables that influence run-time behavior. It uses the fork-join model of parallel execution, see Fig. 3.6.

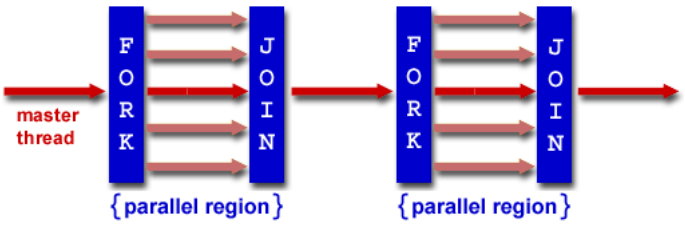

Figure 3.6: Fork-join model of parallel simulation run for shared memory systems.

All OpenMP programs begin as a single process - the master thread, which executes sequentially until the first parallel region construct is encountered. The master thread then creates a team of parallel threads (the so-called fork) and the statements in the code that are enclosed by the parallel region construct are then executed in parallel among the various team threads. When the team threads complete the statements in the parallel region construct, they synchronize and terminate, leaving only the master thread (the so-called join). Most OpenMP parallelism is specified through the use of compiler directives which are embedded in the source code. It is entirely programmer's responsibility to insure that all variables in the code and input/output are conducted correctly within the context of multi-threaded program. More details about OpenMP and compiler directives are freely accessible in Ref. [122].

3.6 Conclusion

To describe plasma interacting with a high-intensity laser pulse and related phenomena, an approach which considers the particle distribution function in the phase space is necessary since the system is certainly out of the local thermodynamic equilibrium. One possibility is to solve directly the Vlasov equation describing the temporal evolution of the single-particle

distribution function, which consumes, however, too much computational power. Another possibility (usually more efficient) is to sample the distribution function in the phase space by numerical macro-particles, which is, in fact, the particle-in-cell (PIC) method.

PIC codes calculate arbitrary positions and momenta of all macro-particles in the simulation box at each time step. The motion of the particles is influenced by electric and magnetic fields calculated on the grid by discretized Maxwell equations and interpolated to the positions of the particles. Moreover, the charge continuity equation has to be satisfied in a finite discrete scheme, which determines the computation of charge and current densities on the grid.

In our two-dimensional PIC code, the validity of the continuity equation is ensured by the zigzag scheme which has an advantage in computation speed compared to other charge conservation schemes assuming particle trajectories over one time step as a straight line. Relativistic equations of motion are solved by two-step Boris rotation, fields in the positions of particles are determined by bilinear interpolation. Leap-frog method is used, and thus macro-particle velocities and magnetic fields are computed in the middle of time step, while particles positions and electric fields are calculated in the time step edges.

The most problematic issue of PIC simulations is the employment of suitable boundary conditions, since the inappropriate conditions can lead to incorrect numerical results. Different boundary conditions for the particles are suitable for different types of targets - periodic conditions are usually appropriate for sub-wavelength targets, particles may be frozen or cooled down and reflected at the simulation box boundaries for mass-limited targets (of all sizes of several laser wavelengths), and, finally, fast electrons leaving the surface layer of thick solid target into the target interior located out of the simulation box can be replaced by thermal electrons carrying the return current. Our contribution is mainly in absorbing boundary conditions for fields. We have successfully adopted these conditions described in one-dimensional case by simply multiplying 1D masking functions related to all spatial coordinates in two-dimensional case. Reliable functioning of relatively thin damping layers is verified at the beginning of Chapter 4.

Finally, we should note that there exists numerous PIC codes with various algorithms. However, it is not usually easy to obtain them as they represent "know-how" of certain laboratories or physicists. Moreover, to be familiar with a numerical code, it is necessary to be frequently in contact with its authors, or to have a detailed description of the code (manual) which is not usually the case. At our department, we have also used and modified freely accessible 1D PIC code LPIC++ [61], [117], which is, however, not useful for the simulations of femtosecond laser pulse interaction with small-sized targets where two spatial dimensions are necessary at least. Thus, numerical results presented below in this thesis are obtained with our 2D PIC code described above. According to our knowledge, there are other numerical multidimensional PIC codes mentioned in various articles on ion acceleration by intense laser pulses, namely CALDER [123], ILLUMINATION [124], OOPIC [125], OSIRIS [126], PICLS [85], VLPL [127], or VORPAL [128].

Chapter 4

Interaction of an Intense Laser Pulse with Mass-limited Targets

This chapter is firstly devoted to the numerical study of the interaction of femtosecond laser pulses with mass-limited targets (MLTs) of various shapes. Secondly, the chapter includes presentation/explanation of the first experimental results using thin foils of reduced surface, which fits well in the context of this chapter and confirms our previous theoretical predictions.

MLTs are usually defined as the targets with all dimensions comparable to the laser spot size [129]-[131]. Our objectives are to study the efficiency of ion acceleration in MLT targets of various shapes and composition (one or two ion species). We also varied laser (duration, intensity) and plasma (maximum density, initial density profile) parameters to observe how they affect the acceleration process.

4.1 Interaction of extremely short ultraintense laser pulse with hydrogen plasma

Firstly, we studied the interaction of a hydrogen plasma of a density of several times the critical density with short laser pulses of a duration only about several laser periods and an intensity at the margin of relativistically induced transparency. This interaction regime may become accessible in future laser systems, such as in ELI project [132], although the density of plasma and the laser intensity should be higher in reality, but the ratio will be the same as in the following preliminary simulations. Our main goal has been the demonstration of higher ion acceleration efficiency in the case of mass-limited targets.

In this set of simulations, the incident laser pulse of the wavelength $\lambda = 800\ \mathrm{nm}$ is assumed to have the dimensionless amplitude $a_0 = 10$ ($I \approx 2.1 \times 10^{20}\ \mathrm{W/cm^2}$). The laser pulse shape is of $\sin^2$ form for the full duration 5τ or 10τ (i.e., 13 fs or 26 fs), where τ is the time of the laser cycle. A Gaussian transverse profile of the laser beam is assumed with the beam full width 4λ at half maximum (FWHM). Laser interactions with fully ionized hydrogen targets of electron density $n_e = 4n_{crit}$ and various geometrical forms - sphere of a diameter 4λ, a planar foil and a foil section of the square shape of the same thickness 4λ - are studied. In 2D geometry, the sphere is modeled by an infinite cylinder and the foil

section is modeled by an infinite rectangular parallelepiped. Target expansion due to a laser pulse precursors is disregarded and a sharp plasma-vacuum boundary is assumed when the simulations are started.

4.1.1 Interaction of the pulse with a cylindrical target

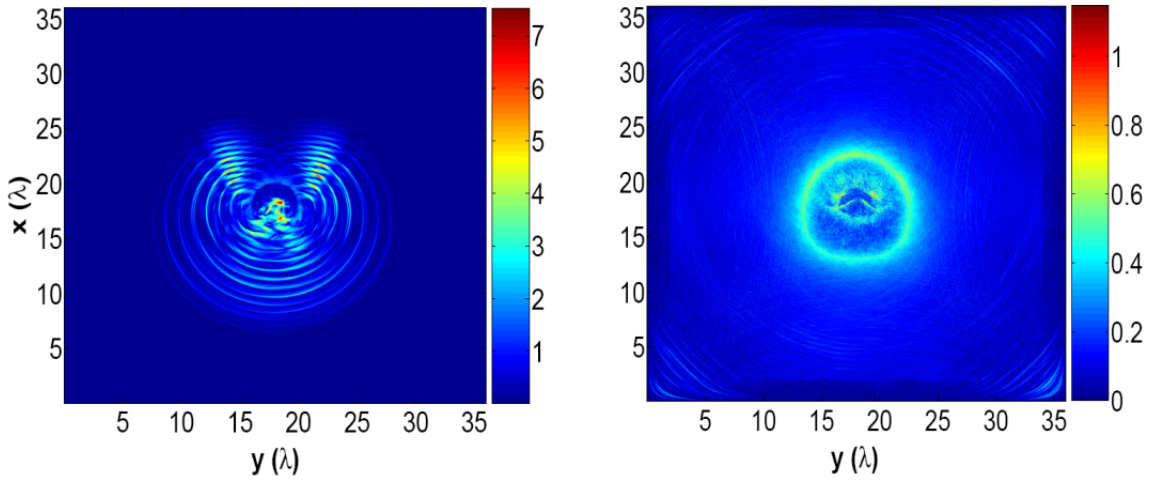

Figure 4.1: Normalized absolute value of electric field $eE/(m_e\omega c)$ during the interaction of laser of amplitude $a_0 = 10$, pulse duration 10τ, and beam width 4λ with a homogeneous plasma sphere of a diameter 4λ and an initial density $n_e = 4n_{crit}$. Coordinates are normalized by λ, dummy damping regions 2λ wide at each side of simulation box are included. The left and right figures are plotted in moments 5τ and 30τ after the laser maximum reaches the sphere front side. The laser pulse propagates along x-axis.

Now we will discuss the interaction of a p-polarized laser pulse with a hydrogen droplet. The absolute value of normalized electric field is presented in Fig. 4.1. We plot here the full simulation region including dummy damping regions of width 2λ on all simulation box boundaries, where no particles are allowed. The left snapshot in Fig. 4.1 taken 5 periods after the laser maximum reached the sphere front demonstrates reflection, diffraction, and scattering of laser wave on the sphere. The right snapshot is taken 30τ after laser pulse maximum when all electromagnetic waves left the simulation box. This snapshot verifies excellent function of damping region. The estimated reflection from simulation box boundaries is ≤ 0.003 of the maximum laser pulse intensity, for values $r_d = 0.06$, $r_r = 1$, and $L_D = 2\lambda$ defined in Chapter 3.

The corresponding energy balance of the interaction is presented in Fig. 4.2. When the laser interacts with the target front side, the kinetic energy of electrons rises rapidly with fast oscillations in kinetic and field energy, caused by electron oscillations in the field of laser wave. Later, small oscillations with a period of about 6τ are observed. These oscillations are caused by the electron motion back and forth through the droplet target. During electron motion inside sheath layers, part of its kinetic energy is transferred to the field energy. These oscillations are more pronounced for shorter laser pulses and for lower laser intensities when they are damped more slowly. The simulation also demonstrates a gradual transfer of the

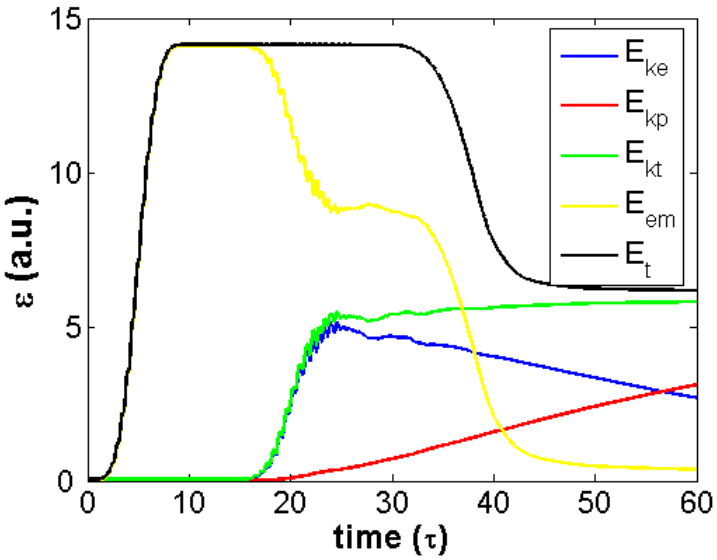

Figure 4.2: Energy (arbitrary units used in the code) balance in the simulation box versus time in laser periods τ for laser interaction with a spherical target of a diameter 4λ and a density $4n_{crit}$. E_{ke}, E_{kp}, E_{kt} are electron, proton and total kinetic energies, E_{em} denotes the electromagnetic field energy, and E_t is the total energy in the simulation box. The laser enters the simulation box in the first 10 periods τ and interacts with the target front size between 15τ and 25τ. Ions are accelerated after 20τ and the radiation leaves the simulation box between 30τ and 45τ.

electron kinetic energy to the proton energy mediated by the electrostatic fields in the sheath. The total absorption of the laser pulse energy is about 35% in this case. Damping regions start to absorb outgoing electromagnetic waves at time instant about 30τ and the total field energy at the end of simulation (60τ) is mainly due to electrostatic fields caused by the charge separation as the electrons have still enough kinetic energy and the acceleration of protons has not been yet terminated.

Although the target is initially relativistically transparent as $\gamma_L \approx 7$ and, thus, $n_e < \gamma_L n_{crit}$ according to (2.42), almost instantaneous local increase of the target density due to the action of ponderomotive force excludes laser-target interaction in this regime and the laser pulse is reflected from the formed dense layer at the target front. However, the laser pulse absorption is relatively high in this "transitional" interaction regime in spite of the initial step-like density profile (about 35% for p-polarization and approximately twice lower for s-polarization) since the dense layer, where the laser radiation is reflected, is located towards the target interior and a thin front surface layer (in front of the dense layer) works like a preplasma.

4.1.2 Enhanced ion acceleration due to reduction of the sheath width

The majority of hot electrons are accelerated at the target front side inward into the target due to electron heating mechanisms ($j \times B$, Brunel vacuum heating). The number of hot electrons can be estimated by the formula $N_h \approx \eta\varepsilon_L/\varepsilon_{eh}$, where ε_L and ε_{eh} are laser

and average hot electron energies, and η is the laser transformation efficiency into the hot electron energy, which is close to the laser absorption for our conditions. The average energy of hot electrons accelerated at the target front side can be estimated as the electron can acquire energy equal to the ponderomotive potential (2.50), $\varepsilon_{eh} \approx m_e c^2(\gamma_L - 1)$, where $\gamma_L = \sqrt{1 + a_0^2/2}$ for linearly polarized laser pulse. The increase of the hot electron number with the laser pulse duration τ_L and laser energy is demonstrated in Fig. 4.3. It means that the absorption coefficient and the hot electron temperature do not change significantly at a constant laser intensity. The electron distributions plotted in Fig. 4.3 in a logarithmic scale are nearly linear in the region 1-8 MeV, and thus they correspond to a Maxwellian distribution with a hot electron temperature $T_h \approx \varepsilon_{eh}$.

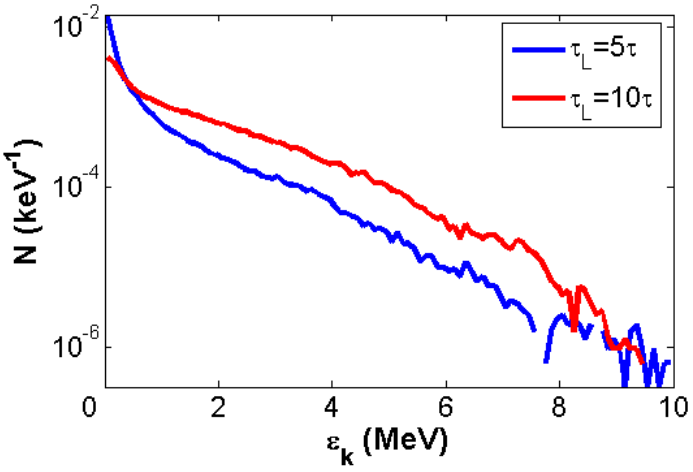

Figure 4.3: Spatially averaged electron distribution function at time t=30τ for the laser interaction with a spherical target of a density $n_e = 4n_{crit}$ and of a diameter 4λ. The laser pulse duration is $\tau_L = 5\tau$ and 10τ.

Generated hot electrons cross the target and propagate beyond its rear side. When the electrons reach the target rear surface, they escape into vacuum. While a small number of hot electrons penetrate far into vacuum, the majority of them is stopped and returned into the target by the self-generated electrostatic field. The average distance of hot electron excursion into vacuum is determined by the hot electron Debye length $\lambda_{Dh} \approx \sqrt{\epsilon_0 \varepsilon_{eh}/(e^2 n_h)}$. Hot electron density is estimated by the relation $n_h \approx N_h/(S_r c\tau_L)$, where S_r is the cross-section of the hot electron cloud behind the target rear side and τ_L is the laser pulse duration.

For the foil target, the cross-section of the sheath area at the rear side is considerably increased $S_r >> S_f$ in comparison with the laser focal spot S_f. First, the electron beam widens during laser propagation through the foil and second, the transverse velocity is preserved and even enhanced due to the electron repulsion when electron enters the vacuum, and the longitudinal velocity is decreased and reversed. Later in time, the sheath area is increased due to the electron beam widening during its propagation back and forth through the foil. This effect is demonstrated in Fig. 4.4 where the foil is initially irradiated by the laser beam of a diameter 4λ and, finally, the electric field covers the area of more than 10λ at the foil rear side. A periodic structure of the laser electric field is also shown in Fig. 4.4,

together with an additional laser focusing due to the target surface bending by the ponderomotive force action.

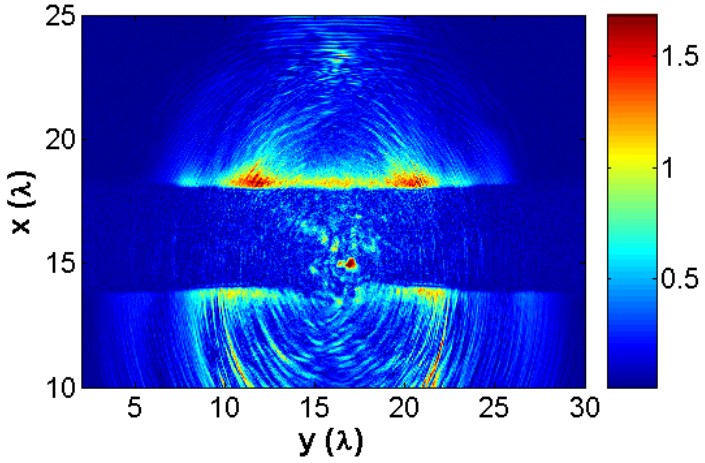

Figure 4.4: Electric field distribution at time t=30τ for the interaction of a laser of an amplitude $a_0 = 10$, a pulse length $\tau_L = 5\tau$ and a beam width 4λ with plasma-foil target of a density $n_e = 4n_{crit}$ and a thickness 4λ. The field is in dimensionless units $e|E|/(m_e\omega c)$.

We have shown above that an important difference of a planar foil from a droplet target is in the width of sheath layer at the target rear side. The sheath layer at the foil target is several times broader than the laser spot, and consequently, the hot electron density in the sheath is reduced. A lower hot electron density in the sheath reduces the efficiency of ion acceleration. This is demonstrated in the distribution function of laser accelerated protons in Fig. 4.5. Beside the target dimensions, the ion energy depends also on the target shape. Mass-limited targets of squared and spherical shapes are considered in the simulations - the maximum energy for the rounded target is about 7 MeV, for the rectangular target about 6 MeV, in comparison with a planar foil where the proton cutoff energy slightly exceeds 3 MeV. Thus, the circular shape seems to be preferred to the rectangular form as the laser pulse absorption is enhanced by the presence of a curvature at the front side of the target. In this case, the laser pulse arrives on the target on larger angles giving rise to a more efficient collisionless absorption and to higher electron energies. On the other hand, the proton angular distribution is very broad and the anisotropy is relatively small for a spherical target: the fast protons angular density in the direction of incident laser beam is 2.5 times higher than that in the opposite direction. Moreover, the simulation on the interaction of the droplet with the laser pulse of twice longer duration (10τ) have shown the maximum energy increase from 7 MeV to 11 MeV. The enhancement of proton energy is due to a higher number of generated hot electrons, which increases the accelerating electric field in the sheath.

We should note that there exists an optimum value of laser and target radius maximizing the efficiency of laser energy transformation into fast ions. Interaction of a very narrow laser beam corresponds to the regime of plane target, while the geometrical losses of the laser energy are large for a very broad laser beam (compared with the target radius). In Fig. 4.6, we demonstrate the dependence of the efficiency of ion acceleration on the ratio of the foil

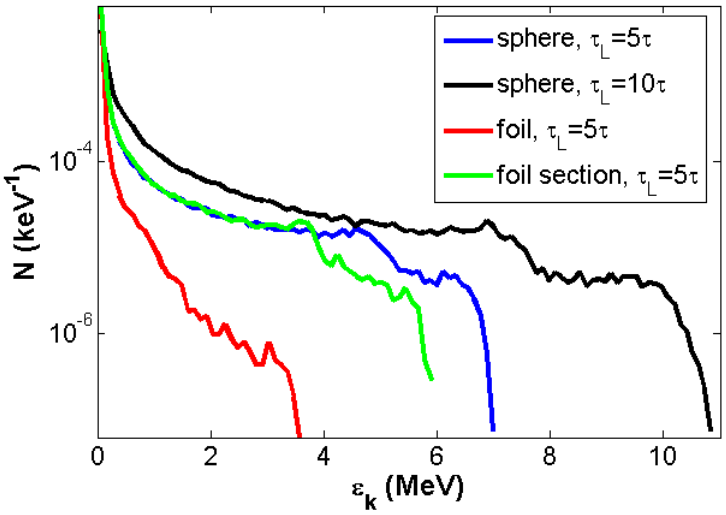

Figure 4.5: Fast proton spectra calculated for the spherical target of a diameter 4λ, and for the laser normal incidence on a foil and a foil section (square) of the same thickness 4λ. The laser amplitude $a_0 = 10$, pulse durations $\tau_L = 5\tau$ and 10τ. The initial electron density is $n_e = 4n_{crit}$ in all the targets.

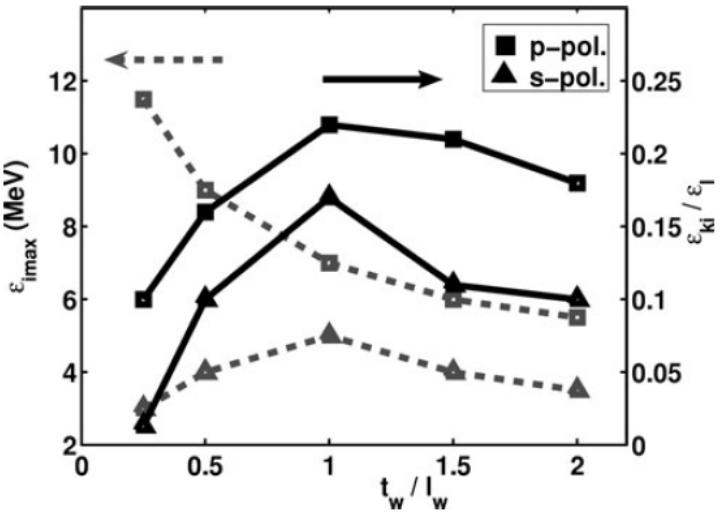

Figure 4.6: Maximum ion energy (dashed lines) and the efficiency of laser energy transformation into the fast ions (solid lines) versus the ratio of the foil section target width t_w to the Gaussian laser beam FWHM width l_w for the case of p-polarization (squares—laser electric field in the simulation plane) and s-polarization (triangles—laser electric field normal to the simulation plane).

section target width to the laser beam width. Here, the laser pulse of a duration 10τ and of a maximum intensity $a_0 = 10$ incidents normally on an ionized foil section composed of electrons and protons of the density of $4n_{crit}$. The laser beam width is fixed at $l_w = 4\lambda$

(FWHM) as the foil thickness, and the target width t_w varies from 1λ to 8λ. In the case of s-polarization, the fast ion energy maximizes for the target width equal to the laser beam width, as the laser diffraction for a narrower target does not lead to an increase of the accelerating electric field. On the other hand, the diffraction increases the accelerating field for the case of p-polarization and thus, the increase of maximum ion energy is maintained when the target is narrowed further. However, the energy transformation efficiency is maximal for the target width equal to the laser beam width for both polarizations. Due to a more efficient absorption and diffraction effects, both maximum ion energies and transformation efficiencies are higher for p-polarization.

4.1.3 Spectra of emitted radiation from planar and spherical targets

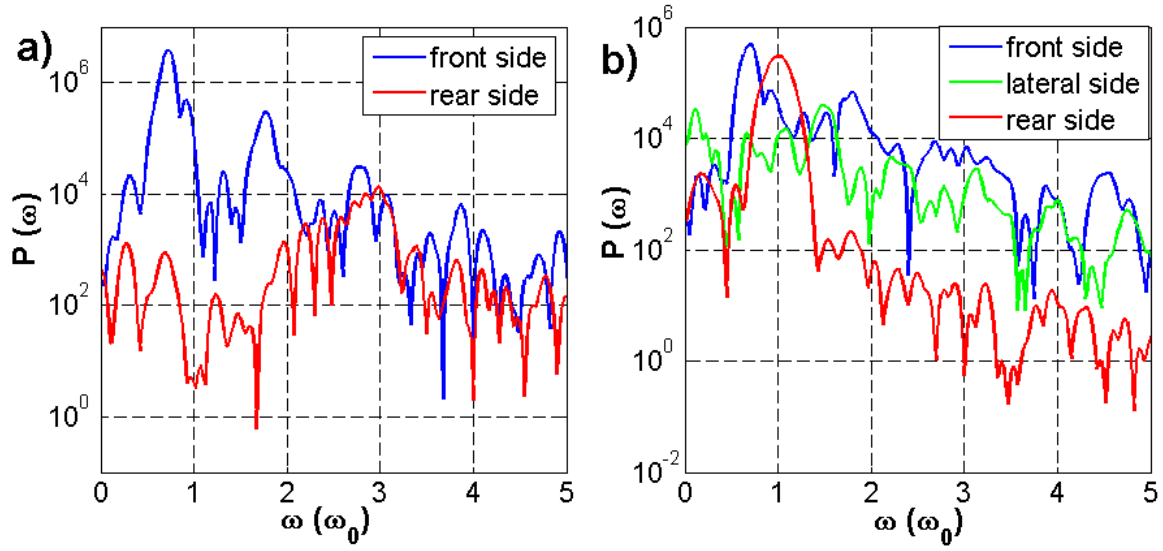

Figure 4.7: Emission spectrum of (a) planar and (b) spherical target on the front, rear, and lateral sides. Frequency is normalized on the laser frequency ω_0.

To illustrate the physics of interaction of the laser pulse with a planar foil and a droplet from another point of view, the frequency spectra of radiation emitted from the front and rear side of planar and spherical targets are plotted in Fig. 4.7. The spectra are calculated from the temporal evolution of emitted electric fields by the fast Fourier transform. The fields are "measured" (in our numerical simulations) at the distance of 10λ from the target center at corresponding directions from the target and in an appropriate time interval for the propagation of the emitted electromagnetic waves. The emission on laser harmonics from the front side is shifted to the red side due to the critical surface motion induced by the ponderomotive force. The first and second harmonics are suppressed on the rear side of the planar foil as the target of initial density $n_e = 4n_{crit}$ is transparent only for the third harmonic emission. The amplitude of the first harmonic on the rear side of the spherical target is comparable to that on the front side due to laser diffraction. It is also shown in Fig. 4.7b that a low-frequency electromagnetic radiation (in comparison to laser frequency) is emitted from the spherical target in the transverse direction due to the formation and relaxation of the

longitudinal dipole of hot electrons (it corresponds to small oscillations in electron kinetic and field energies with period of about 6τ shown in Fig. 4.2).

4.1.4 Scaling of hot electron temperature and maximum proton energy with the laser intensity

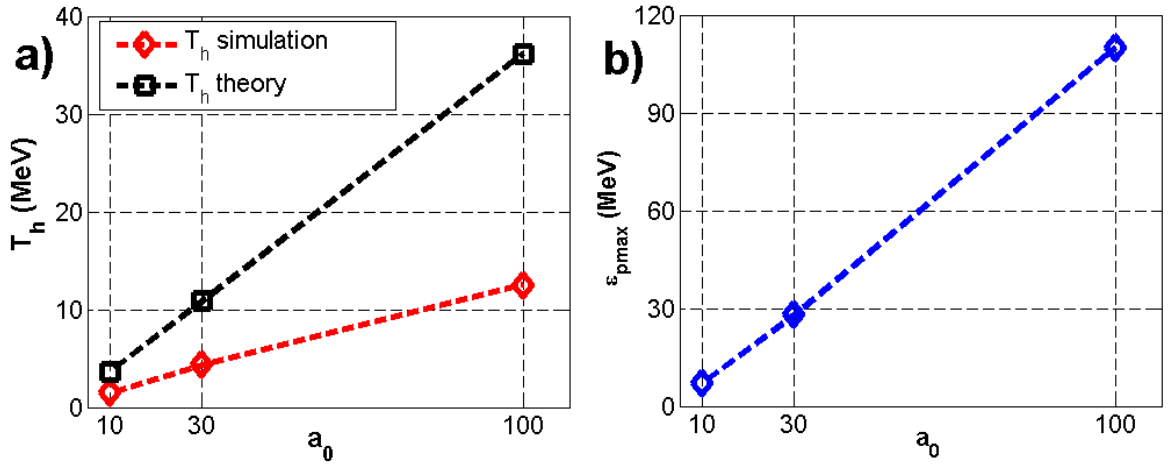

Figure 4.8: a) Hot electron temperature T_h versus the laser dimensionless amplitude a_0 after the interaction of laser pulse of duration 5τ with a cylindrical hydrogen target of a diameter 4λ. The PIC simulation results are plotted by a red line, while the analytic approximation (according to the ponderomotive scaling) by the black line. b) Dependence of maximum proton energy ε_{pmax} at the end of simulation (about 30τ after laser-plasma interaction) on laser amplitude a_0 for the same simulation parameters.

Finally, we investigate the scaling of the hot electron temperature and the maximum proton energy with the laser pulse intensity (dimensionless amplitude a_0) for the cylindrical target. Additional simulations were carried out for a_0=30, a_0=100 and for target densities n_e=12n_{crit}, n_e=36n_{crit}, respectively, in order to avoid relativistic laser transparency of the target.

Calculated hot electron temperatures inferred from the electron momenta snapshots immediately after laser-plasma interaction demonstrate that the ponderomotive scaling (2.50), which can be written as $T_h \approx m_e c^2 a_0/\sqrt{2}$ for $a_0 >> 1$ and linearly polarized laser pulse, is overestimated, see Fig. 4.8a. Based on this set of numerical simulations, we estimate the scaling of hot electron temperature on dimensionless amplitude as $1/c_1 \times a_0^{c_2}$ where the constant c_1 is in the interval (3.5; 4.0) and c_2 in (0.35; 0.45).

The dependence of maximum proton energy on the laser intensity is plotted in Fig. 4.8b. Here, it is not possible to compare simulation results with analytical estimate (2.72) because a very short acceleration time (if we consider that the acceleration time for the isothermal model [66] should be comparable with the laser pulse duration) leads to $\omega_{pih}^{-1} > t_{acc}$ and thus $\omega_{pih} t_{acc} < 1$ where the isothermal model fails.

4.2 Ion acceleration by femtosecond pulses in multispecies targets

In this set of simulations, we have studied the interaction of ultrashort laser pulses with MLT targets of various shapes containing a homogeneous mixture or compound of different elements. We are interested in the efficiency of ion acceleration, in the energy spectrum, and in angular distribution of fast protons depending on the size and geometric shape of MLTs.

It has been shown in Fig. 4.5, that the energy spectrum of ions originated from hydrogen plasma is broad, the energy distribution function of accelerated protons is roughly exponentially decreasing with the cutoff energy at the front of expanding plasma in agreement with theoretical models presented in Chapter 2. Foil targets containing a high-Z substrate and a very thin low-Z layer at the rear side were proposed in Ref. [133] in order to enhance the energy conversion efficiency and to improve the energy spectrum of fast ions. An additional important requirement is that the transverse size of the low-Z coating layer must be smaller than the laser focal spot in order to assure uniformity and good quality of accelerated beams [14]. Another approach has been proposed in Refs. [42], [43]. The authors suggest using a mixture of two or more ion species in a thin rear layer, which allows us to produce a proton beam with a small energy spread.

In our case, we employed multispecies targets of a uniform composition. This type of target can be considered in experiments when usual deposits are removed by heating the target to a high temperature before laser-target interaction [87]. However, this model can be also applied when the contaminant layer is not sufficiently thin to accelerate the whole layer (in fact, only ions originating from a very thin layer of the thickness at most of several tens of nm are accelerated by TNSA mechanism). Alternatively, a specific type of mass-limited targets, water or heavy water microdroplets used in recent experiments [19]-[24] are naturally free from contaminants as they are created directly in the focal spot a few milliseconds before the laser shot.

Ion acceleration in those targets has been theoretically described in Ref. [25]. The electrons accelerated and heated by a laser pulse on the front side of the target form a population of hot electrons. These hot electrons cross the target and propagate beyond its rear side. There, a sheath layer is formed and a strong electric field accelerates ions. The strong electric field provides a spatial separation of fast protons and heavy ions. Their mutual interaction strongly affects the shape of the proton distribution and the total efficiency of the process.

Next results are based on 2D PIC simulations with the following parameters. In order to investigate the role of target shape on the proton acceleration, fully ionized targets of a uniform composition of three different shapes have been employed: (i) A cylinder with a diameter of 3λ, which serves as a model of the microdroplet in the 2D case; (ii) a flat foil section of size $3\lambda \times 4\lambda$; (iii) a curved foil section [134] of size $3\lambda \times 4\lambda$ with radius of curvature 4λ at the rear side. Additionally, density ramps were introduced at the front and rear side in order to assess the effect of target expansion on the fast electron generation and ion acceleration. The simulation geometry is shown in Fig. 4.9. The targets contained two ion species (protons and "heavy" C^{4+} ions in ratio 1:1) and they were irradiated at normal incidence by a p-polarized laser pulse of wavelength $\lambda = 800\ \mathrm{nm}$ and intensity $I = 4.5 \times 10^{19}\ \mathrm{Wcm}^{-2}$ (dimensionless amplitude $a_0 = 4.6$). The pulse length was 12 laser cycles

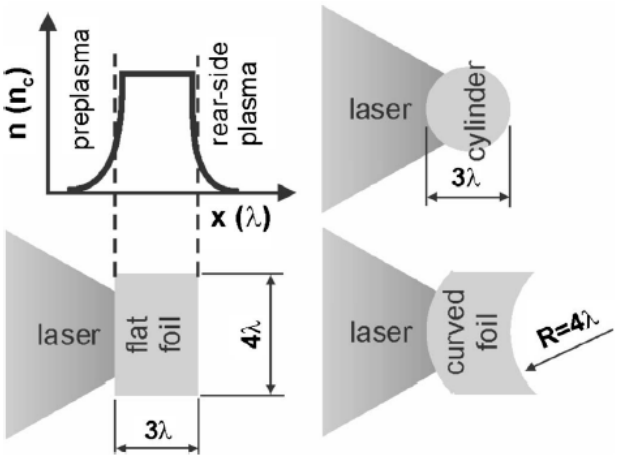

Figure 4.9: Three targets of various shapes and their density profile with preplasma and rear-side plasma density ramps.

(about 30 fs) with $\sin^2$ shape and the beam at full width at half maximum was 2.5λ at the focal spot. To prevent numerical heating, the initial temperature was set to 1 keV (for the cell size $\lambda/100 \times \lambda/100$ in the simulation box). This relatively high temperature can be justified for mass-limited targets. Our preliminary simulations have shown that the cold electron temperature increases to several keVs during the interaction with laser of relativistic intensity in a few femtoseconds. To decrease computational demands, the initial electron density was set to $20n_{crit}$ (where n_{crit} is the critical density), although the density corresponding to this degree of ionization should be about $150n_{crit}$ in a solid target. Our preliminary simulations have shown that the employment of targets with higher initial densities leads to somewhat lower absorption and energies of accelerated ions. Nevertheless, the energies are at the same order and qualitative results are similar.

4.2.1 Mutual interaction of two ion species

The formation of proton bunch is demonstrated in Fig. 4.10 which shows the phase space (x, v_x) of protons and C^{4+} ions beyond the rear side of a flat foil section at the time of 200 fs after the interaction. Initially, a thin layer (a few nm or tens of nm, depending on initial maximum target density and density profile) of protons at the rear target surface is accelerated by a strong electric field ($\sim 10^{12} - 10^{13}$ V/m). Carbon ions from this layer are accelerated somewhat later because of their inertia. They shield the sheath electric field from protons seated deeper in target and also interact with earlier accelerated protons. The in-flight interaction between protons and carbon ions compensates partially for the effect of Coulomb repulsion and maintains for a long time a narrow proton energy spectrum. Protons accelerated from the front side are also observed due to another sheath layer formed at the front side of the target where electrons are swept by the ponderomotive force [3]. Our preliminary simulations have shown that the energy of those protons is reduced as the target density increases (even without collisions which are not taken into account in our code). It has been also proved experimentally [86] that ions originated from the rear surface of thin

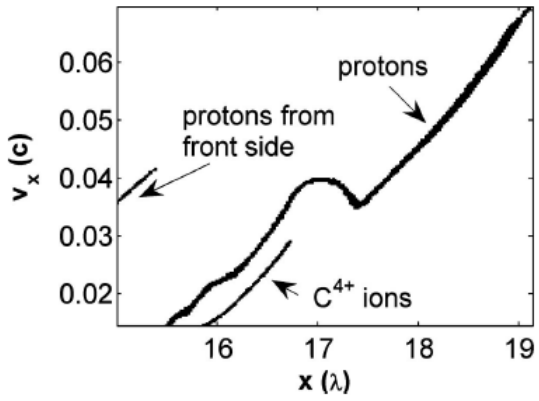

Figure 4.10: Phase space (x, v_x) of ions beyond the rear side of the foil section at 200 fs after the interaction. Initially, the target is located between 12λ and 15λ and a step-like density profile is assumed.

foils strongly prevail except for preheated targets with a smooth density gradient at the rear surface.

Figure 4.11 shows the proton energy distribution beyond the rear side of CH targets of various shapes. The laser pulse has the same parameters in all cases. The fast protons are separated from the thermal particles by a deep dip, so the spectrum consists of a peak and a high energy tail, which is caused by the presence of the C^{4+} ions. At the beginning of the acceleration process, each ion species (protons and "heavy" C^{4+} ions) from the rear target surface is accelerated independently without feeling each other. Because of a different charge to mass ratio, a spatial separation of ion species develops. Then, protons from deeper layers of the rear target surface are not accelerated so rapidly, because carbon ions from outer layers shield the sheath electric field formed by hot electrons. Thus, only protons from a thin layer (which is of the order of a few Debye lengths in the target) at the rear target side can be accelerated. These protons are separated spatially and in the energy distribution from the rest of the target. The thickness of this layer, Δp, can be estimated from the equation of electron pressure $-eE_{ac} + \nabla P/n = 0$:

$$\Delta p \approx \frac{n_h T_h + n_c T_c}{eE_{ac}(n_h + n_c)} \tag{4.1}$$

where $P = n_h T_h + n_c T_c$ is the thermal electron pressure, e is the elementary charge, E_{ac} is the sheath electric field, n_h, n_c are the densities, and T_h, T_c are the temperatures of hot and cold electrons, respectively, in the sheath layer. In our case, for the parameters inferred from the simulation ($E \approx 3\times10^{12}\,\mathrm{V/m}$, $n_h \approx 3n_{crit}$, $n_c \approx 20n_{crit}$, $T_h \approx 105\,\mathrm{keV}$, $T_c \approx 1.5\,\mathrm{keV}$), $\Delta_p \approx 5\,\mathrm{nm}$ for the flat foil. For a steep density profile or for a density ramp, a thicker layer is expected.

The protons are accelerated by the sheath electric field and, at the same time, they explode in space due to the effect of Coulomb repulsion. This explosion in the parallel direction is partly compensated by the electric field of carbon ions which are lagging behind protons and work like a piston. The fastest protons are accelerated by electric fields, created both by the fast electrons and the protons themselves. They form an energetic tail in the proton

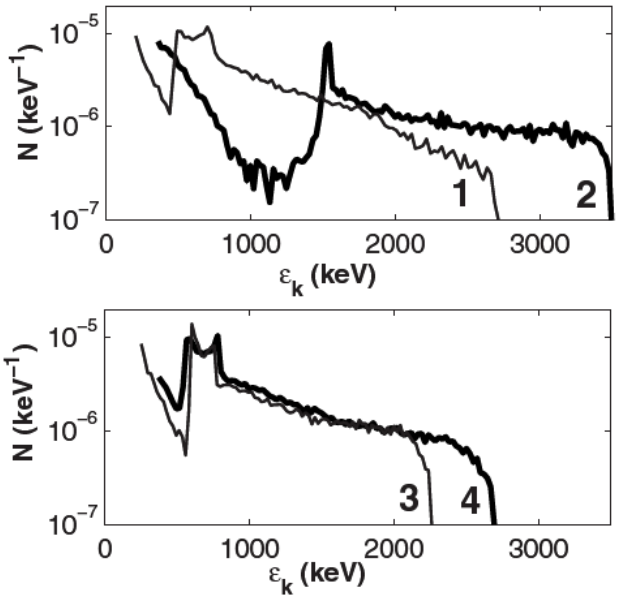

Figure 4.11: Proton energy spectra for three target shapes at the time of 200 fs after the interaction (line 1, curved foil; line 2, cylinder; line 3, flat foil), and for the flat foil section at the time of 300 fs (line 4).

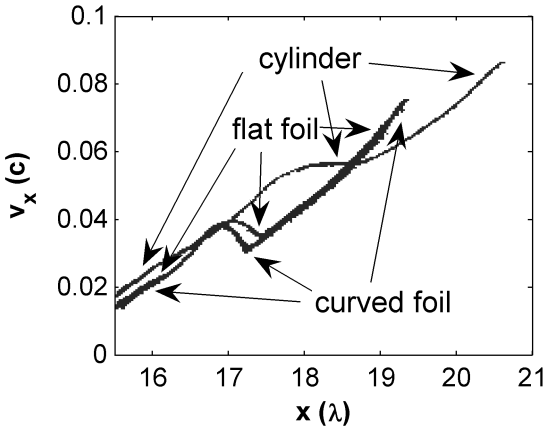

Figure 4.12: Phase spaces (x, v_x) of protons beyond the rear side of three different targets at the time of 200 fs after the interaction. The target is initially located between 12λ and 15λ.

spectrum. (These ions can be seen in Fig. 4.12 in the domain $x > 18\lambda$.) The slower protons, which are located in the rear side of the bunch, feel an additional electric field created by the expanding carbon ions. These carbon ions create a peak in the spatial proton distribution, which can be seen in Fig. 4.12 as a V-shaped structure in the domain $17\lambda < x < 18\lambda$. The peak in the proton energy spectrum corresponds to a plateau in the phase space, that is, the protons of the same energy are spread in the coordinate space. Nevertheless, as a time goes on, under action of the Coulomb field, some protons overtake the others producing a fine structure of the peak. In the case of a cylindrical target (solid thick line in Fig. 4.11), the

number of protons in the peak is relatively small and the two-peak structure is not observed in the simulation. This is due to a high angular divergence, which leads to lower densities of fast protons. Thus, the effect of space charge decreases and the peak evolves slower in time. This can be seen in Figs. 4.12 and 4.13.

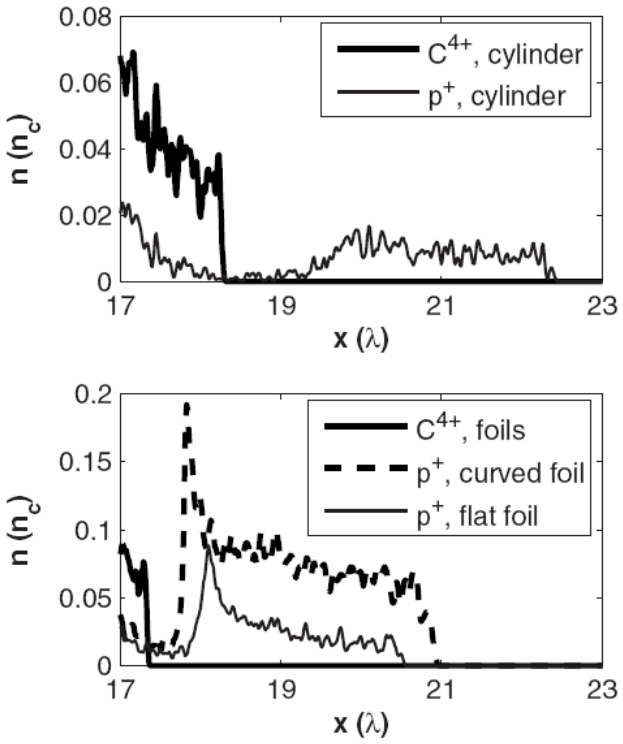

Figure 4.13: Densities of protons and carbon ions on the axis at 250 fs after the interaction. The initial position of the target is between 12λ and 15λ. Density profiles of carbon ions from the flat and curved foils are similar, hence they are plotted by the same line.

Figure 4.11 demonstrates that the energy of accelerated ions can be enhanced if a micro-droplet is employed as a target. The average energy of fast protons is defined by the position of the peak in their energy spectrum. It has been observed that the position of the peak is practically unchanged after its formation (on 100 fs time scale), in contrast to cutoff energies of protons, which still increase in time because of the Coulomb repulsion. However, only a relatively small portion of fast protons can be found in the energy tail.

While the peak position for the cylindrical target is about 1.5 MeV, the latter for the flat foil and curved foil sections is about 600 and 450 keV, respectively. This effect can be explained as follows. The peak energy position depends on two parameters. The first one is the cutoff energy of carbon ions, which is about 400 keV per nucleon for a flat foil and a curved foil section and it is about 800 keV per nucleon for a cylinder, respectively, at the time of 200 fs after the interaction. The second parameter is the spatial density of accelerated carbon ions and protons. In the cases where the spatial density of ions is higher, the Coulomb explosion is stronger and the bunch of fast protons follows more closely the position of the most energetic carbon ions. This can be seen from pictures with density profiles shown in Fig. 4.13. The highest densities of fast protons are acquired in the case of a curved foil

section. It corresponds to the lowest difference between the cutoff energy of carbon ions and the position of the peak in the proton energy spectrum. Thus the proton bunch is compact in the energy space. On the contrary, the lowest densities of fast protons are calculated in the case of the cylinder, which corresponds to the highest difference between the cutoff energy and the position of the peak and the highest proton divergence.

Analytical estimate (2.80) gives the position of dip in proton energy spectra (which is approximately constant) for the hot electron temperature $T_h \approx 105$ keV inferred from the simulation of flat foil section about 400 keV. This value is in agreement with the simulation, see Fig. 4.11.

Concerning the proton cutoff energy, our analysis confirms the qualitative *ad hoc* model by Schreiber *et al.* [97] and shows that the most important parameter defining the cutoff energies is the potential drop $\triangle\varphi = \int_{x_0}^{x_1} E(x)\mathrm{d}x$ at the beginning of acceleration process (x_0 is the position of target rear surface, x_1 is the maximum position of hot electrons which are not escaping the rear surface potential). This parameter depends on the total absorbed laser pulse energy. However, one also has to account for the divergence of accelerated ions (e.g., for the density of ions), especially for determining the cutoff energies of carbon ions (owing to mutual interaction between carbon ions front and fast protons back).

In our case, the potential drop $\triangle\varphi$ is determined by two parameters. The first one is the absorbed laser energy; the second parameter is the effective area of the surface where the TNSA mechanism takes place (cross section of the hot electron cloud behind the target rear side).

At the beginning of acceleration process, 10.6%, 11.4% and 14.6% of the laser pulse energy is transformed into the kinetic energy of electrons for the flat, curved foil and cylindrical targets, respectively. A higher absorption of laser pulse energy in the cylinder can be explained by the presence of a curvature at the front side of a target. In this case, the laser pulse arrives on the target on larger angles giving rise for a more efficient colisionless absorption (resonance absorption, Brunel vacuum heating) and higher electron energies. In the case of a flat foil, the p-polarized laser pulse has a normal incidence on the target, the main mechanism of colisionless absorption is the $j \times B$ heating, and the average electron energy is lower.

A smaller effective surface leads to higher densities of hot electrons at the rear side of target and, thus, to higher accelerating electric fields as also discussed in the previous section. Indeed, in the case of two times wider flat foil (size $3\lambda \times 8\lambda$) with the same parameters, we obtained about 30% lower average energy of fast protons due to an undesirable spread of hot electrons which results in lower accelerating electric fields (maximum 2.8×10^{12} V/m compared to 3.5×10^{12} V/m for the flat foil of size $3\lambda\times4\lambda$). It is difficult to determine exactly the size of the effective surface because of various target shapes. However, the analysis of the value of the potential drop $\int_{x_0}^{x_1} E(x)\mathrm{d}x$ in function of the absorption rate shows that somewhat smaller effective surface should be defined for a cylindrical target.

4.2.2 Conversion efficiency and influence of initial density profile

We define the number of fast protons as the number of all protons with energies higher than the position of the dip in the energy spectrum. This definition is simple to use (the position of the dip is always well-defined) and it is justified in terms of physics because the

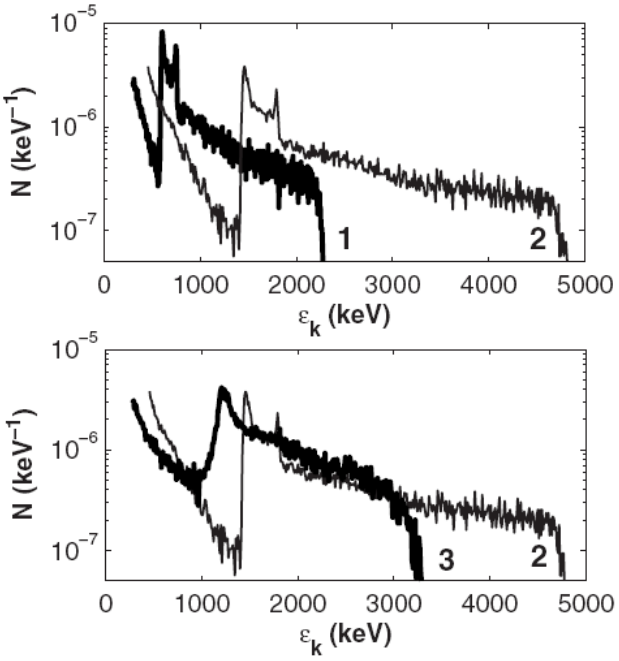

Figure 4.14: Proton energy spectra at 200 fs after the interaction for the flat foil sections with different initial density profiles at the front and rear side. Line 1, steep, steep; line 2, exp, steep; line 3, exp, exp. "Steep" stands for density scale length $L \approx 0.05\lambda$, while "exp" stands for $L \approx 0.25\lambda$.

other protons with lower energies are spatially separated by carbon ions (see Fig. 4.13). We observed that the number of fast protons remains constant from the time approximately 150 fs after the interaction. It was found that 0.35%, 0.4%, 0.5% of all protons can be regarded as fast at the rear target side for three types of targets considered (flat and curved foils, cylinder, respectively).

A relative number of fast protons can be estimated as a ratio of the number of protons in the sheath layer given by Eq. (4.1) and the total number of protons in target

$$N_{rel} \approx \Delta_p / d, \tag{4.2}$$

where d is the target thickness. For the flat foil $\Delta_p \approx 5\ \mathrm{nm}$ and, thus, $N_{rel} \approx 0.2\%$, according to Eq. (4.2). This is in a reasonable agreement with the simulation result (0.35%). The difference of less than two times can be explained by the effect of ion expansion. According to Eq. (4.1), a lower cold electron density results in a larger thickness of the sheath Δ_p and, thus, to a larger number of protons N_{rel}.

Our simulations were stopped 300 fs after the laser-target interaction. At this moment, the laser energy transformation into the proton kinetic energy was 2.8%, 3.0%, and 3.8% for three types of targets considered. Approximately a quarter of this energy, that is, 0.8%, 0.8%, and 1.05% of the laser energy, was transformed into the energy of fast protons at the rear target side. These numbers can be compared with the efficiency of carbon acceleration: 3.6%, 3.9%, and 6.7% of the laser energy was transformed into the kinetic energy of carbon ions for flat and curved foil sections and the cylindrical target. The laser absorption

was 15.8% for the cylindrical target and only 11.6% and 12.4% for the flat and curved foil sections, respectively.

The absorption efficiency and the proton energy spectrum can be controlled by a target density profile. The step-like profile was assumed at the onset of previous simulations. However, the target starts to expand due to a nonzero initial temperature, and the density scale length on both target sides is approximately $L \approx 0.05\lambda$ at the time of laser target interaction. Such a density profile is labeled as "steep" in Fig. 4.14, where the impact of plasma density profile on the fast ion spectrum is demonstrated for the flat foil section. For the simulation initiated with the exponential profile on the front side of the target with the density scale length $L = 0.2\lambda$ ($L \approx 0.25\lambda$ during the laser target interaction), see Fig. 4.9, the laser absorption is increased to 26% and the energy of fast protons is enhanced by more than two times. The laser energy transformation to fast protons rises to 1.95% at the target rear side, while the number of fast protons does not increase significantly (from 0.35% to 0.45%). In the run where the same exponential profile is assumed also at the target rear side, the fast proton number is slightly enhanced (0.55%), but the energy of fast protons is reduced because the accelerating electric field at the rear side of the target decreases (see Fig. 4.15). The laser transformation efficiency to fast protons (1.9%) is almost the same as in the previous case.

These numerical results are in agreement with the experimental data obtained in Ref. [100] where the influence of the laser prepulse on the ion acceleration has been investigated. In this experiment the rear-side plasma was formed by a shock wave created by the laser prepulse and reflected from the rear surface of a thin target.

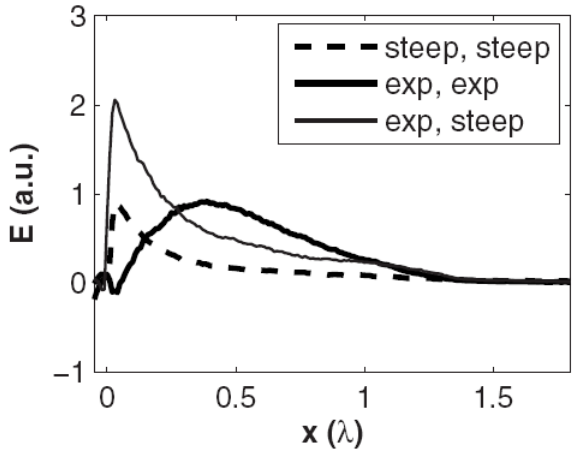

Figure 4.15: Electric field on-axis profiles at the rear side of flat foil sections with the same parameters except for their different initial density profiles at the beginning of ion acceleration. The position x=0 corresponds to the initial rear boundary of overdense plasma with a constant maximum density of particles (the rear-side plasma with the scale length $L \approx 0.25$ is located in the interval $x = 0 - \lambda$). 1 a.u. corresponds to the electric field of 4×10^{12} V/m.

Fig. 4.16 shows the phase space of protons at the rear side of three targets with two different scale lenghts at the front and rear sides. The ions evolve slower in the case of the target with a longer rear-side plasma scale length. Figure 4.15 demonstrates that ions are accelerated by a smaller electric field compared to the target with a shorter rear-side

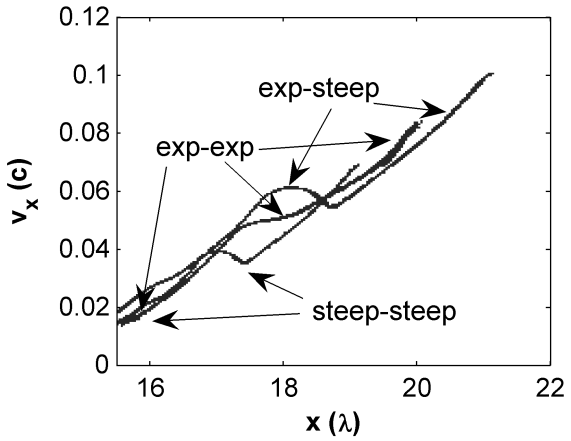

Figure 4.16: Phase spaces (x, v_x) of protons beyond the rear side of foil sections with various density profiles at 200 fs after the interaction. The target is initially located between 12λ and 15λ.

gradient length, but they are accelerated on a longer track. Because of the initial spread of ions at lower densities and a much lower gradient of accelerating electric field, the spatial separation of protons and carbon ions develops slower and carbon ions do not shield the accelerating electric field so rapidly compared to the cases with a steep density profile at the target rear side. Because of that, the protons from deeper layers of the target can be also strongly accelerated before the time when carbon ions inhibit the acceleration process. This is the reason for a higher number of fast protons in the case of a longer rear-side plasma density profile.

4.2.3 Angular divergence of fast protons

A quality of fast proton beam is characterized by the number of particles and the beam divergence. The latter is controlled by the shape of the rear side target surface. The angular distribution of fast protons at the rear side of target is presented in Fig. 4.17 for various target shapes at the time of 300 fs after the interaction. The divergence of fast protons is about 15° for a flat foil. It corresponds to experimental data measured in Ref. [94]. In the case of cylindrical target, the protons angular distribution is very broad and the anisotropy is relatively small: the fast protons angular density in the direction of incident laser beam (angle 0°) is 2.5 times higher than that in the opposite direction (angle 180°). On the contrary, a very narrow angular distribution is observed for the curved foil section. The proton and the carbon ion density on the axis achieves its maximum at the distance 4λ from the target due to ion focusing induced by the concave rear side shape.

The ions focusing distance of about 4λ is equal to the foil rear side curvature radius. The width of the focused proton beam is estimated 2λ, compared to 5λ for the flat foil at the same distance from the rear surface of the target. After reaching their focal spot, the protons are spread due to the effect of Coulomb repulsion similarly to the case of the flat foil. However, the proton density in the focus is relatively low due to their lateral spreading and consequently the repulsion is weak. According to our simulation results for the curved

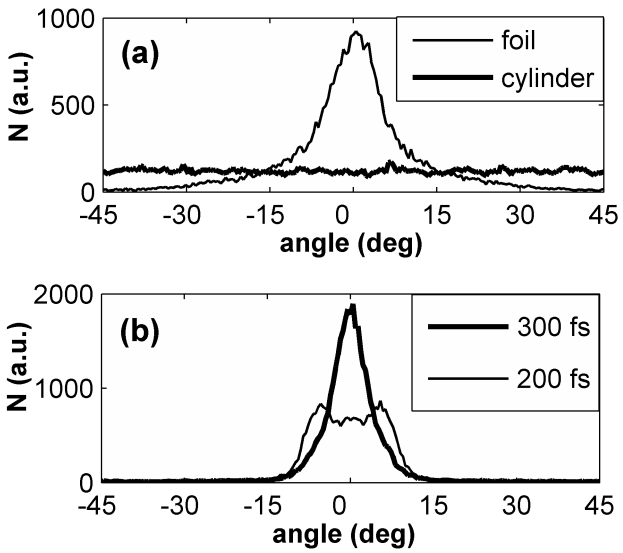

Figure 4.17: Angular distribution of fast protons for three different target shapes at the distances $3 - 8$ μm from the target: a) angular distribution for the flat foil and the cylinder at the time of 300 fs after interaction; b) angular distribution for the curved foil at 200 fs and 300 fs after interaction.

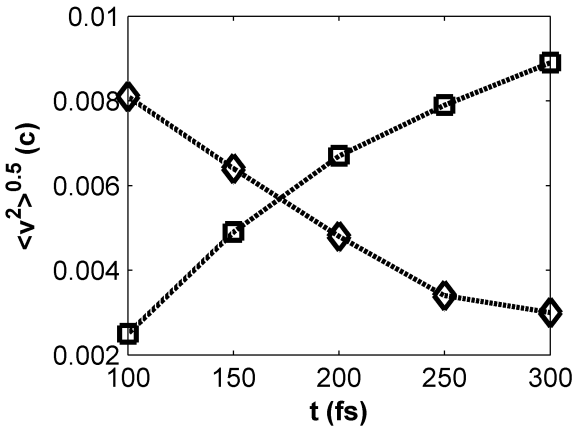

Figure 4.18: Temporal evolution of the root mean square transverse velocity of fast protons for the flat foil section (squares) and the concave section (diamonds).

foil, the average density of fast protons is approximately $0.08n_c$ in the focal spot at the time of 300 fs. This can be compared with the flat foil, where the same density is reached at the distance of about 2λ from the target rear surface at 150 fs after the interaction.

Figure 4.18 shows the time dependence of the root mean square (rms) transverse velocity of all fast protons for the flat and curved foils. The rms transverse velocity is defined as

follows

$$\sqrt{< {v_t}^2 >} = \sqrt{\sum_{i=1}^{N} \frac{(v_y)_i^2}{N}}, \tag{4.3}$$

where $(v_y)_i$ is the velocity of *i-th* proton in the transverse direction and N is the total number of fast protons. In the case of the flat foil section the proton rms velocity is $0.002c$, and it increases with time. The decrease of velocity spread with time for the concave target corresponds to the proton beam focusing. At the time of 300 fs, when the fast protons are reaching their focal spot, the rms transverse velocity of $0.0029c$ is corresponding to the transverse proton temperature 4.5 keV. Later on, the beam is defocused, nevertheless the angle of divergence is lower than in the case of flat foil. The defocusing of proton beam occurs more rapidly in the beginning of the acceleration process because of a higher space charge densities leading to a higher acceleration of protons in the transverse direction. As time goes on, the proton beam spreads in the longitudinal direction and space charge densities decrease even in the case of curved foil (where the proton beam is initially focused in the transverse direction).

4.3 Enhanced laser-driven proton acceleration from thin foil sections

We have demonstrated above that the employment of targets with limited transverse dimensions enhances the energy of accelerated ions. In our numerical simulations, the most efficient acceleration takes place if the laser beam width is equal to the target width. However, the laser beam has to be focused very precisely to the target center which is not easy under real experimental conditions together with a more complicated process of target fabrication and its positioning. This is possible to overcome by using targets produced directly in the focal spot such as the chain of water microdroplets [19]-[24]. On the other hand, this approach has its limits in reproducibility, because of a certain probability of the interaction of the pulse with injected microdroplets.

Measurements of the hot electron spatial distribution (on large mm size) showed that the accelerating sheath extends over a relatively large area (typically $\sim 100 - 200$ μm in radius) at the rear side of the target [93], [135]. By limiting the transverse size of the target below this size, one can hope to confine the electrons laterally and enhance the efficiency of ion acceleration such as in cases studied previously.

In this section, there are, firstly, presented experimental results obtained at LULI laser facility in France, which demonstrate an increase of the maximum proton energy and the laser-to-proton conversion efficiency, as well as a reduced proton beam divergence, with decreasing the transverse foil dimensions. Secondly, we have explained these results by the mechanism of refluxing of hot electrons, which takes place during the ion acceleration time and produces effective (time-integrated) denser and hotter electron population if the transverse dimension of the target is small enough.

4.3.1 Experimental results

The experiments were performed using the 100 TW laser at LULI operating in the Chirped Pulse Amplification regime. The main laser pulse was compressed to a temporal duration of $\tau_L = 350$ fs, then frequency-doubled and filtered at $\lambda = 529$ nm in order to enhance its temporal contrast. Frequency conversion was used to avoid preplasma leakage from the front to the rear surface of the limited mass targets used in the experiment (2 μm thick Au foils supported by an insulated glass stalk [136]). The laser was focused at the target center at $45°$ incidence on the front surface of the target to a FWHM of ~ 6 μm. The laser energy in the focal spot was $\varepsilon_L \sim 7$ J, which led to a peak intensity on the target of $I \sim 4 \times 10^{19}$ W/cm^2. A wave front correction is applied before every shot. As sketched in Fig. 4.19, the targets had constant thickness, but a variable surface area. The profile and spectrum of the proton

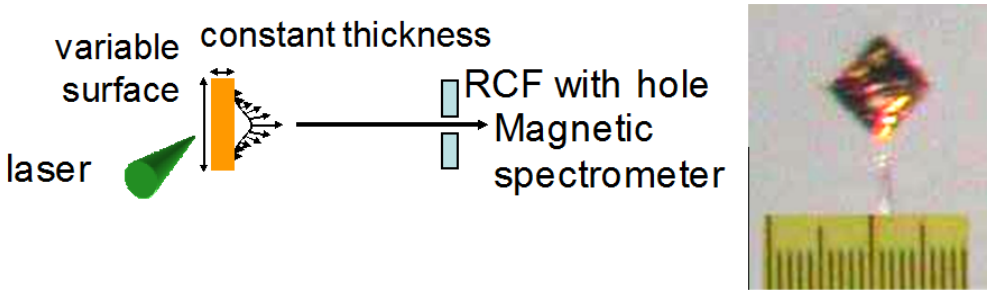

Figure 4.19: Set-up of the experiment: laser pulse of intensity $I \approx 4 \times 10^{19}$ W/cm^2 and of duration $\tau_L = 350$ fs is incident on 2 μm thick Au foil at the angle of $45°$. On the right: an example of the foil section supported by an insulated glass stalk in the experiment.

beam accelerated from the targets was monitored using a combination of dosimetric film (RCF) stacks (having a central, millimeter-sized hole) [137] and a magnetic spectrometer [138], located 70 cm away from the target (see Fig. 4.19). The latter used imaging plates (BAS SR-2025 from Fuji Photo Film Co. Ltd) to detect the protons [138]; they were read with a BAS-1800II scanner. RCF are preferentially sensitive to penetrating protons, which have a large specific energy-loss and produce a high contrast image. The RCF stacks yield a coarse resolution in energy (determined using SRIM [139]) but can monitor the transverse beam profile.

Fig. 4.20a shows the measured maximum proton energy ε_{max} as a function of the target surface area. One can clearly observe an increase of ε_{max} when reducing the target surface area, nearly tripling the peak proton energy in the case of the smallest targets. Fig. 4.20b shows that the energy conversion efficiency from laser to proton (integrated over the proton spectrum from 1.5 MeV to the maximum energy) also increases when reducing the target surface (the conversion efficiency is improved more than about one order of magnitude for the smallest targets).

In order to estimate the effective hot electron density and temperature in the accelerating sheath for various target surface area, we fit the proton spectra (i.e., the number of accelerated protons per unit energy ε) using $dN/d\varepsilon = 1.3N_h/(2\varepsilon T_h)^{1/2} \exp\left[-(2\varepsilon/T_h)^{1/2}\right]$ according to (2.73). Note that this fit corresponds to a 1D picture assuming a time-integrated, homogeneous electron population over the sheath with a temperature T_h and an effective number of

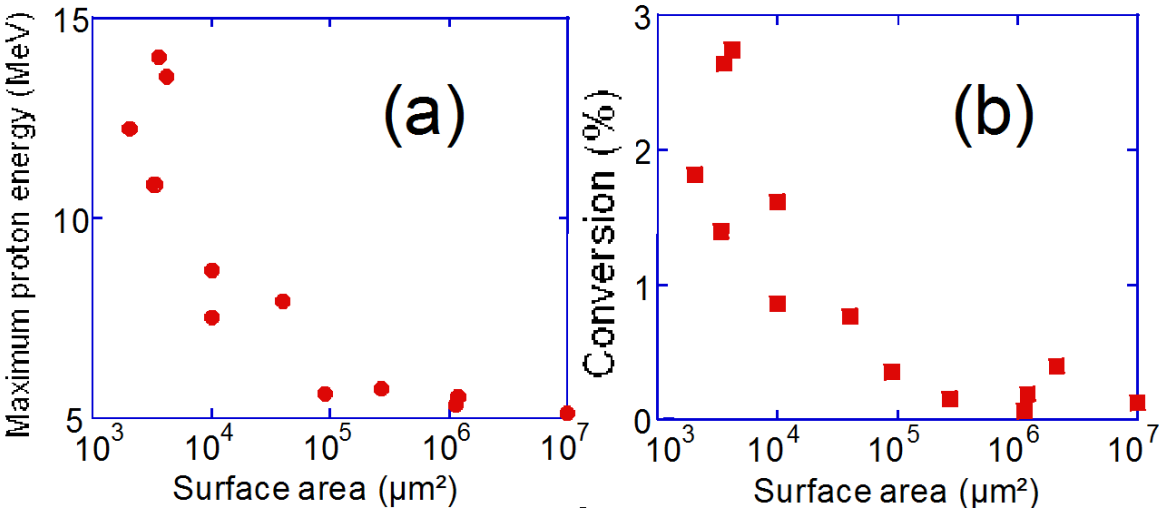

Figure 4.20: (a) Maximum proton energy (extracted from RCF stacks) for Au 2 μm thick foil sections of various surface area. (b) Laser-to-proton energy conversion efficiency (for protons with energy higher than 1.5 MeV) for the same targets.

electrons in the sheath N_h. Fig. 4.21 shows these inferred parameters for 2 μm thick Au targets having various surface area and temperatures consistent with simulations of sharp-interface plasmas irradiated at 45° [140]. Both parameters increase, indicating the enhanced effective electron temperature and number when reducing the target dimensions, contributing to the improvement of proton beam characteristics.

For smaller targets, the proton flux is not only higher but also is more collimated. This is shown in Fig. 4.22a, which displays proton beam angular profiles (corresponding to a beam slice at $\sim 60\%$ of the maximum proton energy) as collected on RCF films. Two cases are shown: medium-size and small-size Au targets, both 2 μm thick. In both cases, the beam is centered on the target surface normal (see the inset). It is clear that smaller targets present an increase in beam collimation: the central part of the dose is more peaked, although there is a fraction of the dose spread at large angles, likely due to emission from the target edges. Using the information given by the angular distribution of the beams, we can deduce that the accelerating sheath is more uniform in small targets. In order to demonstrate this assumption, we first plot (see Fig. 4.22b) the evolution of the angular FWHM of the proton dose (as can be retrieved from profiles such of shown in Fig. 4.22a) for all proton energies within the beam. The decrease of the angular opening of the proton beam with energy is a standard observation. It is determined by the curvature of the bell–shaped accelerating electron sheath [75], [141] : the particles with higher energies, originating from the tip of the sheath, are emitted at small angles, while the particles with lower energies, originating from the wings of the sheath, are emitted at large angles. In our case, the observed dependence of the angular opening of the proton beam for transversally large or medium-size targets is consistent with previous measurements [142] made with laterally large targets. However, for smaller targets, the variation of the angular FWHM with the proton energy is greatly reduced, suggesting a flatter electron sheath. This is consistent with the picture of geometrically confined electrons, which then produce a more uniform sheath over the target surface.

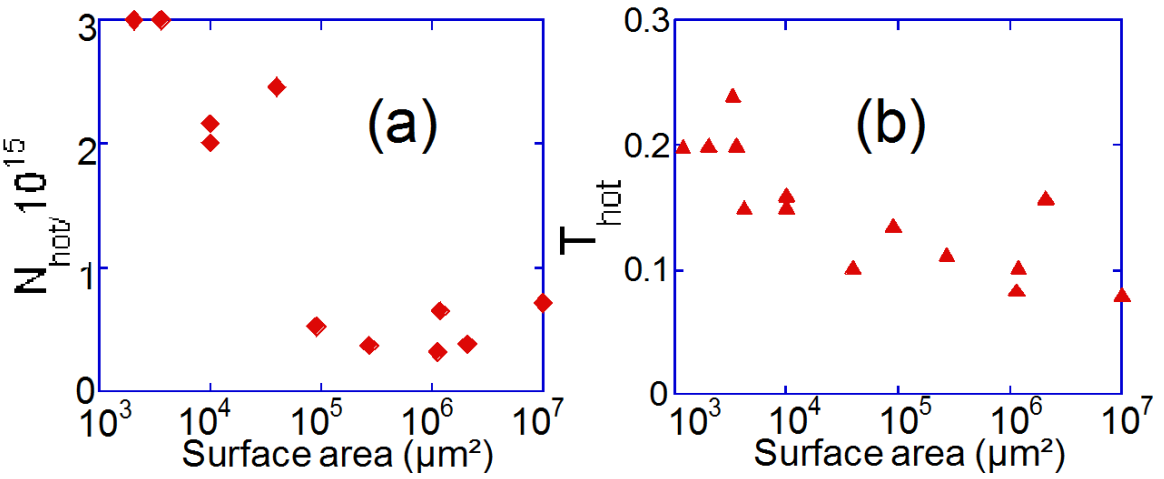

Figure 4.21: Inferred (a) effective number of hot electrons in the accelerating sheath N_h and (b) effective hot electron temperature T_h (in MeV) for Au foil sections (see text for details).

4.3.2 Our theoretical interpretation of the results

To clarify the mechanism of the observed enhancement in the time-integrated properties of the electron and ion beams when reducing the target surface, we performed two-dimensional (2D) particle-in-cell (PIC) simulations of laser target interactions with our code. As present-day computational limitations do not allow treating simulation boxes of several hundred microns across, the laser and target parameters were rescaled in such a way that the key ratio of the target transverse size (D_s) to the laser pulse length $c\tau_L$ (where τ_L is the pulse duration) was kept the same as in experiment. We used ratios $D_s/(c\tau_L)$ of 0.6 and 2.4 to be respectively representative of "small" (50×80 μm^2) and "medium" (200×300 μm^2) foils in the experiment. In our simulations, a "small" foil has the transverse size of 12 μm (20λ) and a "medium" foil of 48 μm (80λ). Both foils have the same thickness of 1.2 μm (2λ). The laser pulse duration is set to 80 fs (40 laser cycles), the laser wavelength $\lambda = 600$ nm. The temporal laser pulse profile has a trapezoidal shape with a constant maximum intensity $I = 2.4 \times 10^{19}$ W/cm^2 ($a_0 = 2.5$) of a duration of 60 fs and two linear ramps of a duration 10 fs at the beginning and at the end of the pulse. The p-polarized laser beam has a supergaussian profile (n=3) with the beam width (FWHM) 4 μm (7λ) and the incidence angle is 45°. Targets are composed of protons and electrons with a step-like density profile of $n_e = 20n_{crit}$ and an initial temperature of 2 keV. Simulation boxes are $76\lambda \times 76\lambda$ and 2λ thick absorption layers are added behind each side of the box. The electrons that reach the simulation box boundaries are frozen there. The cell size is set to 12 nm. The collisions are neglected in these simulations since they cannot significantly affect the transport of MeV electrons relevant to our case as discussed in Chapter 2. The simulation run terminates at the time of $2.5\tau_L$ (200 fs) after the laser hits the foil, at the moment when temporal changes in ion cutoff energy are below 0.025 MeV/fs and they have a decreasing tendency (the acceleration of ions is terminated).

The simulations show that the time-integrated (over the ion acceleration duration) hot electron spectra measured at the target center display higher temperatures and higher numbers for the small foil. This is due to transverse refluxing, schematically displayed in Fig. 4.23,

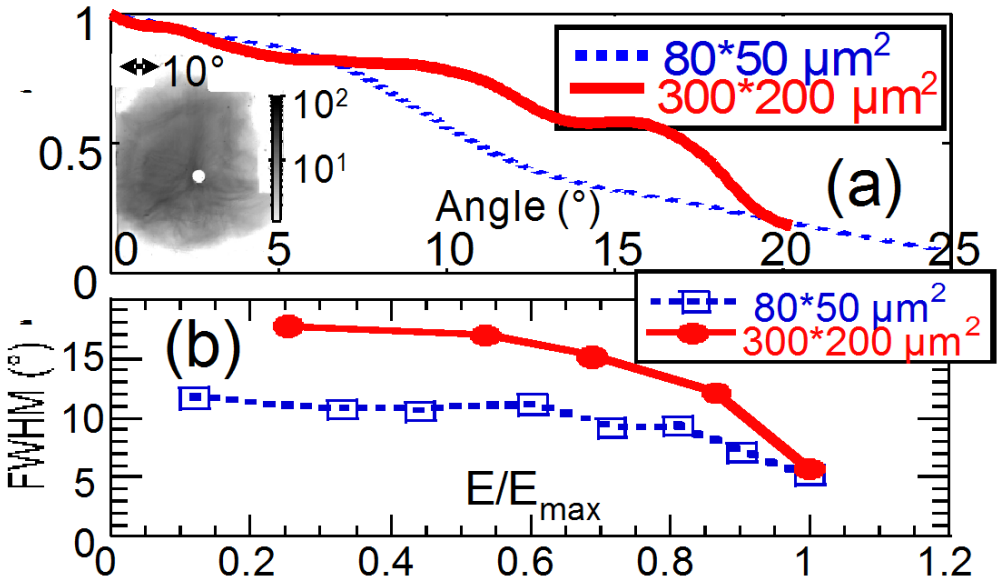

Figure 4.22: (a) Azimuthally averaged angular proton dose profiles extracted from films and corresponding to $\varepsilon \approx \varepsilon_{max}$ for medium and small 2 μm thick Au targets, showing that the dose is more peaked for the small target. The inset shows the corresponding film for 300×200 μm^2 target. The gray scale is in units of Gy. (b) FWHM of angular transverse profiles such as the ones of (a) for all proton energies and for the same two targets.

in which hot electrons are reflected back from the small foil edges towards the target center and overlap there. This creates an effectively denser and hotter sheath while the protons are accelerated. The larger the target, the longer it will take for the electrons to be reflected, thus restricting the enhancement. This is shown in Fig. 4.24 where the temporal evolutions of electron energy spectra beyond the focal spot are displayed for the small (a) and medium (b) foils. Only electrons with energies higher than 100 keV and in a central strip that is 10λ wide are considered.

When the laser pulse duration $\tau_L >> D_s/c$ (where D_s is the transverse foil size and c is the velocity of light in free space, i.e., maximum velocity of hot electrons in longitudinal direction to the foil surface), hot electrons from the foil edges mix with newly heated electrons by still interacting laser pulse. In the case of small foil (Fig. 4.24a), $\tau_L \approx 2D_s/c$, and one can see an enhancement of hot electron density (from time instant $1.0\tau_L$), whereas in the case of larger foil (Fig. 4.24b), $\tau_L \approx (1/2)D_s/c$, and the first electrons reflected from the foil edges reach the interaction zone at the time of about $2.5\tau_L$, at the moment when the acceleration process has already almost terminated (the laser pulse interacts with the foil from 0 to τ_L in both cases). This leads to smaller hot electron temperatures averaged over the ion acceleration time. If the temperatures are averaged over simulation (i.e., acceleration) time (from $0.5\tau_L$ to $3.5\tau_L$), we obtain effective temperature 0.67 MeV for the small-size and 0.59 MeV for the medium-size foil, which means that the difference is about 15%. Also averaged hot electron densities are different - the density is 2.3 times higher in the central part of the small foil, while the absorption of the laser pulse energy is the same for both cases - about 45%.

We estimate the velocity of the transverse sheath spread along the foil surface about

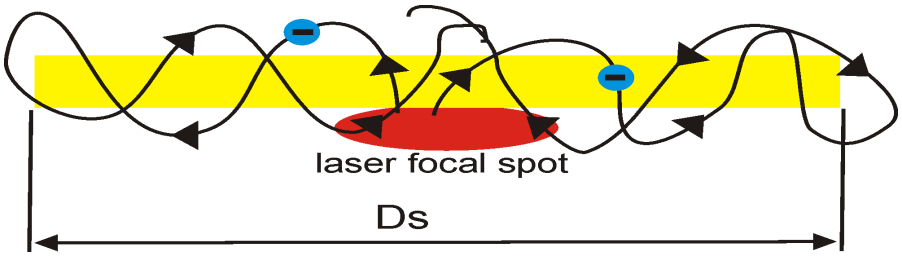

Figure 4.23: Scheme of the transverse refluxing of hot electrons in a thin foil section: Electrons heated at the focal spot recirculate in the foil forth and back and go towards foil edges as their motion is restricted in perpendicular direction to the foil surface, but not in parallel direction to the surface until they will reach the edges. At the foil edges, the electrons are reflected back, and, consequently, they enhance accelerating field in the sheath.

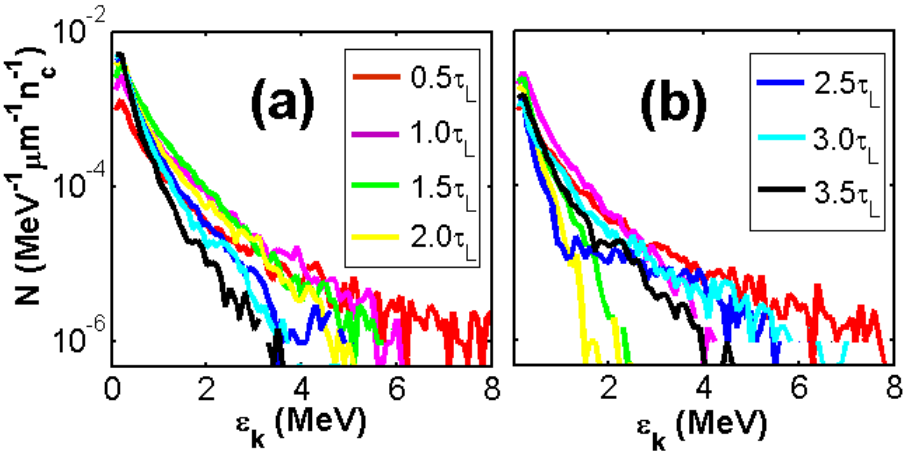

Figure 4.24: Simulated energy spectra of electrons beyond the laser focal spot in several time moments for the cases of (a) small and (b) medium foils. Only electrons in a central strip 10λ wide are considered.

$(2/3)c$ in the simulations. This value agrees well with the electric field expansion velocity of 0.2 μm/fs predicted theoretically [145] and with the experimental measurement of the sheath lateral dimensions after irradiation by a 400 fs laser pulse of mm-size targets [93]. We stress that the important point is whether the hot electrons return to the target center during the acceleration time of protons, which is about $2.5\tau_L$ in our case, 2.5 times longer than the laser pulse duration. For too large targets (over 5×10^4 μm^2 in the experiment), the electrons do not come back in time during the acceleration, which explains why the maximum proton energy does not vary with increasing foil surface (see Fig. 4.20). The hot electron recirculation from the target edges for the small foil also explains the narrower angular ion spread as the electron sheath is more homogeneous along the target surface.

The simulation results agree well with proton cutoff energies measured in the experiment: 12 MeV for the small-size and 10 MeV for the medium-size foil. However, the enhancement of the laser-to-ion conversion efficiency found in the simulations (5.5% for a small vs. 3.5% for a medium foil) is smaller than seen in the experiments. This can be explained by the

fact that the electrons cannot spread in the third spatial dimension in our 2D simulations. The conversion efficiency (2.75) calculated from the total ion energy (2.74) is proportional to the product $T_h n_h$, and therefore is very sensitive to the electron density. On the contrary, the maximum ion energy (2.72) depends on T_h, and it is a much weaker function of the hot electron density n_h.

We performed a preliminary 3D simulation with the code PICLS [85] to check this assertion. In those simulations, the interaction parameters were further scaled down to ensure a reasonable computation time. The laser pulse duration and the beam width were set up two times smaller compared with 2D simulations. Two foil sections were considered with target dimensions $10\lambda \times 10\lambda \times 2\lambda$ (small-size foil) and $30\lambda \times 30\lambda \times 2\lambda$ (medium-size foil) and the laser pulse was incident normally on the target in this set of simulations (the intensity was kept the same as in the 2D case). While calculated maximum proton energies are about 4 MeV in both cases (they differ about 10% between small-size and medium-size targets), the energy conversion efficiency differs about almost one order of magnitude. Thus, the obtained results support the conclusion that 2D simulations can predict well the maximum ion energy, but they strongly overestimate the conversion efficiency for large targets.

4.4 Conclusion

We analyzed here the interaction of femtosecond laser pulses with mass-limited targets of various shapes and compositions, presented experimental results on enhanced ion acceleration in thin foils of reduced surface and our theoretical interpretation of the experimental measurements, all with the help of our two-dimensional particle-in-cell code. The particularity of mass-limited targets is in their ability to limit the accelerating sheath spread created by hot electrons due to reduced target dimensions. That leads to a more efficient transformation of absorbed laser energy to the energy of accelerated ions and to a higher maximum ion energy.

Considering hydrogen plasma targets of various shapes but the same thickness, we demonstrated by numerical simulations that the optimum transverse target size is about the laser beam diameter. For ultrashort intense laser pulses (of duration of only several laser periods) and target densities at the margin of relativistic transparency, we found twice higher maximum proton energy for a droplet target compared to the standard thin foil target. In this case, fast electron bunches produced during laser-target interaction propagate through the target and may generate dipole radiation in transverse direction as they oscillate forth and back, in addition to the ordinary scattering of the laser wave. To obtain the highest possible energy of accelerated ions, a circular target shape is preferred to the rectangular form. On the other hand, the employment of cylindrical targets produces an undesirable divergence of the fast ions, which leads to their lower densities. From this point of view, a concave foil section could be an ideal target as its employment enhances the absorbed laser energy due to the front surface curvature and allows one, simultaneously, to focus the proton beam at a specific distance determined by the radius of curvature at the rear side of the target and to decrease its divergence afterwards. It was also shown that the laser absorption (and, thus, energy characteristics of fast ions) can be theoretically increased by the presence of preplasma. However, the preplasma created by laser prepulse is usually accompanied by the formation

of an exponential density profile of the rear-side plasma, which can destroy the acceleration process ascribed to the TNSA mechanism broadly discussed in Chapter 2.

We also demonstrated the possibility of controlling the ion energy spectra in multispecies mass-limited targets composed of protons and carbon ions (there, the target transverse size has to be comparable with the laser beam width to ensure an uniform accelerating electric field in the sheath). Initially, a thin layer of protons (of the thickness about $\sim 10\ \mathrm{nm}$) is accelerated, whereas carbon ions are accelerated somewhat later because of their inertia. The presence of carbon ions serving as a piston compensates partially for the effect of Coulomb explosion of the fastest protons originated from the thin surface layer and maintains a narrow proton energy spectrum for a long time. In our simulations (laser intensity $\sim 5 \times 10^{19}\ \mathrm{W/cm^2}$, pulse duration 30 fs, laser beam width $\sim 3\lambda$ comparable with all target dimensions), the conversion efficiency of laser pulse energy into those fastest protons is about 1% and their average energy varies from $\sim 1\ \mathrm{MeV}$ to $\sim 2\ \mathrm{MeV}$ depending on the target shape.

Finally, previously presented theoretical and numerical results have been confirmed in the recent experiment with thin foil sections of a reduced surface [35]. In this case, transverse target sizes are at least ten times larger than the laser beam width, but still sufficiently small to observe the effect of increase of the ion energy and number with a decreasing foil surface. In this experiment, $2\ \mu\mathrm{m}$ thick Au foil sections of a variable surface area are irradiated at the incidence angle of 45° by p-polarized laser pulse of intensity $\sim 4 \times 10^{19}\ \mathrm{W/cm^2}$ and of duration $\sim 350\ \mathrm{fs}$. The maximum proton energy and laser-to-proton conversion efficiency stay approximately constant for larger surface areas, i.e., $\sim 5\ \mathrm{MeV}$ and $\sim 0.2\%$, respectively. However, when the surface area is smaller than $\sim 5 \times 10^5\ \mu\mathrm{m}^2$, the maximum energy and the conversion efficiency increase linearly with the decreasing foil surface up to $\sim 14\ \mathrm{MeV}$ and $\sim 3\%$, respectively, for the smallest target (of the surface area about $3 \times 10^3\ \mu\mathrm{m}^2$). An observed dose increase is very promising for applications such as proton-isochoric heating of matter [143], or radioisotope production [144], where the laser-to-proton yield is the appropriate figure of merit.

We have contributed by the theoretical explanations of this improvement in energy characteristics. The enhancement of proton energy is due to the refluxing of hot electrons laterally from the target edges towards the center, which takes place during the ion acceleration time, if the transverse dimension of the target is small enough. The refluxing produces effective (time-integrated) denser and hotter electron population as can be seen not only in our simulations, but also from values of hot electron density and temperature inferred in the experiment. For the smallest target surface, the hot electron sheath is more homogeneous along the target surface, which explains the narrower ion angular spread. Two-dimensional PIC simulations reproduce quite well the dependence of maximum proton energy on the transverse target dimension, but they fail in the calculation of the conversion efficiency. To evaluate more accurately numerically the dependence of the conversion efficiency on the transverse target dimensions, time consuming 3D simulations are necessary.

We should note that our theoretical results on mass-limited targets have initiated an interest and discussions in the scientific community, which has led to an article recently published by another group in Ref. [146]. This paper investigates experimentally and numerically (by 3D PIC code [124]) proton acceleration from a polymethylmethacrylate (PMMA) sphere of

$15\ \mu\mathrm{m}$ in diameter mounted on a sub-$\mu\mathrm{m}$ thin glass capillary irradiated by the femtosecond laser pulse of an intensity $\sim\ 10^{20}\ \mathrm{W/cm^2}$ and of a duration $\sim\ 45\ \mathrm{fs}$ in comparison with the acceleration from $20\ \mu\mathrm{m}$ thick plastic foil. Here, the experiment confirms that the ions originated from the spherical target have higher maximum energies. However, the proton beam is highly directed in the laser propagation direction, in contrast to our 2D PIC simulation results [27], [147] and several experiments for lower laser intensities, slightly above $\sim 10^{18}\ \mathrm{W/cm^2}$, [19], [20], where the protons are accelerated almost isotropically.

3D PIC simulations presented in Ref. [146] demonstrate that this proton beam arises from acceleration in a converging shock launched by the laser at the target front. Protons accelerated in this shock induced by the ponderomotive force can reach energies well in excess of the values observed in the TNSA regime under identical laser conditions, showing a plateau-shaped spectrum as predicted in Ref. [148]. In those simulations for the foil target, the flux of the ions emitted from the rear surface (by the TNSA) exceeds the one of the front accelerated ions by a factor of 10. In the case of the sphere the result is inverted, the proton beam from the front is about 50 times as intense as the beam of surface ions emitted into the solid angle of 4π. This enormous difference in particle flux for protons originating from the two different sources, i.e., target front and back side, were not observed in 2D PIC simulations which were performed for comparison. This shows the necessity of taking into account the full three-dimensional geometry, when describing the interaction of the laser with a spherical target.

Chapter 5

Laser proton acceleration in a water spray target

In targets with dimensions comparable or larger than the laser spot size, a relatively small fraction of target ions is usually accelerated by the TNSA mechanism. Here, the Coulomb explosion of ions is strongly reduced due to the neutralization by electrons. On the contrary, ions in sub-wavelength-sized targets are subjected to the ambipolar expansion together with the Coulomb explosion, which leads to a different character of the energy distribution function of the accelerated ions as discussed at the end of Chapter 2.

This chapter includes experimental results on proton acceleration in spray targets and theoretical analysis of femtosecond laser pulse interaction with a droplet of a sub-wavelength diameter. This provides a basis for the explanation of proton energy spectra originated from a more complex water spray target. It is shown that the spray targets, which consist of water droplets with a diameter a few tenths of the laser wavelength, could be a good candidate for efficient laser energy transfer to the target and thereby for particle acceleration.

5.1 Experiments

The experiments were carried out at Max Born Institute in Berlin, Germany. The water spray targets [149] were developed firstly to demonstrate a relatively high x-ray emission compared to a single droplet source irradiated by a femtosecond laser pulse [150]. With increasing the laser pulse contrast and with variations in the central position of the laser focus, interesting differences were observed in the proton energy spectra, which are discussed in this Chapter.

5.1.1 Experimental setup

The experiments have been realized with 35 fs Ti:Sa laser generated pulses with energies up to 700 mJ. Focused with a f/2.5 off-axis parabolic mirror, the intensities of 2×10^{19} $\mathrm{W/cm^2}$ have been achieved in a focal area with a diameter of 6 $\mu\mathrm{m}$. The temporal contrast of the laser pulse was characterized by a scanning third-order cross-correlator with a dynamic range of 10^{10}, a resolution of 150 fs, and a scanning range of ± 200 ps. The pulse

shape several nanoseconds before the main pulse was controlled by a fast photodiode with the temporal resolution of 300 ps. It is worth noting that the Ti:Sa laser has, in contrast to the most other comparable bigger systems, no regenerative amplifier in the front end part (in order to prevent from the beginning prepulses as consequence of the leakage of the Pockels cell). A prepulse-free multipass amplifier has been used, and the amplified spontaneous emission (ASE) pedestal was growing from zero to the level of $\sim 10^{-7}$ relative to the peak intensity. The measured duration was about 10 ns. In the experiments, the Pockels cells were triggered about 5 ns before the laser pulse peak. Thus, the ASE level was the same 2–3 ns before the main pulse as at 100 ps before the main pulse. In typical operation conditions, the ASE pedestal of the laser pulse, several tens of picoseconds before the pulse peak, was at a level of about 10^{-7} relative to the peak intensity.

The water spray nozzle was characterized in Ref. [150]. The number of droplets near the nozzle exit was $10^{11}\ \mathrm{cm}^{-3}$, the droplet diameter was $(150 \pm 10)\ \mathrm{nm}$, and the jet diameter was 1 mm. The droplets contained a liquid water with a mass density $\sim 1\ \mathrm{g/cc}$ and the mean atomic density near the nozzle was more than $10^{18}\ \mathrm{cm}^{-3}$. The laser was focused 1 mm below the jet nozzle outlet and the total number of droplets in the focal volume was ~ 1000. Three identical Thomson parabola spectrometers with a magnetic field of about 0.27 T and electric fields of 2 kV/cm were positioned at observation angles of 0° (laser propagation direction), 45° and 135° for measurements of ions spectral distributions. The spectrometers entrance pinholes with a diameter of $200\ \mu\mathrm{m}$ were placed at a distance of 35 cm from the source. The fast ions were detected with microchannel plates coupled to a phosphorous screen. The latter was imaged with a cooled CCD camera. The single-particle response of this detection system was evaluated with alpha-particle emission from an Am^{241} source.

5.1.2 Experimental results

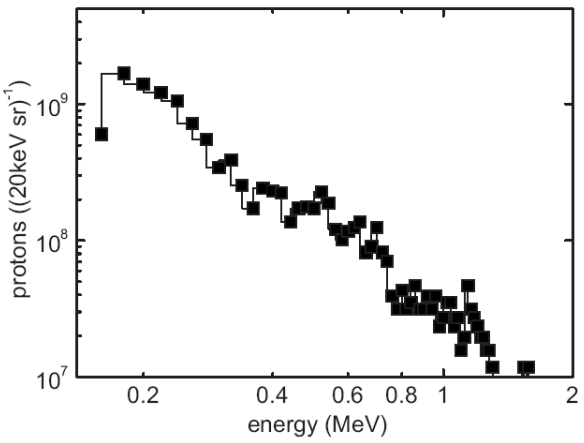

Figure 5.1: Spectrum of accelerated protons from laser-exposed water submicrometer droplets in the case of laser intensity contrast improvement up to the level of about 10^8. The improved contrast condition led to a reduction of laser output pulse energy from 700 mJ up to 550 mJ; however, the protons were accelerated up to 1.5 MeV energy.

The spatial distribution of ion emission from the spray being relatively isotropic was

more pronounced in the laser propagation direction. The laser pulse contrast has a profound effect on the performance of acceleration process in the spray target. Observations show that within the fluctuation of the laser pulse contrast by a factor of 3, the proton energy changes from "no signal" (the low energy limit of the spectrometer is 200 keV) up to (1-1.5) MeV. The contrast improvement up to the level of about 10^8, which led to a reduction of output laser pulse energy up to 550 mJ, increases accelerated protons energies up to 1.5 MeV. An example of proton energy spectra is shown in Fig. 5.1. To our knowledge, no energetic ions have been observed in the direction of laser propagation so far from gas or cluster targets.

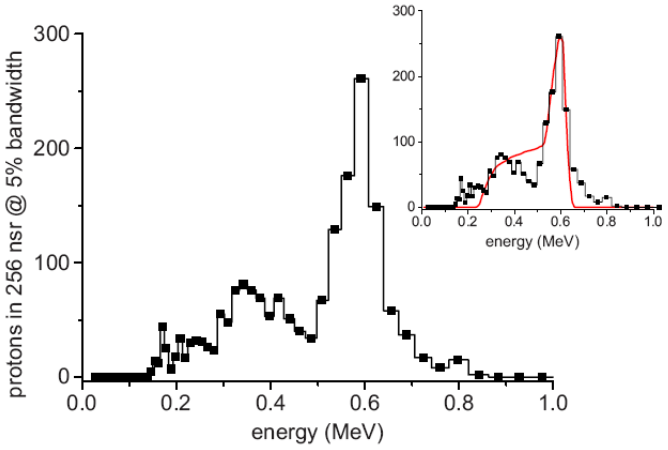

Figure 5.2: Proton energy spectrum with a narrow peak close to the cutoff measured at laser focus position closer to the rear side of the jet less than 0.25 mm. The insert shows the calculated proton energy distribution function from a single water droplet.

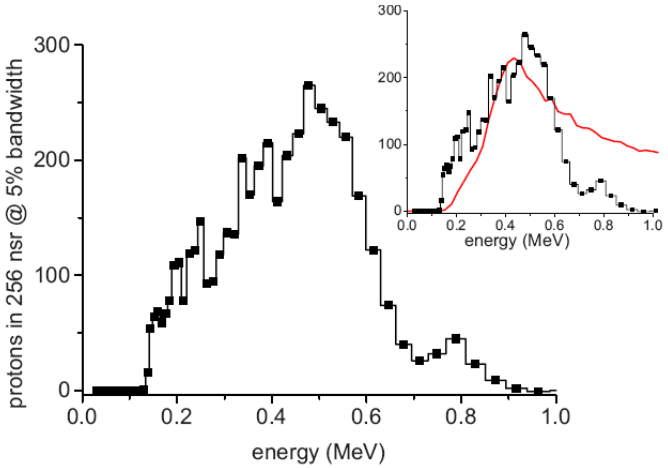

Figure 5.3: Proton spectrum with a broad maximum in the whole spectral range measured at the laser focus position closer to central region of about ± 0.25 mm of the jet. The calculated averaged proton energy distribution function from a spray of water droplets is shown in inset.

In addition to broad energy spectra shown in Fig. 5.1, in some laser shots it was observed that the proton energy spectrum is transformed into a narrow peak close to the energy cutoff

(Fig. 5.2). The observed monoenergetic feature in the proton spectrum is strongly influenced by the shot-to-shot fluctuations of the laser pulse shape (ASE pedestal fluctuated by a factor of 3), which was not actively controlled, because the third-order scanning correlator is averaging over many shots and cannot be used for a single shot on-line measurement. As a result, the adjustment of the ASE requirement was not better as 10%–15%, which agrees well with the observations when a peak in the proton energy spectrum is formed. Such a narrow sharp peak was observed, when the laser pulse was focused not exactly in the center, but more to the rear side of the jet.

The protons with a broader energy distribution were created when the pulse was focused into the center (Fig. 5.3). However, the laser focusing position was controlled only qualitatively. The effective jet diameter was about 1 mm with a sharp density profile of the spray [150]. The laser was focused right below the nozzle. Within the region of about ± 0.25 mm from the center the proton signal does not change significantly. This uncertainty in the central position of the laser focus in the spray makes uncertain the focal spot position out from the center of the spray. It is believed that the focal spot position was less than 0.25 mm close to the rear side of the jet. Moreover, the monoenergetic proton feature was observed only in the laser propagation direction, while in the other directions a broad energy spectrum was always measured. In the directions of 45° and 135° the proton energies were somewhat lower than in the forward direction, but the number of fast protons was slightly higher. This is different from a previous experiment with single $20\ \mu$m water droplets reported in Ref. [20], where an enhanced signal was observed in the direction of 135°. The number and the energy of oxygen ions were much smaller than in the experiment with a single water droplet where all ions up to O^{6+} were observed (see Ref. [20]). This fact can be explained both by slowing down the oxygen ions produced inside each droplet - for 1 MeV protons, the stopping power is $0.27\ \mathrm{MeV}/(\mathrm{mg/cm^2})$ and for oxygen ions $6\ \mathrm{MeV}/(\mathrm{mg/cm^2})$ - and, most importantly, by the recombination of oxygen ions in the surrounding target material where the mean free path length is only about 10^{-3} cm.

5.2 Theoretical analysis of experimental results

Our theoretical explanation of obtained experimental results is based on a general discussion of the laser pulse interaction with a single water microdroplet (including ionization) and a cloud of such microdroplets called water spray (including the discussion of the propagation of laser prepulse and the main pulse inside the target), on numerical particle-in-cell simulations of the laser pulse interaction with a single homogeneously ionized water microdroplet of a diameter about $0.1\ \mu$m, and on estimates describing the ion energy distribution functions. The theory of ion acceleration in homogeneously ionized clusters is described in Chapter 2. Here, we add the theory of ion acceleration in a cloud of such sub-wavelength medium-sized clusters.

5.2.1 General discussion

The essential difference between the spray target and a thin foil is in a very large ratio of the surface to the volume. From the density and extension of the spray (see Ref. [150]),

one can estimate that the total surface of 1000 droplets is approximately $70\ \mu\mathrm{m}^2$, which is two times more than the surface of the laser focal spot. At the same time the total mass of 1000 droplets is the same as one droplet of a diameter of $1.5\ \mu\mathrm{m}$. Consequently, the laser energy absorption is rather efficient, and a larger deposited energy is distributed among fewer particles.

As discussed at the end of Chapter 2, the energy distribution in the exploding clusters depends on their diameter. In small clusters with diameters of a few tens of nanometers, which is of the order of the electron Debye length, the Coulomb ion repulsion is the dominant mechanism, and the ions are receiving the kinetic energy according to their initial position in the cluster: from 0 up to maximum energy. For this reason, energies of MeV per nucleon were never observed in small cluster targets. In addition, small clusters are much more sensitive to the laser prepulse and can be easily destroyed before the peak of the laser pulse. Big clusters with diameters in the 100 nm range are expanding under the pressure of hot electrons, which cannot leave the droplet because of its very high electric charge. Moreover, the ionization is very inhomogeneous: atoms in the outer layer of a thickness about the skin depth ($\approx 15\ \mathrm{nm}$) are being ionized by the laser electric field to a high degree (Z=4 or 5), while atoms in the inner part of the target can be ionized only by electron collisions. Consequently, their average charge is much lower ($Z \sim 1$). The ions of the external layer are gaining more energy, and one may expect a formation of a high energy peak in the ion spectrum. Therefore, it appears that the size of clusters and a high laser pulse contrast are the crucial parameters for efficient ion acceleration.

It can be shown, that during the time of laser pulse the electron-ion collisions can not smooth out the doubleshell structure of the submicrometer sphere. For the laser pulse duration τ_L, the number of scattering events can be evaluated as [26]

$$P = \nu_{ei}\tau_L = \frac{8\sqrt{2}\pi m_e Z^2 e n_i}{(E_L/\omega)^3}(\ln\Lambda)\tau_L, \tag{5.1}$$

where E_L is the laser electric field, ω is the laser frequency, and ν_{ei} is the electron scattering rate in the plasma with density n_i and ion charge Z.

For the laser parameters used and an average ion density $10^{18}\ \mathrm{cm}^{-3}$, $P \sim 10^{-8}$; i.e., elastic collisions of free electrons with ions do not occur during the laser pulse. The similar estimates can be made for the inelastic collisions as well. Thus, the double-shell structure is established in a submicrometer sphere: a highly ionized outer shell with a cold core inside is preserved during the laser pulse and it affects the whole dynamic of expansion and ion acceleration.

The laser pulse interaction with a target starts already at the edge of the spray. The ionization threshold of water is about $10^{12}\ \mathrm{W/cm}^2$, which is just about the level of the laser pulse pedestal in our experiments. The droplets are evaporated and the energy of the laser prepulse is dissipated by a preplasma formation. As the average density of the spray is well below critical, the laser pulse keeps propagating deeper inside the target, while the overall pulse contrast gradually increases. Assuming that the water droplet absorbs $\sim 10\%$ of the incident laser energy, the absorption cross section of a 150 nm droplet can be estimated as $\sim 10^{-9}\ \mathrm{cm}^2$, and, consequently the extinction length in the spray with the droplet density of $10^{11}\ \mathrm{cm}^{-3}$ is approximately $100\ \mu\mathrm{m}$. Therefore, the spray works as a saturating absorber - it absorbs the low intensity prepulse and transmits the main pulse. If focused sufficiently deep

into the spray, the main laser pulse interacts with still unperturbed droplets, which would produce high energy ion emission. This is reminiscent to an "inverse" plasma mirror effect. The plasma mirror [63] enhances the contrast by reflecting high intensity part of laser pulse, while here the fresh water droplets absorb the pedestal and the pulse peak is transmitted through low density plasma. Similarly to the plasma mirror, this scenario is very sensitive to the laser prepulse level, the spray density, droplet size, and the focusing conditions. For much higher contrast values (above 10^8 in our case) the situation is inverse: the prepulse passes through the transparent nonionized spray and only the main laser pulse is strongly absorbed.

5.2.2 Numerical simulations of the laser pulse interaction with a subwavelength-sized water microdroplet

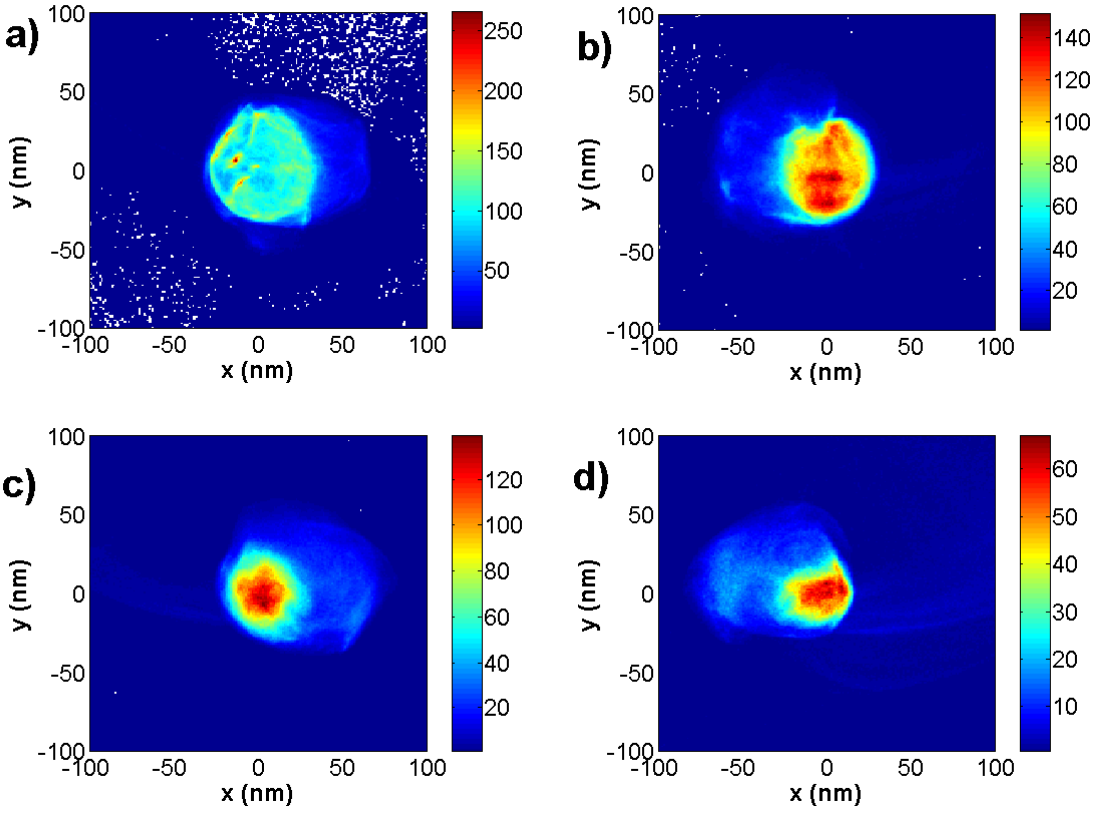

Figure 5.4: Electron density distributions at (a) 7.5τ, (b) 10τ, (c) 12.5τ, and (d) 15τ are presented (densities are evaluated in units of critical density n_{crit}). The laser propagation direction is from the bottom to the top (along y-axis). Electron cloud oscillates from the left to the right (or from the right to the left) during a half-laser period. One can also see the droplet ablation, which gradually reduces its radius.

The interaction of an intense laser pulse with a water droplet was simulated with our two-dimensional electromagnetic PIC code with three velocity components for electrons and

ions. Since the code does not account for the collisional and ionization processes, we consider a quasi-neutral plasma consisting of two ion species: the protons (p^+) and the oxygen O^{6+} ions in the ratio 2:1. The droplet was modeled with a cylindrical target ("microdroplet" in the 2D geometry) located in the center of the simulation box ($1.45\ \mu$m from boundaries on each side) with a diameter of 100 nm and the electron density $100n_{crit}$. The initial plasma temperature is 100 eV and the cell size is set to 1 nm. Periodic boundary conditions for particles and absorbing boundaries for fields are applied. The simulation box has the size $3.75\lambda \times 3.75\lambda$ ($3\ \mu\text{m} \times 3\ \mu$m). Absorption layers of the thickness 0.625λ ($0.5\ \mu$m) are added behind each side of the box. A p-polarized laser pulse at the wavelength $\lambda = 800$ nm has a super-Gaussian profile in the perpendicular plane (along x-axis) with the beam width 3λ at half maximum. The temporal laser pulse profile has a trapezoidal shape with a constant maximum intensity $2 \times 10^{19}\ \text{W/cm}^2$ (the dimensionless potential $a_0 = 3.1$) of a duration 11τ (30 fs), and two linear ramps of duration 2τ (5 fs) at the beginning and at the end of the pulse. In Figs. 5.4-5.7, the interaction time covers the period from 2τ to 17τ. The simulation run terminates at the time of 30τ, several periods after the moment when ions are reaching simulation box boundaries.

The electron density distributions at (a) 7.5τ, (b) 10τ, (c) 12.5τ, and (d) 15τ are presented in Fig. 5.4. The electrons from the surface layer are pulled out from the target and strongly heated. They are losing the phase resonance with the laser field each time as they are crossing the target and each period the electrons are gaining approximately the laser ponderomotive energy, $\varepsilon_{eh} = m_e c^2(\sqrt{1 + a_0^2/2} - 1)$, which is ~ 0.72 MeV. This corresponds essentially to the Brunel absorption mechanism, which is, however, different in the case of cluster, as the same electrons undergo the acceleration several times. Some of them are escaping from the target region, but the dominant part is attracted, accelerated backwards to the target, and in the next half of laser wave period enter the target and traverse it easily. The stopping power of 1 MeV electron in the water is about $1\ \text{g/cm}^2$, so the collisional effects are not important.

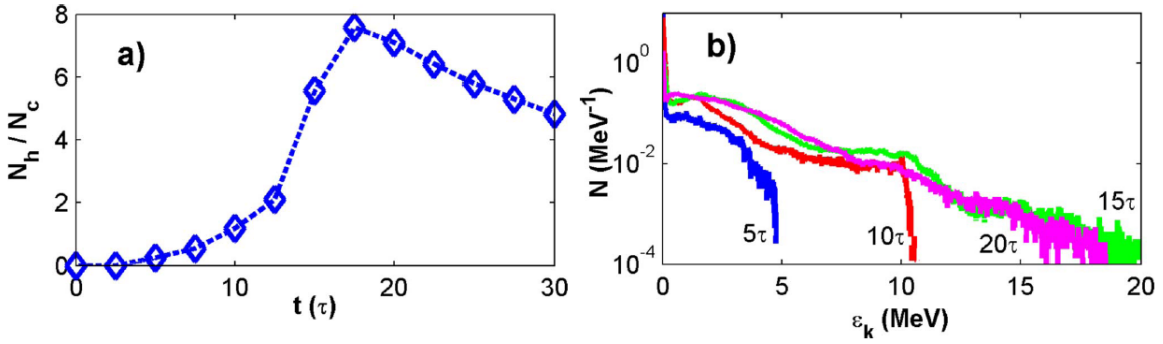

Figure 5.5: Evolution of electron energy in the simulation box. (a) The ratio of the number of hot to cold electrons. The electrons with the energy less than 250 keV are considered as cold. (b) Time evolution of the electron distribution function, at time instants 5τ, 10τ, 15τ, and 20τ shown in the legend. All electrons in the simulation box are included.

Time evolution of electron energy distribution function shown in Fig. 5.5 demonstrates that the number of hot electrons increases dramatically and cold electrons become in a minority halfway into the interaction. The hot electron temperature to the end of the laser pulse, $T_h = 3.0$ MeV, is more than four times the ponderomotive energy.

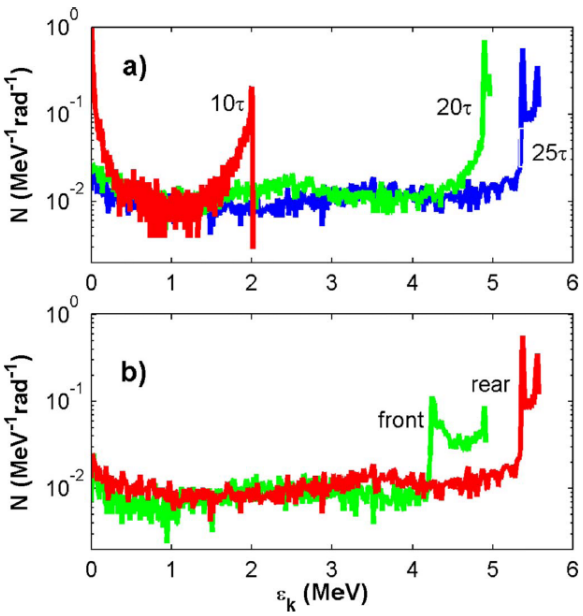

Figure 5.6: (a) Proton energy distribution function at the target rear side at time instants 10τ, 20τ, and 25τ. (b) Proton energy distribution function in the forward (red) and backward (green) directions accelerated at the target front and rear sides at 25τ.

Because of a relativistic laser intensity, trajectories of accelerated electrons in Fig. 5.4 are bent towards the rear target side by the magnetic component of the laser wave. This is the reason for more efficient ion acceleration at the rear target side. However, the difference in cutoff energies of protons accelerated from target rear and front sides is not significant; it is less than 20% (Fig. 5.6). The droplet ablation is clearly seen in the time sequence shown in Fig. 5.4. The droplet radius is reduced by a factor of 2 to the end of the laser pulse. Therefore, a significant part of ions is put in motion within first (20–30) fs. This time is shorter than the ion acceleration time in massive targets because of a higher electron temperature.

Proton energy spectrum shapes shown in Fig. 5.6 are very similar to those obtained in the experiment. They demonstrate a broad pedestal and a peak near the cutoff. The difference in energies of protons almost ten times compared to the experiment can be explained by the following factors. First, the efficiency of laser absorption in the 2D geometry and for the p-polarization is higher than that in the real three-dimensional (3D) case. Second, the droplet in the simulation is of a smaller size and it is completely ionized, so the energy absorbed per particle is almost ten times bigger; it is about (3–4) MeV/n. One can see in Fig. 5.6 that the energy distribution function before the peak is approximately constant in agreement with Eq. (2.89) for the Coulomb explosion part of the spectrum with $\nu = 2$ (in 2D). In 3D case, the Coulomb explosion spectrum is proportional to $\sim \sqrt{\varepsilon_i}$ which can be seen in the insert in Fig. 5.2 (without the peak). Eq. (2.89) describes the explosion of cluster with a single ion species, thus the spectrum is without a narrow peak. The peak in the proton energy spectra near the cutoff is caused by mutual interaction between two ion species as reported in Ref. [107].

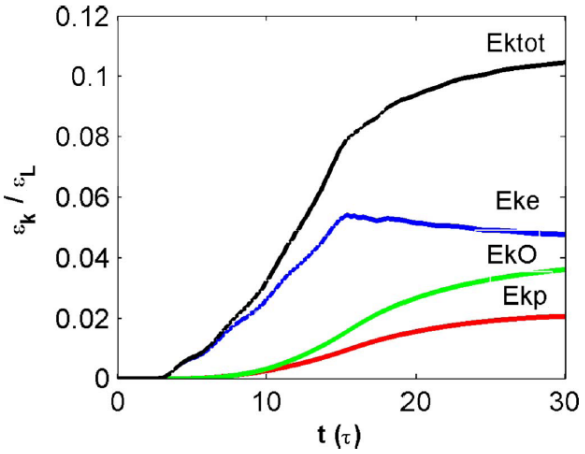

Figure 5.7: Energy balance in the simulation. Horizontal axis shows the time in the laser periods, the vertical axis stands for the particle kinetic energy divided by the total laser energy. The total absorption is more than 10%. Ektot—kinetic energy of all particles in the simulation box; Eke—kinetic energy of all electrons; EkO—kinetic energy of oxygen ions; Ekp—kinetic energy of protons

The energy balance in the simulations is shown in Fig. 5.7. The electrons are absorbing energy during the interaction with laser pulse and gradually they are transferring it to ions. The protons, as lighter particles are accelerated first. During the time of about 15 laser periods they are gaining about 90% of their kinetic energy. To the end of the run they are carrying about 20% of the absorbed energy. The acceleration of oxygen ions occurs later in time and they are gaining approximately five times less energy per nucleon because of the species spatial separation in expanding cluster and the electric field screening by fast protons.

To the end of the run the ion cloud achieves the radius of more than $1\ \mu\mathrm{m}$, which is the average distance between the droplets in the experiment. At this moment the separate clouds from each droplet mix together and the plasma expands from the focal volume adiabatically. The electrons will cool down and one may suppose the ion kinetic energy will increase by a factor of 2.

5.2.3 Energy distribution of accelerated protons

The numerical simulations have shown that the Brunel absorption is the dominant mechanism of the laser energy deposition into the droplet. Although the absorption is inhomogeneous over the droplet surface, the most efficient absorption takes place in the left and right segments where the laser electric field is perpendicular to the surface. Fast electron circulation redistributes promptly the absorbed energy in the cluster. One can then characterize the efficiency of laser absorption by a cross section σ, which is proportional to the droplet cross section, $\sigma = \alpha\pi r_c^2$ (here, r_c is the droplet radius). According to our numerical simulations, the parameter $\alpha \sim 0.1$ in the relativistic regime. However, it should be smaller in the 3D case. For the droplet radius $r_c = 75\ \mathrm{nm}$, the geometric cross section is $\sim 1.7 \times 10^{-10}\ \mathrm{cm}^2$, and taking $\alpha \sim 0.1$, the estimated absorbed energy is about $0.1\ \mathrm{mJ}$. Here, one can see the

major advantage of the spray: having 10^{11} cm^{-3} water droplets, one has a very developed surface and consequently a relatively short laser absorption length, which is of the order of a few hundred μm. Having in mind that the droplet contains about 10^7 water molecules, the energy deposition is ~ 60 MeV/mol, or 2 MeV/n. This estimate agrees with the observations.

It has been already discussed in Chapter 2 that the energy spectrum of ions depends on the mode of cluster explosion; that is, on the ratio Λ_s of the cluster radius r_c to the hot electron Debye length λ_D. In our case, $\lambda_D \sim 50$ nm is slightly smaller than r_c, and the explosion of the inner part of the cluster is ruled by the electron thermal pressure, but the outer shell, which is ionized to a much higher degree, is a subject of the Coulomb-like explosion. If we apply the model of self-similar adiabatic expansion of an ionized sphere [106], by considering the electrons as an ideal gas with polytrophic constant $\gamma = 4/3$, and the protons as test particles, the proton distribution function (2.89) can be written as

$$\frac{dN}{d\varepsilon_p} = \frac{n_{p0}}{\varepsilon_0}\sqrt{\frac{\varepsilon_p}{\varepsilon_0}}\left[\frac{6}{\Lambda_s^2} + \exp\left(-\frac{\varepsilon_p}{\varepsilon_0}\right)\right] \tag{5.2}$$

where $\varepsilon_0 \approx 2\varepsilon_{eh}$ is the characteristic energy and ε_{eh} is a function of local laser intensity. The maximum proton energy (2.85) is determined by

$$\varepsilon_{pmax} \approx 2\varepsilon_{eh} W(\Lambda_s^2/2) \tag{5.3}$$

where W is the Lambert function (2.87), $\Lambda_s \sim 3$. The energy distribution function of protons has the form of Eq. (5.2) and additionally, the high energy peak is formed. These protons are running ahead of oxygen ions as it was discussed previously.

The fitted proton energy distribution function based on the previous discussion is shown in the inset of Fig. 5.2 (red line). The most energetic protons come from the outer high ionized shell (oxygen ions with $Z \approx 4$) which is a subject of Coulomb-like explosion. The low energy protons are accelerated mostly from the low ionized (Z=1) inner shell of the submicrometer spheres due to electrostatic and hydrodynamic expansion. This model of ion acceleration is in a good agreement with the experimental observations.

The proton energy spectrum with a broad maximum shown in Fig. 5.3 can be explained by variation of the laser intensity along the spray, so the energy deposition per droplet varies depending on its position with respect to the focal plane. The corresponding ion distribution function can be calculated by averaging the proton distribution spectra over the laser intensity distribution in the confocal area (2.37). The inset of Fig. 5.3 shows the calculated averaged proton distribution function (red line).

5.3 Conclusion

Experiments on ion acceleration in a cloud of sub-wavelength-sized water microdroplets (the so-called water spray target) demonstrated that the maximum energy and the shape of energy spectra of accelerated protons strongly depend on interaction conditions (prepulse level and the position of the laser focus in the spray). Due to a very large ratio of the surface to the volume in the spray target, the laser energy absorption is rather efficient and a larger deposited energy is distributed among fewer particles in comparison with bigger

mass-limited targets. With increasing laser pulse contrast, a narrow sharp peak in the proton energy spectra was observed in the direction of laser pulse propagation, when the laser pulse was focused not exactly in the center, but more to the rear side of the jet, whereas the protons with a broader energy distribution were created when the pulse was focused into the center.

The physics of the femtosecond laser pulse interaction with a water spray is rather complex as one has to take into account many phenomena such as the influence of the laser prepulse on ablation of microdroplets, target ionization, laser intensity distribution in the spray, the position of the laser focus, and so on. Based on our estimates demonstrating the inefficiency of ionization by electron-ion collisions, we suppose that the ionization in larger clusters is very inhomogeneous in the experiment as only atoms in the skin depth ($\sim 15\ \mathrm{nm}$) are ionized by the laser electric field to a high degree of ionization. We contributed to the interpretation of obtained experimental data by numerical simulations of the laser pulse interaction with a water microdroplet of a diameter of 100 nm which gives an insight into the physics of ion acceleration and facilitates following analytical estimates. The proton energy spectra from 2D PIC simulations are in agreement with the model of adiabatic expansion of ionized sphere (of one ion species) presented in Ref. [106] except for the peak formation at the maximum energy. Here, the peak in the proton energy spectra can be explained by mutual interaction between protons and oxygen ions. In a more complex spray target, the laser intensity distribution in the confocal area, or the recombination and collisional effects in the surrounding target material has to be taken into account. Presented estimates show that the recombination and decelerating of (mainly) oxygen ions are significant, which explains relatively small number of oxygen ions observed in experiments. If the laser pulse is focused close to the rear side of the jet, the proton energy spectra can be well fitted by the spectra from the expansion of a single ionized water microdroplet including mutual interaction between two ion species. In the case of laser beam focusing in the spray center, the proton energy spectra could be fitted by the energy distribution function averaged over the laser intensity distribution in the confocal area.

In my opinion, the presented theoretical interpretation of experimental results has several issues which have to be further investigated. Firstly, it would be desirable to include the field and collisional ionization into the simulation of the laser pulse interaction with a single microdroplet to observe the time evolution of the distribution of oxygen ions with various charges inside the droplet. Secondly, the fitting of proton energy spectra is questionable as one cannot well describe the process of recombination and slowing down of oxygen ions (and also protons), especially when the focal spot is placed in the center of the spray. Here, we proposed simple models, which should be further developed or even substituted if necessary. For example, a broader proton energy distribution when the laser pulse is focused to the center of the spray target could be also explained by a lower repulsion between oxygen ions and protons due to a lower number and charge of the heavier ions as they has to penetrate on a longer track beyond the target.

Chapter 6

Lateral hot electron transport and ion acceleration in thin foils

6.1 Introduction

In Chapter 2, we have already presented the recent theoretical analysis, numerical simulations and experiments [28]-[33] of a short laser pulse interaction with thin foil targets that revealed a fast electron current propagating along the target surface. This surface current is generated by a short laser pulse of a relativistic intensity ($I\lambda^2 \approx 10^{19}\ \mathrm{Wcm^{-2}}\mu\mathrm{m}^2$) when it is incident on a plane target at large angles $\alpha \sim 70^\circ$. It has been also demonstrated that generated strong quasi-static magnetic and electric fields confine electrons in a potential well along the target surface and the electrons can be resonantly accelerated by the laser electric field inside the potential well [34]. This could result in electron energies exceeding the ponderomotive potential and in a transport of those electrons along the target surface far beyond the interaction region.

Another mechanism of the lateral electron transport is due to hot electron recirculation in the thin foil [3], [39]. In this case, the majority of accelerated electrons pass through the target and they are reflected in the expanding Debye sheath on the rear surface. This results in reversing of the normal component of electron velocity while the transverse velocity is largely unaltered. Hot electrons reflux in the foil many times and propagate towards target edges. There, the expansion is halted by the lateral component of the electrostatic field caused by the buildup of net negative charge and accumulated electrons enhance the ion acceleration. The resulting energetic ion emission from the edges of thin target foils, was investigated in Ref. [151] for a smaller incidence angle of 45° and a higher intensity ($I\lambda^2 \approx 6 \times 10^{20}\ \mathrm{Wcm^{-2}}\mu\mathrm{m}^2$).

Electron transport has been also studied in cone targets designed for fast ignition. Electrons can be focused to the cone tip and concentrated in a small volume there. Papers [152]-[155] report on fast electron guiding along cone walls. The effect of electron recirculation also seems to be important. In the double-cone target, proposed in Ref. [156], the conducting cone wall is covered by a dielectric layer. It isolates the inner cone from a corona plasma, generated by the laser radiation incident on the outer cone surface. Such a configuration allows the high energy electrons (which cross the inner cone wall) to be confined inside the inner cone by the sheath electric field. For the laser pulse that is incident on the cone wall

at large angles ($\sim 75^\circ$) a remarkable difference is found between single- and double-cone targets surrounded by a coronal plasma. The electron energy flux to the cone tip is much stronger in the latter case, which indicates an importance of the recirculation hot electron transport mechanism. The physics of electron transport in cone targets is even more complicated as one also has to take into account laser beam focusing towards the cone tip. This effect is outside the scope of this study where a flat thin foil is considered.

Fast electron guiding outside the laser-plasma interaction region was experimentally and numerically demonstrated using a fine straight carbon wire attached to the cone target in Ref. [157] and a plasma inverse cone in Ref. [158]. The guiding of electrons carrying high current is explained by a high conductivity of a plasma with respect to return current electrons. The high energy electrons that escape from plasma create strong electric and magnetic fields near the plasma-vacuum boundary. These fields confine fast electrons and force them to propagate along the target surface, perpendicularly to the gradient of electric conductivity. This effect was also demonstrated in numerical simulations [159], [160] and in experiments [161].

Motivated by these results, we investigated fast electron transport towards foil edges and resulting ion acceleration. We performed 2D PIC simulations of interaction of a femtosecond laser pulse with an ionized foil target and studied the dependence of the electron lateral transport on the laser incidence angle and polarization. The latter is also quantified by analysis of characteristics of fast protons emitted from foil edges.

6.2 Simulation method and parameters

We employed our relativistic colisionless particle-in-cell (PIC) code in two spatial directions and with three velocity components described in Chapter 3. To investigate the lateral electron transport itself and its effect on proton acceleration, several simulation setups were chosen. The incidence angles of 30°, 45°, 60°, and 75° were considered for both p- and s-polarizations of the laser beam. Additional series of numerical simulations were performed, where the hot electron recirculation is suppressed by choosing a special condition at the rear foil side - the fast electrons escaping to vacuum are replaced by thermal electrons in order to distinguish between different effects controlling the fast electron transport along the target surface. Other simulation parameters are similar for all runs.

Simulation geometry is illustrated in Fig. 6.1. A fully ionized foil of the size $77\lambda \times 2\lambda$, consists of electrons and protons of the initial density $20\ n_c$ (where n_c is the electron critical density). Additionally, to enhance the laser energy absorption, a density ramp has been introduced with the exponential profile and with the density scale length $L = 0.1\lambda$ on the front side of the target. The transverse foil size is set to be two times larger than the laser focal spot for the largest incidence angle, i.e., $(10\lambda/\cos 75^\circ) \times 2 = 77\lambda$, in order to observe the lateral transport and dissipation of the surface electron current outside the interaction zone. A laser beam at the wavelength $\lambda = 1.0\ \mu\mathrm{m}$ has a super-Gaussian profile ($n = 5$) in the perpendicular plane with the width 10λ at half maximum. The larger beam width is chosen according to Ref. [34] in order to enable surface electron acceleration, which requires large incidence angles and focal spot sizes as the electrons propagating along the target surface are accelerated by wiggling inside generated quasi-static and laser fields.

The initial plasma temperature is 1 keV and the cell size is set to 20 nm; 200 particles

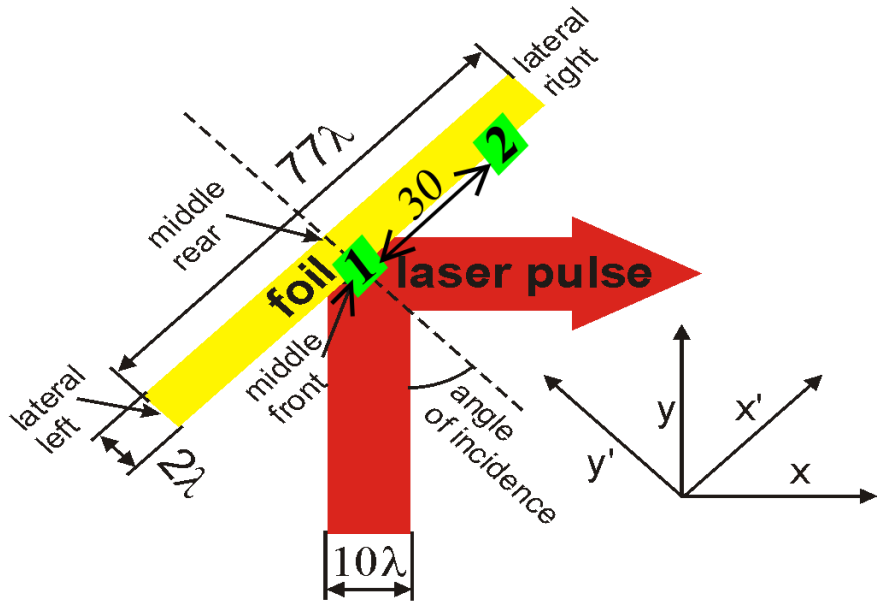

Figure 6.1: Parameters of simulations and configuration of numerical diagnostics. Laser beam initially propagates along y-axis, interacts with a foil and is reflected. Some electrons are heated during the interaction and they accelerate protons. Ion emission is investigated from the front, rear and lateral faces of the foil, and electron characteristics in regions 1 and 2.

per cell are used for each species at the maximum density and the total number of particles is about 1.6×10^8. Absorbing boundaries for fields are applied. Electrons reaching the simulation box boundaries are frozen there. The size of simulation box was chosen to be sufficiently large so that during the simulation time no protons were reaching the boundaries and were affected by an electric field created by the frozen electrons. The temporal laser pulse profile has a trapezoidal shape with a constant maximum intensity 3.4×10^{19} W cm^{-2} (the dimensionless amplitude $a_0 = 5.0$) of duration 20τ (in laser periods, 67 fs), and two linear ramps of duration 5τ (17 fs) at the beginning and at the end of the pulse.

We recorded the electric and magnetic fields, electron and proton phase spaces each five laser periods in the simulation. Then, the data were analyzed with Matlab scripts. The lateral transport is quantified by studying the total, that is, laser-to-proton conversion efficiency, the number of accelerated protons in characteristic directions and the cutoff energies of protons, which are emitted from foil edges.

6.3 Results and discussion

6.3.1 Hot electron guiding

In the case of p-polarization, our simulations with large laser pulse incidence angles (75° and 60°) show that some electrons are pulled out from the target front by the electric field of

the laser wave and their trajectories are bent parallel to the surface by the magnetic field of the wave. A part of those ejected electrons is pulled back into the target, but some of them rest close to the target front and form a bunch which moves along the surface. This can be seen in the left panel of Fig. 6.2, where are shown separately negative (formed by accelerated electrons moving towards lateral right side) and positive (formed by return current electrons) current densities in longitudinal direction to the initial target surface. The fast electrons are moving outside the target while the return current is flowing in a dense plasma at the target surface. The bunches are distributed regularly with $\lambda/\sin(\alpha)$ interval. That indicates that the Brunel absorption mechanism dominates in this case.

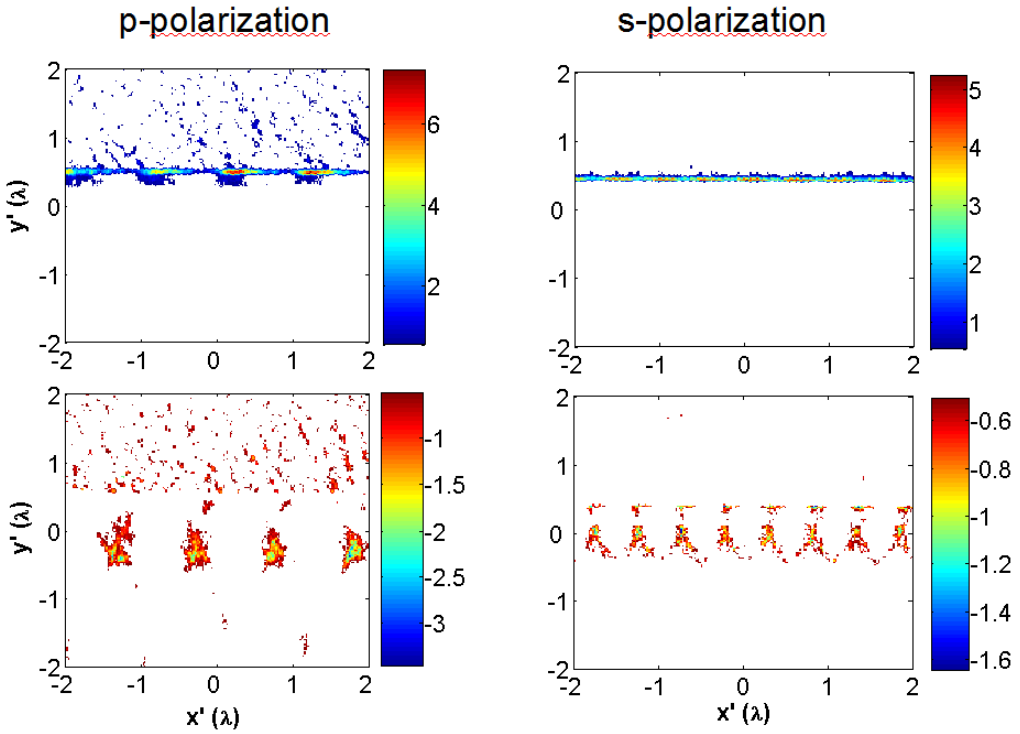

Figure 6.2: Longitudinal current densities with respect to the target surface during interaction with p-polarized (left) and s-polarized (right) laser pulses in the case of incidence angle equal to $75°$. Current densities are normalized by $en_{crit}c$ and only the densities higher than 0.5 are displayed. Target interior with a maximum plasma density is located from $y' = 0.5\lambda$ to $y' = 2.5\lambda$, the initial plasma-vacuum interface is at $y' = 0$. Upper line - the positive current created by "cold" plasma electrons; bottom line - the negative current created by laser-accelerated fast electrons.

In the case of s-polarization, the oscillating electric field is parallel to the foil surface and perpendicular to the simulation plane, the electrons cannot be pulled out from plasma directly by the electric component of the laser wave, but they can be ejected by $j \times B$ force. Therefore, the bunches of electrons are ejected twice per laser period and are distributed regularly with $\lambda/(2\sin(\alpha))$ interval. Thus, the period is twice shorter and the maximal current is smaller compared with the p-polarization case. This is demonstrated in the right panel of Fig. 6.2 together with the return current.

The maximum density of electrons in bunches observed in simulations is about 2 n_{crit}. The separation between the fast electron and return currents give rise to the quasi-static electric and magnetic fields at the target front. These surface magnetic field and charge separation electric field form a potential well as it is described in Chapter 2 and surface fast electrons are confined there.

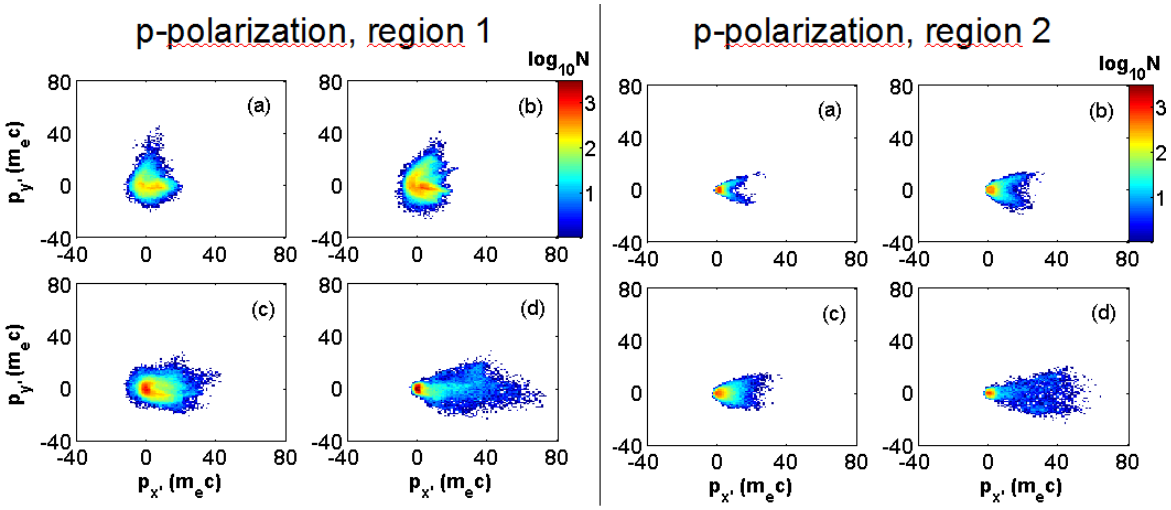

Figure 6.3: Phase spaces (p'_x, p'_y) of electrons in the region 1 and 2 for the p-polarized laser pulse. Incidence angles: a) 30°, b) 45°, c) 60°, d) 75°

.

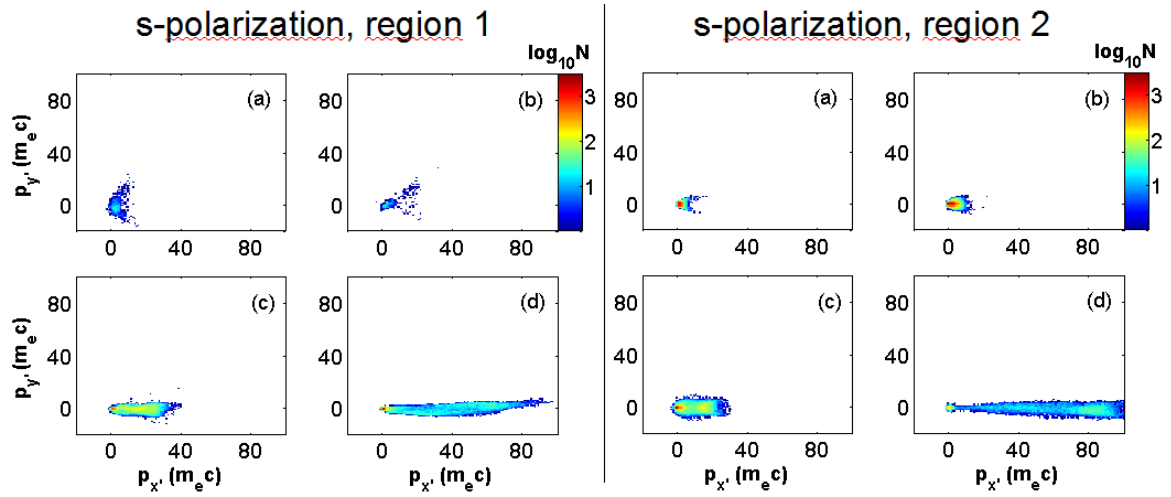

Figure 6.4: Phase spaces (p'_x, p'_y) of electrons in the region 1 and 2 for the s-polarized laser pulse. Incidence angles: a) 30°, b) 45°, c) 60°, d) 75°

.

The guiding of hot electrons is well documented in the phase space $(p_{x'}, p_{y'})$ in two distinct regions marked as 1 and 2 in Fig. 6.1 - in the interaction region and outside the focal

spot, see Figs. 6.3 and 6.4. The guided electrons should have $|p_{y'}| \ll |p_{x'}|$, i.e. a low angular spread. This is clearly the case for s-polarization. In the case of p-polarization, the electron spectrum in $p_{y'}$ is broad even for the largest incidence angle of 75°. This indicates that the recirculation of hot electrons forth and back significantly contributes to their lateral transport. For these electrons, $p_{y'}$ varies from positive to negative values, and they recirculate, whereas $p_{x'}$ is largely unaltered. In panels of Fig. 6.3 related to region 2, one can see that for smaller incidence angles (30° and 45°), there are less electrons with $p_{y'} \approx 0$ than that with non-zero $p_{y'}$ (positive or negative). This indicates that the major part of electrons is laterally transported by the recirculation. A strong lateral transport ascribed to the recirculation was measured experimentally even several mm outside the focal spot [151]. In the s-polarization case, the guiding of electrons is more evident for incidence angles of 60° and 75° than in the case of p-polarization. The electrons have a very low angular spread in the simulation plane, as it is shown in panels $(p_{x'}, p_{y'})$ in Figs. 6.3 and 6.4.

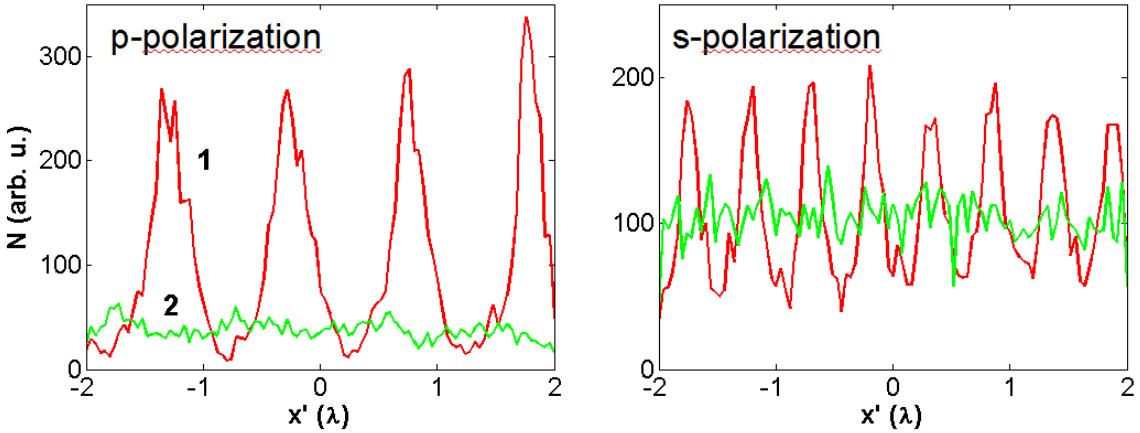

Figure 6.5: Density of hot electrons along the target front in two time instants in surface regions 1 and 2 (incidence angle of 75°). Only electrons with energy higher than 3 MeV are taken into account. The first region is located in the center of interaction zone. The second region is shifted along the front surface 30λ to the lateral right side and recorded about 30τ later than the first, which corresponds to the shortest time needed for electrons to be moved from the first to the second region. The region is located from $y' = -1.0\lambda$ to $y' = 0.5\lambda$, initial plasma-vacuum interface at $y' = 0$.

Outside the spot region, accelerated bunches of electrons are gradually broadened into continuous electron current and dissipated, more rapidly in the case of p-polarization. The electron densities on the front foil surface are shown in Fig. 6.5. For p-polarization, additional series of numerical simulations were performed, where the hot electron recirculation was suppressed. The results on proton acceleration (Fig. 6.7 and 6.8 discussed in the next section in detail) confirm that the surface guiding really takes place outside the laser-plasma interaction region in agreement with observations reported in Refs. [157], [158], and that the lateral transport is mainly due to multiple recirculation of electrons through the foil for smaller incidence angles of 30° and 45°.

The electron energy spectra at the foil front surface are shown in Fig. 6.6. The spectrum

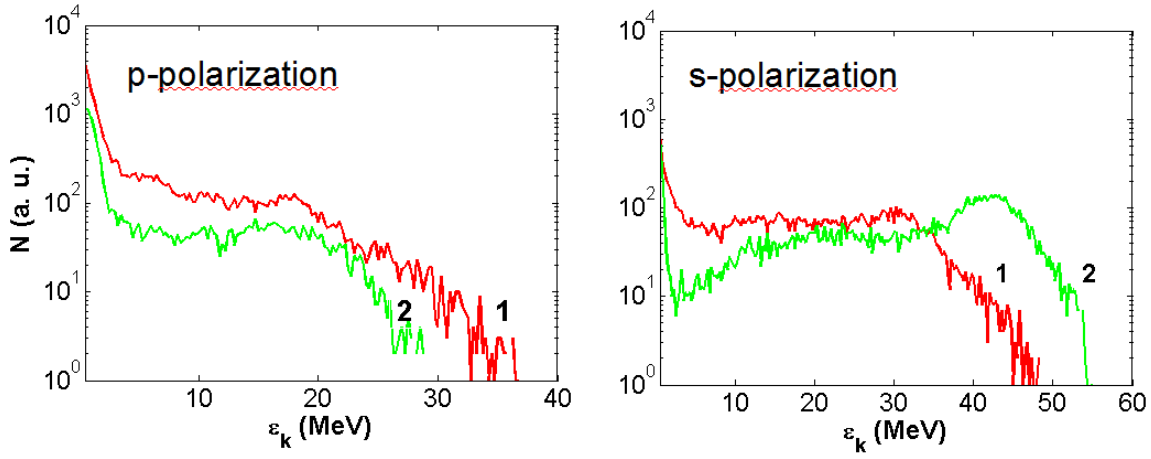

Figure 6.6: Energy spectra of hot electrons (with kinetic energy $\varepsilon_k > 100$ keV) for the incidence angle of 75° on the target front in the region 1 and 2. The first region is located in the center of interaction zone. The second region is shifted along the front surface 30λ to the lateral right side and recorded about 30τ later than the first, which corresponds to the shortest time needed for electrons to be moved from the first to the second region. The region is located from $y' = -1.0\lambda$ to $y' = 0.5\lambda$, initial plasma-vacuum interface at $y' = 0$.

contains a high energy tail. The energy of electrons in this tail is much higher than the value of ponderomotive energy (2.50), $\varepsilon_{eh} \approx m_e c^2(\sqrt{1 + a_0^2/2} - 1) \approx 1.5$ MeV. Such spectra are in agreement with the simulations of Ref. [34]. That confirms that the surface acceleration takes place in the laser irradiated zone. In the case of p-polarized pulse, the electron energy in the region 1 is higher than in the region 2. This is also manifested in the phase space shown in Fig. 6.3. That indicates that the most energetic electrons leave the potential well before the moment when they could be accelerated to higher energies. We roughly estimate from electron position and momentum snapshots (taking into account the total energy of all electrons with energy higher than 3 MeV in the region $x' = 0 \ldots 40\lambda$, $y' = -1\lambda \ldots 0.5\lambda$ in time instants corresponding to the end of the pulse interaction with target center located at $x' = 0$, $y' = 0$) that about 2% of the laser energy is guided for the incidence angle of 75° and about 1.5% for 60°, compared with the total laser energy absorption 30% and 40%, respectively.

In the s-polarization case, the electron energy spectra have different character than for the p-polarized pulse. For the incidence angle of 75°, the electrons are evidently gradually accelerated along the foil surface, as can be seen in the right panel of Fig. 6.6. In the interaction region 1, there is a plateau between 3 and 30 MeV, where the number of electrons is approximately constant. In the region 2, the number of electrons is increasing between 3 and 40 MeV. The similar effect, but less pronounced, was also observed for the incidence angle of 60°. Since the driving electric and magnetic fields exist only inside the spot region, the acceleration length is limited by the laser spot size. Outside the spot region, bunches are broadened into continuous electron current, but the electron density is several times higher than for p-polarized pulse as can be seen in Fig. 6.5. Concerning the energy balance, about

10% of the laser energy is guided for 75° and about 3% for 60°, compared to the total laser energy absorption about 20% in both cases. For incidence angles of 30° and 45°, the guiding is strongly suppressed (Fig. 6.3 a, b). Note that the laser energy absorption is only from 10% to 15% for smaller angles (30°, 45°) in the s-polarization case in comparison with 40% and 50% for p-polarization.

The physical mechanism of electron surface acceleration is rather similar to the betatron acceleration in laser channels reported in Ref. [82] and further discussed in Ref. [83]. The major difference is in the fact that the phase velocity of the laser field propagating along the target surface $v_{ph} = c/\sin(\alpha)$ depends on the angle of incidence. Necessary conditions (2.66), (2.67) for the electron trapping in the acceleration phase are discussed in Chapter 2. They depend on the gradients of the guiding electric and magnetic fields, $\kappa_E = dE_{y'}/dy'$ and $\kappa_B = c\,dB_z/dy'$, on the wave phase velocity v_{ph} along the foil front surface, and the particle initial energy $\gamma_{e0} = 1 + \varepsilon_{e0}/(m_e c^2)$.

Both conditions are readily satisfied for our simulations with the incidence angles of 60° and 75°. The minimum trapping electron energy ε_{e0} is of the order of $2 - 3$ MeV, which is of the order of the ponderomotive potential in the incident laser field ($\varepsilon_{eh} \approx 1.5$ MeV as estimated above). The required gradient of the quasi-static electric and magnetic fields is of the order of $(1-2)\ \mathrm{kV}\cdot\mu\mathrm{m}^{-2}$ for the incidence angle of 75° and it increases as the incidence angle decreases. This explains the most efficient electron guiding and acceleration for the incidence angle of 75°. The difference between the s- and p-polarization cases can be explained by the simulation geometry. As the plasma and laser field are supposed to be homogeneous in z-direction, there is no localization in that direction and the electron acceleration is due to the electron rotation in the x', z-plane, and no broadening in the y'-direction can be seen.

6.3.2 Proton acceleration

The ions are accelerated in the electrostatic sheath formed by hot electrons usually on the rear side of a thin solid foil. The strength of the electrostatic field can be estimated as (2.71), directly proportional to the product of hot electron density n_h and temperature T_h. It is often considered that the hot electron temperature in laser interaction with solid targets is of the order of the ponderomotive energy (2.50), and the hot electron density cannot exceed the critical density. However, these parameters depend strongly on the target shape and interaction conditions. The electrons confined at the front surface layer may interact with the laser field many times, which would result in a temperature higher then the ponderomotive energy [34]. Moreover, the hot electron density n_h can be enhanced by the target geometry. With higher values of T_h and n_h, higher sheath electric fields are expected, which will be translated in higher energies of accelerated ions and in enhanced laser-to-proton conversion efficiency.

More precisely, the maximum ion energy and the total ion energy are described by the model of isothermal plasma expansion [66] discussed in Chapter 2. Here, the electrostatic energy of accelerating electric field is translated into the kinetic energy of ions. The maximum ion energy and the total energy of accelerated ions from a unit surface scale as

$$\varepsilon_{imax} \simeq 2ZT_h \ln^2(\omega_{pi} t_{acc}/2e_N), \qquad W_{itot} \simeq T_h n_h c_s t_{acc}, \tag{6.1}$$

where $\omega_{pi} = \sqrt{Ze^2 n_h/\epsilon_0 m_i}$ is the partial ion plasma frequency, $c_s = \sqrt{ZT_h/m_i}$ is the ion acoustic velocity, e_N is the Euler number, and t_{acc} is the acceleration time. The maximum proton energy is proportional to T_h, while the total energy of accelerated protons depends stronger on the density and is proportional to surface. Thus, very energetic (but less numerous) electrons guided along the foil front surface should lead rather to a high maximum energy of protons emitted from foil edges than to their relatively high total energy.

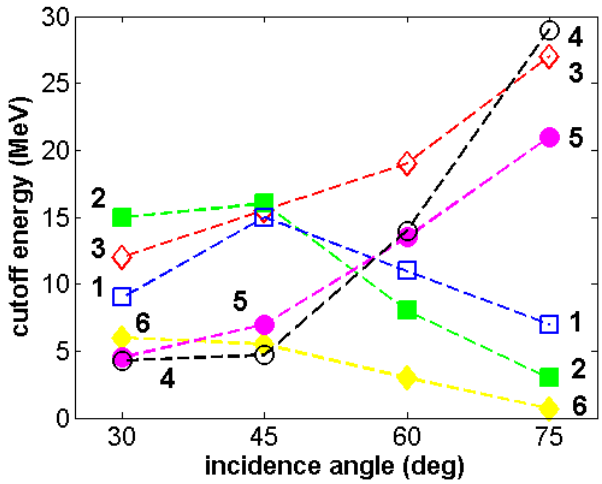

Figure 6.7: Dependence of maximum energies of protons on the position of the emission zone on the target and the incidence angle: 1 - middle front; 2 - middle rear; 3 - lateral right; 4 - lateral right, s-polarization; 5 - lateral right r.b.c.; 6 - lateral left; "r.b.c." denotes the simulation cases where the fast electrons escaping to vacuum are replaced by thermal electrons of Maxwellian distribution with initial temperature about 1 keV; all the lines except for line 4 are related to p-polarized laser pulse.

To confirm these qualitative considerations, we compare fast ion characteristics in simulations with four laser beam incidence angles (30°, 45°, 60°, 75°). Dependencies of maximum proton energy ε_{imax} and ion energy fluence W_{itot} (that is, the total energy of ions accelerated from a unit surface) on the incidence angle are shown in Figs. 6.7 and 6.8. These values are calculated from spectra "measured" in the rectangular area of width 1.75λ perpendicular to the surface in the center of foil on its front, rear sides, and on lateral sides at the time of about 250 fs after the interaction of the laser pulse with the target, when the ion acceleration process is terminated. The acceleration from left side is relatively weak and decreases with increasing incidence angle as the hot electrons are mostly accelerated in the direction of the laser wave vector projection onto the foil surface towards lateral right side. There, a strong proton acceleration takes place for large angles.

The maximum proton energy on lateral right side is 27 MeV and 29 MeV and the corresponding ion energy fluence about 21 $\mathrm{kJ/cm^2}$ for p-polarization and 16 $\mathrm{kJ/cm^2}$ for s-polarization, respectively, in comparison with the energy fluence of laser pulse about $2.8\ \mathrm{MJ/cm^2}$. The number of accelerated ions is higher for the p-polarization in spite of a stronger confinement of absorbed laser energy in the case of s-polarized pulse. This fact can be explained

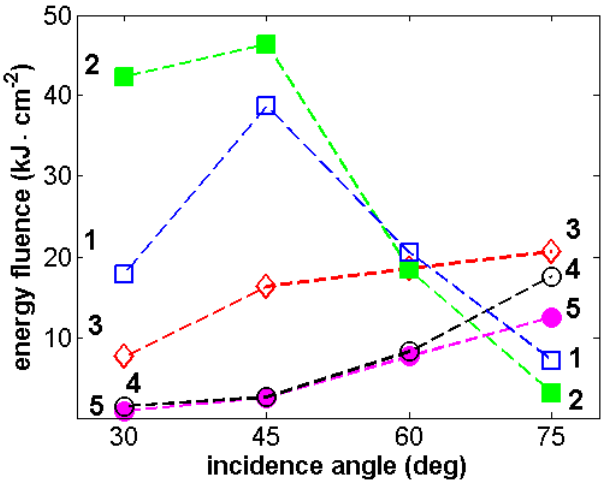

Figure 6.8: Energy fluences of protons emitted from different target regions for incidence angles of 30°, 45°, 60°, and 75°. Only protons with kinetic energy higher than 1 MeV are taken into account. Line numbering has the same meaning like in Fig. 6.7.

by the electron energy spectrum shown in Fig. 6.6. In the region 2 (close to lateral right foil side), the electron distribution in the case of s-polarization is not favorable for an efficient proton acceleration, because it is dominated by a relatively small number of fast electrons. These most energetic electrons overcome the potential barrier created by the ions and by themselves, and are lost from the system (they are accumulated on the boundaries of the simulation box), whereas less energetic "bound" electrons participate in the acceleration, according to a theoretical model of Ref. [90]. The isothermal plasma expansion in the case of lateral acceleration is limited because the electron energy distribution function is not Maxwellian and the electrostatic field decreases strongly due to 2D effects.

In the case of p-polarization, additional simulations were performed to demonstrate explicitly the effect of electron surface guiding on proton acceleration. The runs where hot electron recirculation is artificially suppressed show that the recirculating electrons (which are mostly observed in the p-polarization case) contribute significantly to proton acceleration, even for the largest incidence angle. A significant difference between a standard simulation and the run with the substitution of hot by thermal electrons on the rear foil side can be observed, both, in the cutoff energy (Fig. 6.7) and in the energy fluence (Fig. 6.8) related to the lateral right foil side. The difference is more pronounced in the proton energy fluence as the most energetic electrons guided along the surface (which are presented in all simulations) enhance mainly the cutoff energy, whereas recirculating electrons (less energetic) are contributing into the enhancement of the fluence. The proton energy characteristics reveal that the hot electron transport along the front surface also takes place for smaller angles of incidence, but a fraction of confined electrons gradually decreases with the angle as it was already described in Ref. [30].

6.3.3 Efficiency of ion acceleration

Let us introduce the laser-to-proton energy conversion efficiency (2.75), which is, in our case, defined as the ratio of the total energy of fast ions (with kinetic energy higher than 1 MeV), emitted from a whole corresponding foil surface (foil side), to the laser pulse energy. In the s-polarization case, the laser energy absorption is quite low, which reduces the efficiency of proton acceleration from rear foil side - the maximum energy reaches 4 MeV for smaller angles and it is below 1 MeV for larger angles. The acceleration from rear foil side is much more pronounced with the p-polarized laser pulse and the following discussion is related to this case. Here, one can see a common feature that the acceleration is more efficient for smaller angles of incidence (30°, 45°), where the laser absorption is higher.

The conversion efficiencies are 7%, 11%, 4%, 1% on the rear side and 4%, 9%, 9%, 4% on the front side for incidence angles of 30°, 45°, 60°, 75°, respectively. The most efficient proton acceleration takes place for 45°, which correlates well with the maximum laser pulse energy absorption in this case. We recall that the laser energy absorption in our simulations is about 40%, 50%, 40%, 30% in the sequence of increasing incidence angle. The conversion efficiency of ions accelerated from lateral right side is about 0.5% in the case of p-polarization for the largest incidence angle. Generally, the conversion efficiencies are much higher from rear/front foil sides, although the maximum energy of protons is enhanced on lateral foil side. However, it is necessary to take into account the size of front/rear foil side which is about 40 times higher than the size of the lateral side.

If the electron cooling (that is, a substitution of hot electrons by the thermal ones) is applied on the rear foil side, the acceleration of protons is reduced on the foil front mainly for smaller angles as a large part of hot electrons propagates into the target and cannot recirculate and accelerate protons from the front side. The corresponding conversion efficiencies are 0.5%, 3%, 6%, 3%, respectively, thus, they illustrate higher influence of the recirculation with decreasing incidence angle.

Energy characteristics of protons emitted from front/rear foil side again confirm what was discussed earlier. With increasing laser pulse incidence angle (from 45° to 75°), the conversion efficiency (and the energy fluence) as well as the cutoff energy decrease due to reduced laser pulse absorption and increasing hot electron guiding resulting in their enhanced lateral transport. The enhancement of proton energy characteristics for the incidence angle of 45° compared to 30° is caused entirely by a higher laser pulse absorption, a lower level of guided electrons is comparable for both cases. The hot electron guiding along the front foil surface starts to play a significant role in the ion acceleration process for the incidence angles larger than 60°, but even in this case they carry out relatively small part of the laser pulse energy.

6.4 Conclusion

We investigated lateral electron transport in a thin foil caused by hot electron guiding along the foil front surface and hot electron recirculation forth and back, by 2D PIC simulations. While a femtosecond laser pulse is incident on the foil at a large angle ($75°$, $60°$), a part of electrons is confined on the foil front due to generated quasi-static magnetic and electric fields. The confined electrons are accelerated to very high energies exceeding more than 10

times the ponderomotive energy, and transported towards an edge of the foil in the direction of laser wave vector projection onto the foil front surface. This acceleration takes place when the oscillations of electrons trapped in a potential well created by quasi-static fields are in resonance with oscillating laser field - in other words, the resonance condition states that when an electron makes one oscillation, the laser wave propagating along the target surface with phase velocity $v_{ph} > c$ overtakes it exactly by one period.

These guiding and acceleration effects are not observed for smaller incidence angles ($30°$, $45°$). However, the lateral electron transport also takes place for the smaller angles, but the energies of transported electrons are much lower. In this case, the lateral transport is mainly due to multiple recirculation of electrons through the foil. The electrons pass through the target and are reflected in the Debye sheath on the rear surface where the normal component of electron velocity is reversed while the transverse velocity is largely unaltered. Thus, the hot electrons reflux in the foil many times and propagate towards target edges.

We also studied the effect of lateral electron transport on ion acceleration from the foil surfaces. For the largest incidence angle ($75°$), the ions emitted from the foil edge (lateral side) can reach several times higher maximum energy than the ions accelerated from the rear foil surface in the target center, although their total number is rather low.

To clearly observe the effect of the electron guiding along foil front surface on proton acceleration, an artificial boundary condition cooling down recirculated electrons is applied on the rear foil surface. It is shown that the hot electron recirculation forth and back still plays an important role even for very large incidence angles, which are considered for the cone targets used for fast ignition. Therefore, the schemes that reduce looses of recirculating electrons along the cone wall would increase the electron transport efficiency.

This Chapter of thesis presents my theoretical work based on previous theoretical and experimental results. The authors of previous publications studied different aspects of the electron guiding separately. The presented results demonstrate that the number of electrons guided along the foil front surface is limited, although the laser can accelerate a small number of electrons and consequently ions from foil edges to very high energies. This could be a motivation for future experiments.

Chapter 7

Conclusions

7.1 Summary

Laser-plasma interaction physics is of great interest due to its potential in nuclear fusion, producing of fast particles, x-ray radiation, or attosecond laser pulses. In the domain of ultraintense femtosecond laser pulses, much effort is concentrated on ion acceleration. Laser accelerated ions have a number of unique characteristics: the pulse duration is at least three orders of magnitude shorter, the currents are many orders of magnitude higher and the inherent beam emittance is better than that of conventional accelerators. Moreover, accelerating fields in plasmas exceed more than 10000 times the fields in conventional accelerators, thus, there is an intention to substitute large-scale facilities with a lower-cost table-top accelerators based on laser-plasma interaction.

In order to put these accelerators into practice, the produced ion beams have to satisfy very demanding criteria. For example, the treatment of deep-seated tumors requires monoenergetic proton beams with energies about 200 MeV [162]. A large flux of protons with the energy about 10 MeV is required for practical production of radioisotopes for positron emission tomography [163]. The fast ignition scheme [164] requires a proton source with a very small divergence, high total energy, and a short pulse duration. Therefore, significant improvements are necessary in producing of fast particles by laser-plasma interaction.

This thesis deals with one possibility of such improvements - the employment of small-sized targets instead of widely used foils in order to improve the efficiency of ion acceleration and ion energy spectra. We consider interaction of ultrashort intense laser pulses (of intensity $10^{18} - 10^{21}$ $\mathrm{W/cm^2}$ and of a duration in 10's or 100's fs) with such targets, by using two-dimensional particle-in-cell simulations. The simulation results together with theoretical models are compared with recent experiments.

Chapter 2 is devoted to the discussion about previously published theoretical and experimental results related to the subject of this thesis. Firstly, we discussed electron acceleration mechanisms in overdense plasma with a step-like (or very steep) density profile as the electrons mediate the acceleration of ions in targets of solid density by induced electrostatic fields. Due to relativistic laser fields in which free electrons oscillate with velocities close to c, collisional absorption rate is negligible because the collision frequency between plasma particles is proportional to $\sim v^{-3}$. Collisionless absorption mechanisms give rise to the

population of hot electrons with a temperature close to the ponderomotive potential of laser radiation, much higher than the temperature of background electrons. The fast electrons are injected into the target once per laser period by electric component (Brunel vacuum heating) or twice per laser period by magnetic component ($j \times B$ heating) of the Lorentz force. Although the current of propagating hot electrons inside the target strongly exceeds the Alfven limit, the electrons can propagate over large distances as they are almost completely neutralized by the return current of background electrons. When the laser pulse is incident on a planar target under very large angle ($\sim 70^{\circ}$), hot electrons can be guided in a potential well formed by generated quasi-static magnetic and electric fields whose magnitude can reach up to several tenths of the laser fields amplitude. These guided electrons are further accelerated when their oscillation period in the potential well is in resonance with the period of laser fields.

Since the field of nowadays operating lasers is not sufficient to accelerate directly ions to high energies due to their at least 1000 times larger mass-to-charge ratio compared with electrons, the ion acceleration is mediated by hot electrons in targets of sizes higher or comparable with the laser wavelength or by Coulomb force between ions after electron expulsion in clusters. In more detail, ions can be accelerated at the target front side by generated electrostatic field due to electrons pushed into the target by the ponderomotive force (radiation pressure acceleration), or from the rear surface of the target where a sheath layer is formed by hot electrons propagating through the target (target normal sheath acceleration). In clusters, the acceleration mechanism depends on the ratio of the hot electron Debye length to the cluster size. When the ratio is small enough, the acceleration is only driven by the Coulomb explosion of ions as almost all electrons are extracted from the cluster by sufficiently intense laser field. In larger clusters, the Coulomb explosion is mixed together with the ambipolar expansion.

The accelerated ions from thin foils have usually an exponential energy distribution decreasing with a cutoff. In small-size targets, where all target dimensions are comparable with the laser focal spot or smaller, mutual interaction of two ion species lead to a discontinuity in the energy spectra: dips and peaks in light ion energy spectra can be observed. This feature is more pronounced in clusters, where the peak in proton energy distribution function is near the cutoff energy. Previous theory and experiments have shown that the efficiency of ion acceleration depends on hot electron dynamics in the target - it is clearly demonstrated by the enhancement of ion energy due to reduced foil thickness. This enhancement is caused mainly by hot electron recirculation forth and back through the thin foil.

Chapter 3 explains various aspects of particle-in-cell (PIC) method and describes algorithms employed in our two-dimensional particle-in-cell code which is widely used in the frame of this thesis. In the PIC method one calculates the motion of numerical macro-particles of a finite size in the simulation box. Charge and current densities are computed only at certain places of the simulation box, namely on a grid. Maxwell equations are solved to compute electric and magnetic fields on the grid and the fields are consequently interpolated at the position of each macro-particle. It was shown that the macro-particles in the PIC code sample distribution function in the phase space that is considered in the solution of Vlasov equation. However, the numerical solution of Vlasov equation requires, in the most general case, the grid with six dimensions, whereas the PIC method only with three dimensions. In our 2D PIC code, novel efficient algorithms are implemented. Zigzag scheme is

employed for the computation of current densities in order to guarantee an automatic compliance with charge continuity equation. Damping regions are applied for the absorption of outgoing electromagnetic waves. Here, we adopted successfully the recipe described in 1D situation [121].

In Chapter 4, we studied the interaction of femtosecond laser pulses with mass-limited targets, which are defined as the targets having all dimensions comparable with the laser spot size. Due to reduced target dimensions, the mass-limited targets limit the spread of hot electrons and, thus, the electron kinetic energy is transferred to ions more efficiently. We considered the interaction of mass-limited targets of various shapes with one or two ion species. We found via 2D PIC simulations that the optimum transverse target size is about the laser beam diameter. It was demonstrated that the circular target shape is preferred to the rectangular form to obtain the highest energy of accelerated ions. On the other hand, the cylindrical target produces an undesirable divergence of fast ions. In this point of view, a concave foil section could be an ideal target as its employment enhances the absorbed laser energy due to the front surface curvature and allows one, simultaneously, to focus the proton beam at a specific distance determined by the radius of curvature at the rear side of the target and to decrease its divergence afterwards. Mutual interaction of light (usually protons) and heavier ions enables to control the light ion energy spectra. The presence of heavier ions serving as a piston compensates partially for the effect of Coulomb explosion of the fastest light ions originated from the thin surface layer and maintains a narrow light ion energy spectrum for a long time. These results have been published in peer-reviewed journals in four articles [27], [48], [147], [165].

The enhancement of proton energy, laser-to-proton conversion efficiency, and narrower ion angular spread have been observed in recent experiments with thin foil sections of a reduced surface [35]. In this case, transverse target sizes are at least ten times larger than the laser beam width, but still sufficiently small to observe the effect of the increase of ion energy and number with decreasing foil surface, which experimentally confirms our previous theoretical and numerical results. We have demonstrated that the enhancement of proton energy is due to the refluxing of hot electrons laterally from the target edges towards the center, which takes place during the ion acceleration time, if the transverse dimension of the target is small enough. The refluxing produces effective (time-integrated) denser and hotter electron population in the sheath. For the smallest target surface, the hot electron sheath is more homogeneous along the target surface, which explains the narrower ion angular spread.

The interaction of femtosecond laser pulse with a cloud of water microdroplets, the so-called water spray target, is discussed in Chapter 5. Here, the experiment has shown that the proton energy spectra are strongly influenced by the interaction conditions (the laser pulse contrast, the position of the laser focus). With an increasing laser pulse contrast, a narrow sharp peak in the proton energy spectra was observed in the direction of laser pulse propagation, when the laser pulse was focused not exactly in the center, but more to the rear side of the jet, whereas the protons with a broader energy distribution were created when the pulse was focused into the center. The physics of the laser pulse interaction with water spray is rather complex and includes many phenomena (microdroplet ablation by laser prepulse, inhomogeneous target ionization, laser intensity distribution in the spray, recombination and collisional effects in the surrounding target material, etc.). We have carried out numerical simulations of the laser pulse interaction with a water microdroplet of diameter of 100 nm,

which gives an insight into the physics of ion acceleration. Here, the proton energy spectra have different character than in bigger targets - the proton energy distribution function is constant in 2D case and increasing function of the ion energy in 3D case ($\sim \sqrt{\varepsilon_i}$) up to the cutoff energy. Additionally, one can observe a peak in the proton energy spectra at the cutoff energy, which was explained by mutual interaction between protons and oxygen ions. The results have been published in a journal article [26].

Finally, Chapter 6 covers our theoretical study of a lateral hot electron transport in thin foils and the resulting ion acceleration from various foil regions. Two mechanisms of lateral electron transport were discussed - the first is due to hot electron guiding along the foil front surface by generated quasi-static electric and magnetic fields, and the second is caused by the hot electron recirculation (reversing of the normal component of electron velocity when the electron propagating through the foil starts to escape into vacuum, while the transverse velocity is largely unaltered). We found that only a small number of electrons can be guided along the foil surface for large incidence angles (more than $\sim 60°$) of the laser beam on the foil surface, whereas the majority of electrons is laterally transported towards foil edges due to the recirculation through the thin foil. However, electrons guided along the surface can be accelerated to several times higher energy than the recirculating electrons, which enhances energy of accelerated ions from foil edges. These results have been submitted to publication [46].

7.2 Perspectives

This thesis contributes to the search for improvements in the efficiency of ion acceleration in order to put laser-plasma accelerators into practice. Small-size targets significantly enhance the maximum ion energy, the laser-to-proton conversion efficiency, and provide possibilities to control ion energy spectra and the ion beam divergence. Some of our numerical and theoretical results have been confirmed in recent experiments. It has been demonstrated experimentally that the employment of small foil sections leads to three times higher maximum proton energies and even larger increase of the laser-to-proton conversion efficiency compared with foils of the same thickness. However, more experiments are needed to confirm the possibility to control the ion energy spectra in such foil sections, although first results seem to be positive [166]. With increasing computational power, it is also necessary to develop more realistic 3D PIC simulations to reproduce well the scaling of energy characteristics, namely, the conversion efficiency, which is not comparable between experiments and 2D simulations.

Concerning ion acceleration in larger clusters, there should be an effort to include the ionization process into simulations as this could strongly affect the following cluster expansion. Field and collisional ionization have been already included in 1D PIC code [61] available to us. The next step could be the implementation of the ionization in our 2D PIC code in order to study it in clusters. Moreover, in laser interaction with a cloud of such clusters, several open questions arise concerning the influence of laser prepulse, the laser pulse propagation through this cloud of clusters, or recombination and collisional effects in the cloud. These issues are very complicated to simulate, but improved theoretical analysis and some partial numerical simulations would be helpful to understand better these complex phenomena.

The lateral electron transport and resulting ion acceleration are studied only theoretically in this thesis, although experimental data have been published recently on ion emission from foil edges [151] and on ion acceleration from laterally moving electron sheath [167]. However, it would be interesting to realize an experiment on ion acceleration from foil edges, where the laser pulse will be incident on the target surface at a large angle (above 60°), and the laser focal spot will be close to the foil edge, in order to compare maximum energies of ions produced from the rear foil side and from the foil edge. Such experiment will confirm that the surface electron acceleration really exists and will demonstrate a possibility of efficient lateral electron transport in a thin foil or a wire.

Bibliography

[1] G. A. Mourou, C. P. J. Barty, and M. D. Perry, *Ultrahigh-intensity lasers: physics of the extreme on a tabletop*, Physics Today **51**, 22 (1998).

[2] G. A. Mourou, T. Tajima, S. V. Bulanov, *Optics in the relativistic regime*, Reviews of Modern Physics **78**, 309 (2006).

[3] Y. Sentoku, T. E. Cowan, A. Kemp, and H. Ruhl, *High energy proton acceleration in interaction of short laser pulse with dense plasma target*, Physics of Plasmas **10**, 2009 (2003).

[4] X. Zhang, B. Shen, X. Li, Z. Jin, F. Wang, and M. Wen, *Efficient GeV ion generation by ultraintense circularly polarized laser pulse*, Physics of Plasmas **14**, 123108 (2007).

[5] A. P. L. Robinson, M. Zepf, S. Kar, R. G. Evans, and C. Bellei, *Radiation pressure acceleration of thin foils with circularly polarized laser pulses*, New Journal of Physics **10**, 013021 (2008).

[6] O. Klimo, J. Psikal, J. Limpouch, and V. T. Tikhonchuk, *Monoenergetic ion beams from ultrathin foils irradiated by ultrahigh-contrast circularly polarized laser pulses*, Physical Review Special Topics - Accelerators and Beams **11**, 031301 (2008).

[7] S. P. Hatchett, C. G. Brown, T. E. Cowan, E. A. Henry, J. S. Johnson, M. H. Key, J. A. Koch, A. B. Langdon, B. F. Lasinski, R. W. Lee, A. J. Mackinnon, D. M. Pennington, M. D. Perry, T. W. Phillips, M. Roth, T. C. Sangster, M. S. Singh, R. A. Snavely, M. A. Stoyer, S. C. Wilks, and K. Yasuike, *Electron, photon, and ion beams from the relativistic interaction of Petawatt laser pulses with solid targets*, Physics of Plasmas **7**, 2076 (2000).

[8] S. C. Wilks, A. B. Langdon, T. E. Cowan, M. Roth, M. Singh, S. Hatchett, M. H. Key, D. Pennington, A. MacKinnon, and R. A. Snavely, *Energetic proton generation in ultra-intense laser-solid interactions*, Physics of Plasmas **8**, 542 (2001).

[9] P. McKenna, K. W. D. Ledingham, J. M. Yang, L. Robson, T. McCanny, S. Shimizu, R. J. Clarke, D. Neely, KS. Spohr, R. Chapman, R. P. Singhal, K. Krushelnick, M. S. Wei, and P. A. Norreys, *Characterization of proton and heavier ion acceleration in ultrahigh-intensity laser interactions with heated target foils*, Physical Review E **70**, 036405 (2004).

[10] R. A. Snavely, M. H. Key, S. P. Hatchett, T. E. Cowan, M. Roth, T. W. Phillips, M. A. Stoyer, E. A. Henry, T. C. Sangster, M. S. Singh, S. C. Wilks, A. J. Mackinnon, A. Offenberger, D. M. Penning, K. Yasuike, A. B. Langdon, B. F. Lasinski, J. Johnson, M. D. Perry, and E. M. Campbell, *Intense high-energy proton beams from petawatt-laser irradiation of solids*, Physical Review Letters **85**, 2945 (2000).

[11] M. Hegelich, S. Karsch, G. Pretzler, D. Habs, K. Witte, W. Guenther, M. Allen, A. Blazevic, J. Fuchs, J. C. Gauthier, M. Geissel, P. Audebert, T. Cowan, and M. Roth, *MeV ion jets from short-pulse-laser interaction with thin foils*, Physical Review Letters **89**, 085002 (2002).

[12] B. M. Hegelich, B. Albright, P. Audebert, A. Blazevic, E. Brambrink, J. Cobble, T. Cowan, J. Fuchs, J. C. Gauthier, C. Gautier, M. Geissel, D. Habs, R. Johnson, S. Karsch, A. Kemp, S. Letzring, M. Roth, U. Schramm, J. Schreiber, K. J. Witte, and J. C. Fernandez, *Spectral properties of laser-accelerated mid-Z MeV/u ion beams*, Physics of Plasmas **12**, 056314 (2005).

[13] H. Schwoerer, J. Magill, and B. Beleites, *Lasers and nuclei: applications of ultrahigh intensity lasers in nuclear science* Springer-Verlag, Berlin, Germany (2006).

[14] H. Schwoerer, S. Pfotenhauer, O. Jackel, K.-U. Amthor, B. Liesfeld, W. Ziegler, R. Sauerbrey, K. W. D. Ledingham, and T. Esirkepov, *Laser-plasma acceleration of quasi-monoenergetic protons from microstructured targets*, Nature **439**, 445 (2006).

[15] B. M. Hegelich, B. J. Albright, J. Cobble, K. Flippo, S. Letzring, M. Pafferr, H. Ruhl, J. Schreiber, R. K. Schulze, and J. C. Fernandez, *Laser acceleration of quasi-monoenergetic MeV ion beams*, Nature **439**, 441 (2006).

[16] Y. Oishi, T. Nauyuki, T. Fujii, Y. Takizawa, X. Wang, T. Yamazaki, K. Nemoto, T. Kayoji, T. Sekiya, K. Horioka, Y. Okano, Y. Hironaka, K. G. Nakamura, K. Kondo, and A. A. Andreev, *Dependence on laser intensity and pulse duration in proton acceleration by irradiation of ultrashort laser pulses on a Cu foil target*, Physics of Plasmas **12**, 073102 (2005).

[17] J. Fuchs, P. Antici, E.D'Humieres, E. Lefebvre, M. Borghesi, E. Brambrink, C. A. Cecchetti, M. Kaluza, V. Malka, M. Manclossi, S. Meyroneinc, P. Mora, J. Schreiber, T. Toncian, H. Pepin, and P. Audebert, *Laser-driven proton scaling laws and new paths towards energy increase*, Nature Physics **2**, 48 (2006).

[18] L. Robson, P. T. Simpson, R. J. Clarke, K. W. D. Ledingham, F. Lindau, O. Lundh, T. McCanny, P. Mora, D. Neely, C. G. Wahlstrom, M. Zepf, and P. McKenna, *Scaling of proton acceleration driven by petawatt-laser-plasma interactions*, Nature Physics **3**, 58 (2007).

[19] S. Karsch, S. Dusterer, H. Schwoerer, F. Ewald, D. Habs, M. Hegelich, G. Pretzler, A. Pukhov, K. Witte, and R. Sauerbrey, *High-intensity laser induced ion acceleration from heavy-water droplets*, Physical Review Letters **91**, 015001 (2003).

[20] S. Busch, M. Schnurer, M. Kalashnikov, H. Schonnagel, H. Stiel, P. V. Nickles, W. Sandner, S. Ter-Avetisyan, V. Karpov, and U. Vogt, *Ion acceleration with ultrafast lasers*, Applied Physics Letters **82**, 3354 (2003).

[21] S. Ter-Avetisyan, M. Schnurer, S. Busch, E. Risse, P. V. Nickles, and W. Sandner, *Spectral dips in ion emission emerging from ultrashort laser-driven plasmas*, Physical Review Letters **93**, 155006 (2004).

[22] S. Ter-Avetisyan, M. Schnurer, P. V. Nickles, M. Kalashnikov, E. Risse, T. Sokollik, W. Sandner, A. Andreev, and V. Tikhonchuk, *Quasimonoenergetic deuteron bursts produced by ultraintense laser pulses*, Physical Review Letters **96**, 145006 (2006).

[23] M. Schnurer, S. Ter-Avetisyan, S. Busch, E. Risse, M. P. Kalashnikov, W. Sandner, and P. Nickles, *Ion acceleration with ultrafast laser driven water droplets*, Laser and Particle Beams **23**, 337 (2005).

[24] P. V. Nickles, S. Ter-Avetisyan, M. Schnurer, T. Sokollik, W. Sandner, J. Schreiber, D. Hilscher, U. Jahnke, A. Andreev, and V. Tikhonchuk, *Review of ultrafast ion acceleration experiments in laser plasma at Max Born Institute*, Laser and Particle Beams **25**, 347 (2007).

[25] A. V. Brantov, V. T. Tikhonchuk, O. Klimo, D. V. Romanov, S. Ter-Avetisyan, M. Schnurer, T. Sokollik, and P. V. Nickles, *Quasi-mono-energetic ion acceleration from a homogeneous composite target by an intense laser pulse*, Physics of Plasmas **13**, 122705 (2006).

[26] S. Ter-Avetisyan, M. Schnurer, P. V. Nickles, M. B. Smirnov, W. Sandner, A. Andreev, K. Platonov, J. Psikal, and V. Tikhonchuk, *Laser proton acceleration in a water spray target*, Physics of Plasmas **15**, 083106 (2008).

[27] J. Psikal, V. T. Tikhonchuk, J. Limpouch, A. A. Andreev, and A. V. Brantov, *Ion acceleration by femtosecond laser pulses in small multispecies targets*, Physics of Plasmas **15**, 053102 (2008).

[28] T. Nakamura, S. Kato, H. Nagatomo, and K. Mima, *Surface-magnetic-field and fast-electron current-layer formation by ultraintense laser irradiation*, Physical Review Letters **93**, 265002 (2004).

[29] M. Chen, Z. M. Sheng, and J. Zhang, *On the angular distribution of fast electrons generated in intense laser interaction with solid targets*, Physics of Plasmas **13**, 014504 (2006).

[30] Y. T. Li, X. H. Yuan, M. H. Xu, Z. Y. Zheng, Z. M. Sheng, M. Chen, Y. Y. Ma, W. X. Liang, Q. Z. Yu, Y. Zhang, F. Liu, Z. H. Wang, Z. Y. Wei, W. Zhao, Z. Jin, and J. Zhang, *Observation of a fast electron beam emitted along the surface of a target irradiated by intense femtosecond laser pulses*, Physical Review Letters **96**, 165003 (2006).

[31] Y. Y. Ma, Z. M. Sheng, Y. T. Li, J. Zhang, X. H. Yuan, M. H. Xu, Z. Y. Zheng, W. W. Chang, M. Chen, and J. Zheng, *Preplasma effects on the emission directions of energetic electrons in relativistic laser–solid interactions*, Journal of Plasma Physics **72**, 1269 (2006).

[32] H. Habara, K. Adumi, T. Yabuuchi, T. Nakamura, Z. L. Chen, M. Kashihara, R. Kodama, K. Kondo, G. R. Kumar, L. A. Lei, T. Matsuoka, K. Mima, and K. A. Tanaka, *Surface acceleration of fast electrons with relativistic self-focusing in pre-formed plasma*, Physical Review Letters **97**, 095004 (2006).

[33] X. H. Yuan, Y. T. Li, M. H. Xu, Z. Y. Zheng, Q. Z. Yu, W. X. Liang, Y. Zhang, F. Liu, J. Bernhardt, S. J. Wang, Z. H. Wang, W. J. Ling, Z. Y. Wei, W. Zhao, and J. Zhang, *Effective fast electron acceleration along the target surface*, Optics Express **16**, 81 (2008).

[34] T. Nakamura, K. Mima, H. Sakagami, and T. Johzaki, *Electron surface acceleration on a solid capillary target inner wall irradiated with ultraintense laser pulses*, Physics of Plasmas **14**, 053112 (2007).

[35] S. Buffechoux, K. Ziel, M. Nakatsutsumi, L. Romagnani, A. Andreev, J. Psikal, M. Amin, P. Antici T. Burris, E. D'Humieres, S. Fourmaux, S. Gaillard, S. Kraft, A. Mancic, G. Sarri, U. Schramm, M. Tampo, V. Tikhonchuk, H. Pepin, P. Audebert, O. Willi, T. E. Cowan, M. Borghesi, and J. Fuchs, *Enhanced laser-driven proton-acceleration induced by transverse refluxing of hot electrons in limited mass targets*, Physical Review Letters, submitted (2009).

[36] T. Esirkepov, M. Borghesi, S. V. Bulanov, G. Mourou, and T. Tajima, *Highly efficient relativistic-ion generation in the laser piston regime*, Physical Review Letters **92**, 175003 (2004).

[37] L. Yin, B. J. Albright, B. M. Hegelich, and J. C. Fernandez, *GeV laser ion acceleration from ultrathin targets: The laser break-out afterburner*, Laser and Particle Beams **24**, 291 (2006).

[38] B. Qiao, M. Zepf, M. Borghesi, and M. Geissler, *Stable GeV ion-beam acceleration from thin foils by circularly polarized laser pulses*, Physical Review Letters **102**, 145002 (2009).

[39] A. J. MacKinnon, Y. Sentoku, P. K. Patel, D. W. Price, S. Hatchett, M. H. Key, C. Andersen, R. Snavely, and R. R. Freeman, *Enhancement of proton acceleration by hot-electron recirculation in thin foils irradiated by ultraintense laser pulses*, Physical Review Letters **88**, 215006 (2002).

[40] D. Neely, P. Foster, A. Robinson, F. Lindau, O. Lundh, A. Persson, C.-G. Wahlstrom, and P. McKenna, *Enhanced proton beams from ultrathin targets driven by high contrast laser pulses*, Applied Physics Letters **89**, 021502 (2006).

[41] T. Ceccotti, A. Levy, H. Popescu, F. Reau, P. D'Oliveira, P. Monot, J. P. Geindre, E. Lefebvre, and Ph. Martin, *Proton acceleration with high-intensity, ultra-high-contrast laser pulses*, Physical Review Letters **99**, 185002 (2007).

[42] A. P. L. Robinson, A. R. Bell, and R. J. Kingham, *Effect of target composition on proton energy spectra in ultraintense laser-solid interactions*, Physical Review Letters **96**, 035005 (2006).

[43] A. P. L. Robinson and P. Gibbon, *Production of proton beams with narrow-band energy spectra from laser-irradiated ultrathin foils*, Physical Review E **75**, 015401 (2007).

[44] A. P. L. Robinson, P. Gibbon, S. M. Pfotenhauer, O. Jackel, and J. Polz, *Scaling of the proton density reduction scheme for the laser acceleration of proton beams with a narrow energy spread*, Plasma Physics and Controlled Fusion **51**, 024001 (2009).

[45] C. Stenz and V. Tikhonchuk, *Ultraintense laser-plasma interaction*, lecture notes (in french), University of Bordeaux 1, Talence, France (2008).

[46] J. Psikal, V. T. Tikhonchuk, J. Limpouch, and O. Klimo, *Lateral hot electron transport and ion acceleration in femtosecond laser pulse interaction with thin foils*, Physics of Plasmas, submitted (2009).

[47] J. Psikal, *Simulations of laser-plasma interactions with two-dimensional particle-in-cell code*, Master thesis (in czech), Czech Technical University in Prague, Czechia (2006).

[48] J. Psikal, J. Limpouch, S. Kawata, and A. A. Andreev, *PIC simulations of femtosecond interactions with mass-limited targets*, Czechoslovak Journal of Physics **56**, B515 (2006).

[49] W. L. Kruer, *The physics of laser plasma interaction*, Addison-Wesley, New York, USA (1988).

[50] S. Eliezer, *The interaction of high-power lasers with plasmas*, Institute of Physics Publishing, Bristol, UK, 2002.

[51] P. M. Bellan, *Fundamentals of plasma physics*, Cambridge University Press, Cambridge, UK (2006).

[52] P. Mora, *Introduction to laser-plasma physics*, lecture notes (in french), Ecole polytechnique, Palaiseau, France (2006).

[53] B. Quesnel and P. Mora, *Theory and simulation of the interaction of ultraintense laser pulses with electrons in vacuum*, Physical Review E **58**, 3719 (1998).

[54] P. Gibbon, *Short pulse laser interactions with matter: An introduction*, Imperial College Press, London, UK (2005).

[55] P. Fiala, *Principles of physical optics*, lecture notes (in czech), Czech Technical University in Prague, Czechia (1999).

[56] P. Mora, *Physics of relativistic plasmas*, Conference proceedings *Atoms and Plasmas in Super-Intense Laser Fields* edited by D. Batani, C. J. Joachain, and S. Martellucci, p. 245, Italian Physical Society, Bologna, Italy (2004)

[57] S. Guerin, P. Mora, J. C. Adam, A. Heron, and G. Laval, *Propagation of ultraintense laser pulses through overdense plasma layers*, Physics of Plasmas **3**, 2693 (1996).

[58] G.-Z. Sun, E. Ott, Y. C. Lee, and P. Guzdar, *Self-focusing of short intense pulses in plasmas*, Physics of Fluids **30**, 526 (1987).

[59] A. Pukhov, *Strong field interaction of laser radiation*, Reports on Progress in Physics **66**, 47 (2003).

[60] K. H. Hong, B. Hou, J. A. Nees, E. Power, and G. A. Mourou, *Generation and measurement of ¿ 10(8) intensity contrast ratio in a relativistic kHz chirped-pulse amplified laser*, Applied Physics B - Lasers and Optics **81**, 447 (2005).

[61] O. Klimo, *Simulations of ultrashort-pulse laser solid-target interactions*, PhD thesis, Czech Technical University in Prague, Czechia (2007).

[62] D. F. Price, R. M. More, R. S. Walling, G. Guethlein, R. L. Shepherd, R. E. Stewart, and W. E. White, *Absorption of ultrashort laser-pulses by solid targets heated rapidly to temperatures 1-1000 eV*, Physical Review Letters **75**, 252 (1995).

[63] C. Thaury, F. Quere, J.-P. Geindre, A. Levy, T. Ceccotti, P. Monot, M. Bougeard, F. Reau, P. D'Oliveira, P. Audebert, R. Marjoribanks, P. H. Martin, *Plasma mirrors for ultrahigh-intensity optics*, Nature Physics **3**, 424 (2007).

[64] A. Levy, T. Ceccotti, P. D'Oliveira, F. Reau, M. Perdrix, F. Quere, P. Monot, M. Bougeard, H. Lagadec, P. Martin, J.-P. Geindre, and P. Audebert, *Double plasma mirror for ultrahigh temporal contrast ultraintense laser pulses*, Optics Letters **32**, 310 (2007).

[65] V. Tikhonchuk, *Plasma physics - kinetic models*, lecture notes (in french), University of Bordeaux 1, Talence, France (2007).

[66] P. Mora, *Plasma Expansion into a Vacuum*, Physical Review Letters **90**, 185002 (2003).

[67] V. T. Tikhonchuk, A. A. Andreev, S. G. Bochkarev, and V. Yu. Bychenkov, *Ion acceleration in short-laser-pulse interaction with solid foils*, Plasma Physics and Controlled Fusion **47**, B869 (2005).

[68] H. Chen, S. C. Wilks, W. L. Kruer, P. K. Patel, and R. Shepherd, *Hot electron energy distributions from ultraintense laser solid interactions*, Physics of Plasmas **16**, 020705 (2009).

[69] Z. M. Sheng, Y. Sentoku, K. Mima, J. Zhang, W. Yu, and J. Meyer-ter-Vehn, *Angular distributions of fast electrons, ions, and bremstrahlung x/γ-rays in intense laser interaction with solid targets*, Physical Review Letters **85**, 5340 (2000).

[70] D. F. Cai, Y. Q. Gu, Z. J. Zheng, T. S. Wen, S. T. Chunyu, Z. B. Wang, and X. D. Yang, *Experimental study for angular distribution of the hot electrons generated by femtosecond laser interaction with solid targets*, Physics of Plasmas **10**, 3265 (2003).

[71] J. Zhang, Y. T. Li, Z. M. Sheng, Z. Y. Wei, Q. L. Dong, and X. Lu, *Generation and propagation of hot electrons in laser-plasmas*, Applied Physics B **80**, 957 (2005).

[72] Z. Li, H. Daido, A. Fukumi, S. V. Bulanov, A. Sagisaka, K. Ogura, A. Yogo, M. Nishiuchi, S. Orimo, M. Mori, Y. Oishi, T. Nayuki, T. Fujii, K. Nemoto, S. Nakamura, A. Noda, I. W. Choi, J. H. Sung, D. K. Ko, and J. Lee, *Protons and electrons generated from a 5-μm thick copper tape target irradiated by s-, circularly-, and p-polarized 55-fs laser pulses*, Physics Letters A **369**, 483 (2007).

[73] R. Kodama, P. A. Norreys, K. Mima, A. E. Dangor, R. G. Evans, H. Fujita, Y. Kitagawa, K. Krushelnick, T. Miyakoshi, N. Miyanaga, T. Norimatsu, S. J. Rose, T. Shozaki, K. Shigemori, A. Sunahara, M. Tampo, K. A. Tanaka, Y. Toyama, T. Yamanaka, and M. Zepf, *Fast heating of ultrahigh-density plasma as a step towards laser fusion ignition*, Nature **412**, 798 (2001).

[74] J. J. Santos, F. Amiranoff, S. D. Baton, L. Gremillet, M. Koenig, E. Martinolli, M. Rabec Le Gloahec, C. Rousseaux, D. Batani, A. Bernardinello, G. Greison, and T. Hall, *Fast electron transport in ultraintense laser pulse interaction with solid targets by rear-side self-radiation diagnostics*, Physical Review Letters **89**, 025001 (2002).

[75] J. Fuchs, T. E. Cowan, P. Audebert, H. Ruhl, L. Gremillet, A. Kemp, M. Allen, A. Blazevic, J.-C. Gauthier, M. Geissel, M. Hegelich, S. Karsch, P. Parks, M. Roth, Y. Sentoku, R. Stephens, and E. M. Campbell, *Spatial uniformity of laser-accelerated ultrahigh-current MeV electron propagation in metals and insulators*, Physical Review Letters **91**, 255002 (2003).

[76] R. B. Stephens, R. A. Snavely, Y. Aglitskiy, F. Amiranoff, C. Andersen, D. Batani, S. D. Baton, T. Cowan, R. R. Freeman, T. Hall, S. P. Hatchett, J. M. Hill, M. H. Key, J. A. King, J. A. Koch, M. Koenig, A. J. MacKinnon, K. L. Lancaster, E. Martinolli, P. Norreys, E. Perelli-Cippo, M. Rabec Le Gloahec, C. Rousseaux, J. J. Santos, and F. Scianitti, *K alpha fluorescence measurement of relativistic electron transport in the context of fast ignition*, Physical Review E **69**, 066414 (2004).

[77] A. Debayle, *Theoretical study of ultrahigh intensity laser-produced high current relativistic electron beam transport through solid targets*, PhD thesis, University Bordeaux 1, France (2008).

[78] H. Alfven, *On the motion of cosmic rays in interstellar space*, Physical Review **55**, 425 (1939).

[79] Y. Sentoku, K. Mima, S. Kojima, and H. Ruhl, *Magnetic instability by the relativistic laser pulses in overdense plasmas*, Physics of Plasmas **7**, 689 (2000).

[80] L. O. Silva, R. A. Fonseca, J. W. Tonge, W. B. Mori, and J. M. Dawson, *On the role of the purely transverse Weibel instability in fast ignitor scenarios*, Physics of Plasmas **9**, 2458 (2002).

[81] L. Van Woerkom, K. U. Akli, T. Bartal, F. N. Beg, S. Chawla, C. D. Chen, E. Chowdhury, R. R. Freeman, D. Hey, M. H. Key, J. A. King, A. Link, T. Ma, A. J. MacKinnon, A. G. MacPhee, D. Offermann, V. Ovchinnikov, P. K. Patel, D. W. Schumacher, R. B. Stephens, and Y. Y. Tsui, *Fast electron generation in cones with ultraintense laser pulses*, Physics of Plasmas **15**, 056304 (2008).

[82] A. Pukhov, Z. M. Sheng, and J. Meyer-ter-Vehn, *Particle acceleration in relativistic laser channels*, Physics of Plasmas **6**, 2847 (1999).

[83] G. D. Tsakiris, C. Gahn, and V. K. Tripathi, *Laser induced electron acceleration in the presence of static electric and magnetic fields in a plasma*, Physics of Plasmas **7**, 3017 (2000).

[84] A. Macchi, F. Cattani, T. V. Liseykina, and F. Cornolti, *Laser acceleration of ion bunches at the front surface of overdense plasmas*, Physical Review Letters **94**, 165003 (2005).

[85] J. Fuchs, Y. Sentoku, E. D'Humieres, T. E. Cowan, J. Cobble, P. Audebert, A. Kemp, A. Nikroo, P. Antici, E. Brambrink, A. Blazevic, E. M. Campbell, J. C. Fernandez, J.-C. Gauthier, M. Geissel, M. Hegelich, S. Karsch, H. Popescu, N. Renard-LeGalloudec, M. Roth, J. Schreiber, R. Stephens, and H. Pepin, *Comparative spectra and efficiencies of ions laser-accelerated forward from the front and rear surfaces of thin solid foils*, Physics of Plasmas **14**, 053105 (2007).

[86] J. Fuchs, Y. Sentoku, S. Karsch, J. Cobble, P. Audebert, A. Kemp, A. Nikroo, P. Antici, E. Brambrink, A. Blazevic, E. M. Campbell, J. C. Fernandez, J.-C. Gauthier, M. Geissel, M. Hegelich, H. Pepin, H. Popescu, N. Renard-LeGalloudec, M. Roth, J. Schreiber, R. Stephens, and T. E. Cowan, *Comparison of laser ion acceleration from the front and rear surfaces of thin foils*, Physical Review Letters **94**, 045004 (2005).

[87] K. Flippo, B. M. Hegelich, B. J.Albright, L. Yin, D. C. Gautier, S. Letzring, M. Schollmeier, J. Schreiber, R. Schulze, and J. C. Fernandez, *Laser-driven ion accelerators: Spectral control, monoenergetic ions and new acceleration mechanisms*, Laser and Particle Beams **25**, 3 (2007).

[88] B. M. Hegelich, *Acceleration of heavy ions to MeV/nucleon energies by ultrahigh-intensity lasers*, PhD thesis, Ludwig-Maximilians Universitat, Munchen (2002).

[89] P. Mora, *Thin-foil expansion into a vacuum*, Physical Review E **72**, 056401 (2005).

[90] M. Passoni and M. Lontano, *Theory of light-ion acceleration driven by a strong charge separation*, Physical Review Letters **101**, 115001 (2008).

[91] A. J. Kemp and H. Ruhl, *Multispecies ion acceleration off laser-irradiated water droplets*, Physics of Plasmas **12**, 033105 (2005).

[92] V. Yu. Bychenkov, V. N. Novikov, D. Batani, V. T. Tikhonchuk, and S. G. Bochkarev, *Ion acceleration in expanding multispecies plasmas*, Physics of Plasmas **11**, 3244 (2004).

[93] P. Antici, J. Fuchs, M. Borghesi, L. Gremillet, T. Grismayer, Y. Sentoku, E. D'Humieres, C. A. Cecchetti, A. Mancic, A. C. Pipahl, T. Toncian, O. Willi, P. Mora, and P. Audebert, *Hot an cold electron dynamics following high-intensity laser matter interaction*, Physical Review Letters **101**, 105004 (2008).

[94] M. Schollmeier, M. Roth, A. Blazevic, E. Brambrink, J. A. Cobble, J. C. Fernandez, K. A. Flippo, D. C. Gautier, D. Habs, K. Harres, B. M. Hegelich, T. Hessling, D. H. Hoffmann, S. Letzring, F. Nurnberg, G. Schaumann, J. Schreiber, and K. Witte, *Laser ion acceleration with micro-grooved targets*, Nuclear Instruments and Methods in Physics Research A **577**, 186 (2007).

[95] A. P. L. Robinson, D. Neely, P. McKenna, and R. G. Evans, *Spectral control in proton acceleration with multiple laser pulses*, Plasma Physics and Controlled Fusion **49**, 373 (2007).

[96] S. Ter-Avetisyan, M. Schnurer, R. Polster, P. V. Nickles, and W. Sandner, *First demonstration of collimation and monochromatisation of a laser accelerated proton burst*, Laser and Particle Beams **26**, 637 (2008).

[97] J. Schreiber, F. Bell, F. Gruner, U. Schramm, M. Geissler, M. Schnurer, S. Ter-Avetisyan, B. M. Hegelich, J. Cobble, E. Brambrink, J. Fuchs, P. Audebert, and D. Habs, *Analytical model for ion acceleration by high-intensity laser pulses*, Physical Review Letters **97**, 045005 (2006).

[98] R. Nuter, L. Gremillet, P. Combis, M. Drouin, E. Lefebvre, A. Flacco, and V. Malka, *Influence of a preplasma on electron heating and proton acceleration in ultraintense laser-foil interaction*, Journal of Applied Physics **104**, 103307 (2008).

[99] M. Roth, A. Blazevic, M. Geissler, T. Schlegel, T. E. Cowan, M. Allen, J.-C. Gauthier, P. Audebert, J. Fuchs, J. Meyer-ter-Vehn, M. Hegelich, S. Karsch, and A. Pukhov, *Energetic ions generated by laser pulses: A detailed study on target properties*, Physical Review Special Topics - Accelerators and Beams **5**, 061301 (2002).

[100] M. Kaluza, J. Schreiber, M. I. K. Santala, G. D. Tsakiris, K. Eidmann, J. Meyer-ter-Vehn, and K. J. Witte, *Influence of the laser prepulse on proton acceleration in thin-foil experiments*, Physical Review Letters **93**, 045003 (2004).

[101] K. Nishihara, H. Amitani, M. Murakami, S. V. Bulanov, and T. Zh. Esirkepov, *High energy ions generated by laser driven Coulomb explosion of cluster*, Nuclear Instruments and Methods in Physics Research A **464**, 98 (2001).

[102] B. N. Breizman, A. V. Arefiev, and M. V. Fomytskyi, *Nonlinear physics of laser-irradiated microclusters*, Physics of Plasmas **12**, 056706 (2005).

[103] T. Ditmire, J. Zweiback, V. P. Yanovsky, T. E. Cowan, G. Hays, and K. B. Wharton, *Nuclear fusion from explosions of femtosecond laser-heated deuterium clusters*, Nature **398**, 489 (1999).

[104] G. Grillon, Ph. Balcou, J.-P. Chambaret, D. Hulin, J. Martino, S. Moustaizis, L. Notebaert, M. Pittman, Th. Pussieux, A. Rousse, J.-Ph. Rousseau, S. Sebban, O. Sublemontier, and M. Schmidt, *Deuterium-deuterium fusion dynamics in low-density molecular-cluster jets irradiated by intense ultrafast laser pulses*, Physical Review Letters **89**, 065005 (2002).

[105] M. Hohenberger, D. R. Symes, K. W. Madison, A. Sumeruk, G. Dyer, A. Edens, W. Grigsby, G. Hays, M. Teichmann, and T. Ditmire, *Dynamic acceleration effects in explosions of laser-irradiated heteronuclear clusters*, Physical Review Letters **95**, 195003 (2005).

[106] M. Murakami and M. M. Basko, *Self-similar solution of finite-size non-quasi-neutral plasmas into vacuum: Relation to the problem of ion acceleration*, Physics of Plasmas **13**, 012105 (2006).

[107] M. Murakami and M. Tanaka, *Nanocluster explosions and quasimonoenergetic spectra by homogeneously distributed impurity ions*, Physics of Plasmas **15**, 082702 (2008).

[108] T. Nakamura and S. Kawata, *Origin of protons accelerated by an intense laser and the dependence of their energy on the plasma density*, Physical Review E **67**, 026403 (2003).

[109] J. Psikal, *A two-dimensional particle-in-cell code for the simulation of interaction between laser radiation and plasma*, research project, Czech Technical University in Prague, Czechia (2005).

[110] C. K. Birdsall and A. B. Langdon, *Plasma Physics via Computer Simulation*, McGraw-Hill, New York, USA (1985).

[111] B.-N. Jiang, J. Wu, and L. A. Povinelli, *The origin of spurious solutions in computational electromagnetics*, Journal of Computational Physics **125**, 104 (1996).

[112] P. Hillion, *Beware of Maxwell's Divergence Equations*, Journal of Computational Physics **132**, 154 (1997).

[113] J. Villasenor, and O. Buneman, *Rigorous charge conservation for local electromagnetic field solvers*, Computer Physics Communications **69**, 306 (1992).

[114] T. Zh. Esirkepov, *Exact charge conservation scheme for particle-in-cell simulation with an arbitrary form-factor*, Computer Physics Communications **135**, 144 (2001).

[115] T. Umeda, Y. Omura, T. Tominaga, and H. Matsumoto, *A new charge conservation method in electromagnetic particle-in-cell simulations*, Computer Physics Communications **156**, 73-85 (2003).

[116] K. S. Yee, *Numerical solution of initial boundary value problems involving Maxwell's equations in isotropic media*, IEEE Transaction on Antennas Propagation **14**, 302 (1966).

[117] R. Lichters, R. E. W. Pfund, and J. Meyer-ter-Vehn, *LPIC++, a parallel one-dimensional relativistic electromagnetic particle-in-cell code for simulating laser-plasma interaction*, Max Planck Institute, Garching, Germany (1997), http://www.lichters.net/work.html.

[118] P. Gibbon, A. Andreev, E. Lefebvre, G. Bonnaud, H. Ruhl, J. Delettrez, and A. R. Bell, *Calibration of one-dimensional boosted kinetic codes for modeling high-intensity laser-solid interactions*, Physics of Plasmas **6**, 947 (1999).

[119] P. Kulhanek, *Particle and field solvers in PM models*, Czechoslovak Journal of Physics **50**, 239-244 (2000).

[120] J. Limpouch, O. Klimo, V. Bina, and S. Kawata, *Numerical studies on the ultrashort pulse K-α emission sources based on femtosecond laser-target interactions*, Laser and Particle Beams **22**, 147 (2004).

[121] T. Umeda, Y. Omura, and H. Matsumoto, *An improved masking method for absorbing boundaries in electromagnetic particle simulations*, Computer Physics Communications **137**, 286 (2001).

[122] B. Barney, *OpenMP tutorial*, https://computing.llnl.gov/tutorials/openMP.

[123] O. Coulaud, M. Dussere, P. Henon, E. Lefebvre, and J. Roman, *Optimization of a kinetic laser-plasma interaction code for large parallel systems*, Parallel Computing **29**, 1175 (2003).

[124] M. Geissler, J. Schreiber, and J. Meyer-Ter-Vehn, *Bubble acceleration of electrons with few-cycle laser pulses*, New Journal of Physics **8**, 186 (2006).

[125] J. P. Verboncoeur, A. B. Langfon, and N. T. Gladd, *An object-oriented electromagnetic PIC code*, Computer Physics Communications **87**, 199 (1995).

[126] R. A. Fonseca, L. O. Silva, F. S. Tsung, V. K. Decyk, W. Lu, C. Ren, W. B. Mori, S. Deng, S. Lee, T. Katsouleas, and J. C. Adam, *OSIRIS: A three-dimensional, fully relativistic particle-in-cell code for modelling plasma based accelerators*, Computational Science - ICCS 2002 Proceedings, 342 (2002).

[127] A. Pukhov, *Three-dimensional electromagnetic relativistic particle-in-cell code VLPL (Virtual Laser Plasma Lab)*, Journal of Plasma Physics **61**, 425 (1999).

[128] C. Nieter and J. R. Cary, *VORPAL: a versatile plasma simulation code*, Journal of Computational Physics **196**, 448 (2004).

[129] M. Schnurer, S. Ter-Avetisyan, P. V. Nickles, and A. A. Andreev, *Influence of target system on the charge state, number, and spectral shape of ion beams accelerated by femtosecond high-intensity laser pulses*, Physics of Plasmas **14**, 033101 (2007).

[130] S. Fujioka, H. Nishimura, K. Nishihara, M. Murakami, Y. G. Kang, Q. Gu, K. Nagai, T. Norimatsu, N. Miyanaga, Y. Izawa, K. Mima, Y. Shimada, A. Sunahara, and H. Furukawa, *Properties of ion debris emitted form laser-produced mass-limited tin plasmas for extreme ultraviolet light source applications*, Applied Physics Letters **87**, 241503 (2005).

[131] M. Anand, P. Gibbon, and M. Krishnamurthy, *Laser absorption in microdroplet plasmas*, EPL **80**, 25002 (2007).

[132] http://www.extreme-light-infrastructure.eu

[133] T. Zh. Esirkepov, S. V. Bulanov, K. Nishihara, T. Tajima, F. Pegoraro, V. S. Khoroshkov, K. Mima, H. Daido, Y. Kato, Y. Kitagawa, K. Nagai, and S. Sakabe, *Proposed double-layer target for the generation of high-quality laser-accelerated ion beams*, Physical Review Letters **89**, 175003 (2002).

[134] S. V. Bulanov, T. Z. Esirkepov, V. S. Khoroshkov, A. V. Kunetsov, and F. Pegoraro, *Oncological hadrontherapy with laser ion accelerators*, Physics Letters A **299**, 240 (2002).

[135] L. Romagnani, J. Fuchs, M. Borghesi, P. Antici, P. Audebert, F. Ceccherini, T. Cowan, T. Grismayer, S. Kar, A. Macchi, P. Mora, G. Pretzler, A. Schiavi, T. Toncian, and O. Willi, *Dynamics of electric fields driving the laser acceleration of multi-MeV protons*, Physical Review Letters **95**, 195001 (2005).

[136] S. D. Baton, M. Koenig, P. Guillou, B. Loupias, A. Benuzzi-Mounaix, J. Fuchs, Ch. Rousseaux, L. Gremillet, D. Batani, A.Morace, M. Nakatsutsumi, R. Kodama, and Y. Aglitskiy, *Relativistic electron transport and confinement within charge-insulated, mass-limited targets*, High Energy Density Physics **3**, 358 (2007).

[137] N. V. Klassen, L. Zwan, and J. Cygler, *GafChromic MD-55: Investigated as a precision dosimeter*, Medical Physics **24**, 1924 (1997).

[138] A. Mancic, J. Fuchs, P. Antici, S. A. Gaillard, and P. Audebert, *Absolute calibration of photostimulable image plate detectors used as (0.5-20 MeV) high-energy proton detectors*, Review of Scientific Instruments **79**, 073301 (2008).

[139] J. F. Ziegler, J. P. Biersack, and U. Littmark, *The stopping and range of ions in solids*, Pergamon Press, New York, USA (1996).

[140] P. Gibbon and A. R. Bell, *Collisionless absorption in sharp-edged plasmas*, Physical Review Letters **68**, 1535 (1992).

[141] E. Brambrink, M. Roth, A. Blazevic, and T. Schlegel, *Modeling of the electrostatic sheath shape on the rear target surface in short-pulse laser-driven proton acceleration*, Laser and Particle Beams **24**, 163 (2006).

[142] M. Roth, E. Brambrink, P. Audebert, M. Basko, A. Blazevic, R. Clarke, J. Cobble, T. E. Cowan, J. Fernandez, J. Fuchs, M. Hegelich, K. Ledingham, L. G. Logan, D. Neely, H. Ruhl, and M. Schollmeier, *Laser accelerated ions in ICF research prospects and experiments*, Plasma Physics and Controlled Fusion **47**, B841 (2005).

[143] P. K. Patel, A. J. Mackinnon, M. H. Key, T. E. Cowan, M. E. Foord, M. Allen, D. F. Price, H. Ruhl, P. T. Springer, and R. Stephens, *Isochoric heating of solid-density matter with an ultrafast proton beam*, Physical Review Letters **91**, 125004 (2003).

[144] M. I. K. Santala, M. Zepf, F. N. Beg, E. L. Clark, A. E. Dangor, K. Krushelnick, M. Tatarakis, I. Watts, K. W. D. Ledingham, T. McCanny, I. Spencer, A. C. Machacek, R. Allott, R. J. Clarke, and P. A. Norreys, *Production of radioactive nuclides by energetic protons generated from intense laser-plasma interactions*, Applied Physics Letters **78**, 19 (2001).

[145] A. Andreev, K. Platonov, and S. Kawata, *Ion acceleration by short high intensity laser pulse in small target sets*, Laser and Particle Beams **27**, 449 (2009).

[146] A. Henig, D. Kiefer, M. Geissler, S. G. Rykovanov, R. Ramis, R. Horlein, J. Osterhoff, Zs. Major, L. Veisz, S. Karsch, F. Krausz, D. Habs, and J. Schreiber, *Laser-driven shock acceleration of ion beams from spherical mass-limited targets*, Physical Review Letters **102**, 095002 (2009).

[147] J. Limpouch, J. Psikal, A. A. Andreev, K. Yu. Platonov, and S. Kawata, *Enhanced laser ion acceleration from mass-limited targets*, Laser and Particle Beams **26**, 225 (2008).

[148] L. O. Silva, M. Marti, J. R. Davies, R. A. Fonseca, Ch. Ren, F. S. Tsung, and W. B. Mori, *Proton shock acceleration in laser-plasma interactions*, Physical Review Letters **92**, 015002 (2004).

[149] S. Ter-Avetisyan, M. Schnurer, and P. V. Nickles, European Patent No. EP 1 574 116 B1 (2007).

[150] S. Ter-Avetisyan, M. Schnurer, H. Stiel, and P. V. Nickles, *A high-density sub-micron liquid spray for laser driven radiation sources*, Journal of Physics D - Applied Physics **36**, 2421 (2003).

[151] P. McKenna, D. C. Caroll, R. J. Clarke, R. G. Evans, K. W. D. Ledingham, F. Lindau, O. Lundh, T. McCanny, D. Neely, A. P. L. Robinson, L. Robson, P. T. Simpson, C.-G. Wahlstrom, and M. Zepf, *Lateral electron transport in high-intensity laser-irradiated foils diagnosed by ion emission*, Physical Review Letters **98**, 145001 (2007).

[152] Y. Sentoku, K. Mima, H. Ruhl, Y. Toyama, R. Kodama, and T. E. Cowan, *Laser light and hot electron micro focusing using a conical target*, Physics of Plasmas **11**, 3083 (2004).

[153] T. Nakamura, H. Sakagami, T. Johzaki, H. Nagatomo, and K. Mima, *Hot electron generation by laser-cone interaction*, Journal de Physique IV **133**, 401 (2006).

[154] T. Nakamura, K. Mima, H. Sakagami, T. Johzaki and H. Nagatomo, *Generation and confinement of high energy electrons generated by irradiation of ultra-intense short laser pulses onto cone targets*, Laser and Particle Beams **26**, 207 (2008).

[155] J. Rassuchine, E. D'Humieres, S. D. Baton, P. Guillou, M. Koenig, M. Chahid, F. Perez, J. Fuchs, P.Audebert, R. Kodama, M. Nakatsutsumi, N. Ozaki, D. Batani, A. Morace, R. Redaelli, L. Gremillet, C. Rousseaux, F. Dorchies, C. Fourment, J. J. Santos, J. Adams, G. Korgan, S. Malekos, S. B. Hansen, R. Shepherd, K. Flippo, S. Gaillard, Y. Sentoku, and T. E. Cowan, *Enhanced hot electron localization and heating in high-contrast ultraintense laser irradiation of microcone targets*, Physical Review E **79**, 036408 (2009).

[156] T. Nakamura, H. Sakagami, T. Johzaki, H. Nagatomo, K. Mima, and J. Koga, *Optimization of cone target geometry for fast ignition*, Physics of Plasmas **14**, 103105 (2007).

[157] R. Kodama, Y. Sentoku, Z. L. Chen, G. R. Kumar, S. P. Hachett, Y. Toyama, T. E. Cowan, R. R. Freeman, J. Fuchs, Y. Izawa, M. H. Key, Y. Kitagawa, K. Kondo, T. Matsuoka, H. Nakamura, M. Nakatsutsumi, P. A. Norreys, T. Norimatsu, R. A. Snavely, R. B. Stephens, M. Tampo, K. A. Tanaka, and T. Yabuuchi, *Plasma devices to guide and collimate a high density of MeV electrons*, Nature **432**, 1005 (2004).

[158] A. L. Lei, L. H. Cao, X. Q. Yang, K. A. Tanaka, R. Kodama, X. T. He, K. Mima, T. Nakamura, T. Norimatsu, W. Yu, and W. Y. Zhang, *Guiding and confining fast electrons by transient electric and magnetic fields with a plasma inverse cone*, Physics of Plasmas **16**, 020702 (2009).

[159] R. B. Campbell, J. S. DeGroot, T. A. Mehlhorn, D. R. Welch, and B. V. Oliver, *Collimation of petawatt laser-generated relativistic electron beams propagating through solid matter*, Physics of Plasmas **10**, 4169 (2003).

[160] A. P. L. Robinson and M. Sherlock, *Magnetic collimation of fast electron produced by ultraintense laser irradiation by structuring the target composition*, Physics of Plasmas **14**, 083105 (2007).

[161] S. Kar, A. P. L. Robinson, D. C. Carroll, O. Lundh, K. Markey, P. McKenna, P. Norreys, and M. Zepf, *Guiding of relativistic electron beams in solid targets by resistively controlled magnetic fields*, Physical Review Letters **102**, 055001 (2009).

[162] U. Linz and J. Alonso, *What will it take for laser driven proton accelerators to be applied to tumor therapy?*, Physical Review Special Topics - Accelerators and Beams **10**, 094801 (2007).

[163] L. Robson, P. McKenna, T. McCanny, K. W. D. Ledingham, J. M. Gillies, and J. Zweit, *High-power laser production of PET isotopes*, in *Lasers and Nuclei: Applications of Ultrahigh Intensity Lasers in Nuclear Science* edited by H. Schwoerer, J. Magill, and B. Beleites, p. 191, Springer-Verlag, Berlin, Germany (2006).

[164] M. Tabak, J. Hammer, M. E. Glinsky, W. L. Kruer, S. C. Wilks, J. Woodworth, E. M. Campbell, M. D. Perry, and R. J. Mason, *Ignition and high-gain with ultrapowerful lasers*, Physics of Plasmas **1**, 1626 (1994).

[165] A. A. Andreev, J. Limpouch, J. Psikal, K. Yu. Platonov, and V. T. Tikhonchuk, *Laser ion acceleration in mass limited targets*, European Physical Journal - Special Topics **175**, 123 (2009).

[166] S. Kar, private communication (2008).

[167] T. Nakamura, K. Mima, S. Ter-Avetisyan, M. Schnuerer, T. Sokollik, P. V. Nickles, and W. Sandner, *Lateral movement of a laser-accelerated proton source on the target's rear surface*, Physical Review E **77**, 036407 (2008).

Publications and Awards

List of publications in peer-reviewed journals

Laser ion acceleration in mass limited targets
A. A. Andreev, J. Limpouch, **J. Psikal**, K. Yu. Platonov, and V. T. Tikhonchuk,
European Physical Journal - Special Topics **175**, 123 (2009)

Laser proton acceleration in a water spray target
S. Ter-Avetisyan, M. Schnurer, P. V. Nickles, M. B. Smirnov, W. Sandner, A. A. Andreev, K. Yu. Platonov, **J. Psikal**, and V. T. Tikhonchuk,
Physics of Plasmas **15**, 083106 (2008)

Enhanced laser ion acceleration from mass-limited targets
J. Limpouch, **J. Psikal**, A. A. Andreev, K. Yu. Platonov, and S. Kawata
Laser and Particle Beams **26**, 225 (2008)

Ion acceleration by femtosecond laser pulses in small multispecies targets
J. Psikal, V. T. Tikhonchuk, J. Limpouch, A. A. Andreev, and A. V. Brantov
Physics of Plasmas **15**, 053102 (2008)

Monoenergetic ion beams from ultrathin foils irradiated by ultrahigh-contrast circularly polarized laser pulses
O. Klimo, **J. Psikal**, J. Limpouch, and V. T. Tikhonchuk
Physical Review Special Topics - Accelerators and Beams **11**, 031301 (2008)

PIC simulations of femtosecond interactions with mass-limited targets
J. Psikal, J. Limpouch, S. Kawata, and A. A. Andreev
Czechoslovak Journal of Physics **56**, B515 (2006)

List of currently submitted articles

Enhanced laser-driven proton acceleration induced by transverse refluxing of hot electrons in limited mass targets
S. Buffechoux, K. Zeil, M. Nakatsutsumi, L. Romagnani, A. Andreev, **J. Psikal**, M. Amin, P. Antici, T. Burris, E. d'Humieres, S. Fourmaux, S. Gaillard, S. Kraft, A. Mancic, G. Sarri, U. Schramm, M. Tampo, V. Tikhonchuk, H. Pepin, P. Audebert, O. Willi, T.E. Cowan, M. Borghesi, J. Fuchs
submitted to Physical Review Letters (2009)

Lateral hot electron transport and ion acceleration in femtosecond laser pulse interaction with thin foils
J. Psikal, V. T. Tikhonchuk, J. Limpouch, O. Klimo
submitted to Physics of Plasmas (2009)

Awards

winner of the **PPCF Poster Prize at the EPS Plasma Conference 2008**
for students in section Beam Plasmas and Inertial Fusion
with poster presentation *Ion acceleration by relativistically intense laser pulses with a large incidence angle*

Oral and Poster Presentations

Oral presentations

Enhanced laser-driven proton acceleration in mass-limited targets
7th Direct Drive and Fast Ignition Workshop, Prague, Czech Republic, May 2009

Ion acceleration in laser irradiated small-size targets
invited talk, Queen's University Belfast, UK, November 2008

2D PIC simulations of ion acceleration in laser irradiated small multispecies targets
9th Zababakhin Scientific Talks, Snezhinsk, Russia, September 2007

Poster presentations at international conferences

Lateral hot electron transport and ion acceleration in femtosecond laser pulse interaction with thin foils
6th International Conference on Inertial Fusion Sciences and Applications, San Francisco, USA, September 2009

Enhanced laser proton acceleration in mass-limited targets
36th EPS Conference on Plasma Physics, Sofia, Bulgaria, June 2009

The effect of large incidence angles on ion acceleration in thin foils by femtosecond laser pulses
30th European Conference on Laser Interaction with Matter, Darmstadt, Germany, September 2008

Ion acceleration by relativistically intense laser pulses incident on target at large angles
35th EPS Conference on Plasma Physics, Hersonissos, Greece, June 2008

Two-dimensional simulations of ion acceleration by ultraintense femtosecond laser pulses
34th EPS Conference on Plasma Physics, Warszaw, Poland, July 2007

Simulations of the ion acceleration in limited mass targets
2nd Forum ILP, Arcachon, France, March 2007

Résumé

Cette thèse a pour but l'étude de l'interaction des impulsions laser brèves et ultra-intenses avec des cibles de petite taille. Nous nous intéressons surtout des phénomènes liés à l'accélération des ions aux granges énergies. L'outil principal de cette étude est notre code Particle-in-Cell (PIC) bidimensionnel, qui est capable d'effectuer le calcul du mouvement des particules et de l'évolution des champs en régime relativiste et sans collisions. Cette mémoire présente la théorie de l'accélération d'ions par laser, les simulations numériques des différents régimes d'accélération, ainsi que les algorithmes mis en oeuvre dans notre code.

Les nouveaux résultats obtenus dans le cadre de cette thèse concernent trois cas principaux:
1) l'interaction des impulsions laser intenses avec des cibles de la masse limitée;
2) l'accélération des protons par laser dans des gouttelettes fines d'eau vaporisé;
3) le transport latéral des électrons chauds dans une feuille mince et son effet sur l'accélération d'ions.

Nos études théoriques et les simulations numériques sont appliquées pour l'interprétation des résultats des deux expériences récentes réalisées par les équipes de recherche en Allemagne et en France. Ces expériences montrent une accélération efficace d'ions dans les conditions prévues dans nos travaux théoriques. Le spectre énergétique et le nombre des protons accélérés dans les feuilles minces de la surface limitée et dans les gouttelettes d'eau se comportent conformément aux nos prévisions. Le modèle théorique développé dans cette thèse considère l'accélération des ions en deux étapes. Le champ du laser n'interagit pas directement avec les ions du plasma du à sa masse très élevée. Par contre, les électrons chauds, générés pendant l'interaction de l'impulsion laser avec une cible, produisent les champs électrostatiques importants qui accélèrent les ions aux hautes énergies. Ces champs peuvent être amplifiés si la masse de la cible est suffisamment petite.

Nous considérons que la cible a une masse limitée, si toutes ses dimensions sont comparables avec la taille du faisceau laser dans la zone d'interaction. Ces cibles permettent de réduire la dispersion des électrons chauds, et donc d'améliorer la transformation de l'énergie cinétique d'électrons dans l'énergie des ions. Nos simulations numériques indiquent que la taille de cible transverse optimale est égale au diamètre du faisceau laser. Les expériences récentes avec des feuilles minces de la surface limitée ont confirmé que la transformation de l'énergie laser à l'énergie des ions est plus efficace, l'énergie des ions est plus élevée, et la divergence du faisceau d'ions diminue avec la diminution de la surface de feuille.

La physique de l'interaction d'un faisceau laser avec les gouttelettes d'eau est plus complexe, car il faut prendre en compte plusieurs facteurs tels que l'ionisation inhomogène des atomes de la gouttelette et la recombinaison, sa position dans le focus de laser, les collisions des électrons etc. Nous avons modélisé l'interaction de l'impulsion laser avec une gouttelette de diamètre de $100\ \mathrm{nm}$. Dans un petit agrégat des atomes irradié par laser, les électrons sont expulsés par la force pondéromotrice et, pas conséquent, les ions sont accélérés par la force de Coulomb. Nous avons réussi d'expliquer la formation d'un pic dans la fonction de distribution des protons en énergie par l'effet de la répulsion mutuelle entre deux espèces des ions.

Finalement, nous avons étudié le transport latéral des électrons dans le cas de l'incidence rasante du faisceau laser sur la cible mince plaine. Avec une série des simulations nous

avons démontré qui le transport des électrons accélérés est réalisé par deux mécanismes complémentaires: par le guidage des électrons chauds sur la surface d'avant de la feuille par les champs quasi statiques électrique et magnétique et par la recirculation des électrons entre les faces l'arrière et l'avant de la cible. Le premier mécanisme concerne un petit nombre des électrons ayant la vitesse presque parallèle de la surface de la cible. Cependant, ces électrons sont accélérés à l'énergie plus élevée et ils, donc, peuvent augmenter l'énergie des ions accélérés au bout de la feuille. Par contre, la grande majorité des électrons est transportée par l'effet de recirculation. Cet effet de guidage peut être bénéfique pour l'accélération des électrons dans le cône pour la fusion nucléaire en allumage rapide.

Souhrn

Předkládaná dizertační práce se věnuje studiu interakce femtosekundových laserových pulsů s rozměrově malými terči a souvisejícími jevy, především urychlováním iontů. Ke studiu interakce a následného urychlování iontů je použit náš relativistický bezesrážkový dvoudimenzionální particle-in-cell kód. V práci je shrnuta teorie urychlování iontů stejně tak jako algoritmy použité v našem simulačním kódu.

Nově získané výsledky v rámci této práce jsou rozděleny do třech základních částí:
1) interakce laserového pulsu s tzv. terči o omezené hmotě; 2) urychlování protonů ve vodním spreji; 3) transport electronů do stran podél povrchu tenké fólie a vliv na urychlování iontů.

Tato teoretická studia na základě numerických simulací jsou doplněna nedávno získanými experimentálními výsledky od výzkumných týmů, se kterými jsme navázali spolupráci. Tyto experimenty demonstrující efektivnější urychlování iontů z tenkých fólií o velmi malém povrchu a energetická spektra protonů urychlených ve vodním spreji jsou v souladu s našimi teoretickými závěry a numerickými simulacemi.

Vzhledem k tomu, že maximální v současnosti dosažitelná intenzita laserového záření není dostatečná k přímému urychlení iontů na vysoké energie, jejich urychlování je zprostředkováno horkými elektrony vznikajícími při interakci laserového pulsu s terči, které vytvářejí silná elektrostatická pole, nebo Coulombovskou explozí iontů při porušení kvazineutrality v důsledku vypuzení elektronů z terče polem laserové vlny v případě malých clusterů.

Terče o omezené hmotě, které jsou definovány jako terče se všemi svými rozměry srovnatelnými s šířkou laserového svazku v ohnisku, omezují rozptyl horkých elektronů a tudíž je jejich kinetická energie účinněji trasformována do energie iontů. Numerické simulace ukazují, že optimální rozměr průřezu terče je roven šířce laserového svazku. Nedávné experimenty s tenkými fóliemi o omezeném povrchu potvrdili vyšší účinnost konverze energie laserového pulsu do iontů, jejich vyšší maximální energii a menší divergenci urychleného svazku iontů se zmenšujícím se povrchem fólie.

Přesný fyzikální popis interakce laserového pulsu s vodním sprejem je velmi komplikovaný, protože zahrnuje mnoho různých faktorů (ablace kapiček vody, nehomogenní ionizace kapiček, pozice ohniska laserového svazku ve spreji, rekombinace a srážky). Pro lepší pochopení alespoň některých fyzikálních procesů jsme simulovali interakci laserového pulsu s kapičkou vody o průměru $100\ \mathrm{nm}$. V souladu s experimentem jsme v simulaci pozorovali relativně mnoho urychlených protonů s maximální energií v energetickém spektru oproti protonům s nižší energií. Tato diskontinuita v distribuční funkci energií protonů je vysvětlována vzájemnou interakcí dvou různých druhů iontů.

Nakonec jsme studovali transport elektronů ke stranám tenké fólie, který je možný dvěma mechanismy - prvním je vodění horkých elektronů podél povrchu fólie v důsledku vznikajícího kvazistatického elektrického a magnetického pole; druhý je způsoben recirkulací elektronů, kdy se mění složka rychlosti elektronů kolmá k povrchu terče (osciluje) zatímco složka ve směru podél povrchu zůstává téměř konstantní. Ze simulací jsme zjistili, že většina elektronů je ke stranám transportována díky recirkulaci v tenké fólii. Pouze velmi malá část elektronů je vedena podél povrchu terče kvazistatickými poli a to jen při velmi šikmém úhlu dopadu laserového pulsu na terč (60° a více), avšak tyto elektrony mohou být dále urychleny na velmi vysoké energie a zvyšovat tak maximální energie iontů urychlených z okraje fólie.